A MEASUREMENT OF $\mathcal{R}_\mu = \sigma(W \rightarrow \mu\nu)/\sigma(Z^0 \rightarrow \mu^+\mu^-)$ IN $P\bar{P}$ COLLISIONS AT $\sqrt{S} = 1.8$ TEV

BY

RAYMOND LEE SWARTZ JR.

B.S., Michigan Technological University, 1986
B.S., Michigan Technological University, 1986
M.S., University of Illinois at Urbana-Champaign, 1987

THESIS

Submitted in partial fulfillment of the requirements
for the degree of Doctor of Philosophy in Physics
in the Graduate College of the
University of Illinois at Urbana-Champaign, 1994

Urbana, Illinois

A Measurement of $\mathcal{R}_\mu = \sigma(W \rightarrow \mu\nu)/\sigma(Z^0 \rightarrow \mu^+\mu^-)$ in $p\bar{p}$ collisions at $\sqrt{s} = 1.8$ TeV
Raymond L. Swartz Jr., Ph.D.
Department of Physics
University of Illinois at Urbana-Champaign, 1994
Professor Steven Errede, advisor

A measurement in the muon channel of the ratio of W and Z production cross sections times branching ratios yields $\mathcal{R}_\mu = \sigma(W \rightarrow \mu\nu)/\sigma(Z^0 \rightarrow \mu^+\mu^-) = 9.8 \pm 1.1(stat) \pm 0.4(syst)$, where the statistics of the Z sample is the dominant uncertainty. The individual cross sections times branching ratios are $\sigma(p\bar{p} \rightarrow W \rightarrow \mu\nu) = 2.21 \pm 0.07(stat) \pm 0.14(syst) \pm 0.15(lum)$ nb and $\sigma(p\bar{p} \rightarrow Z^0 \rightarrow \mu^+\mu^-) = 0.226 \pm 0.022(stat) \pm 0.018(syst) \pm 0.015(lum)$ nb. Combining with previous CDF results in the electron channel yields the overall results $\mathcal{R}_l = 10.0 \pm 0.6(stat) \pm 0.4(syst)$, $\sigma(W \rightarrow l\nu) = 2.21 \pm 0.04(stat) \pm 0.13(syst) \pm 0.15(lum)$ nb, and $\sigma(Z^0 \rightarrow ll) = 214 \pm 11(stat) \pm 14(syst) \pm 15(lum)$ pb. Using Standard Model assumptions we deduce the W inverse branching ratio and width, and a lower bound on the top quark mass of 45 GeV/c^2 (95% CL) which is independent of the decay mode. Lepton universality is confirmed in this energy domain. All results are in agreement with standard model predictions.

To my parents, from whom I learned to try. And to Patricia, from whom I learned success.

Acknowledgments

I want to start by thanking my parents and family, who recognized my interest in learning at an early age, and who afforded me the opportunity to learn all I could. I hope they realize how very important their support has been to me.

I would also like to thank my advisor, Steve Errede, who kept reminding me of the range and bredth of the field and prevented the development of a severe case of "physica myopia". Monte Carlo isn't the world, no matter how often you run the program.

To Dave Smith and Sarah Eno, who helped guide this analysis and, every now and then, would gently remind me that I've taken a wrong path. Although I sometimes questioned the need for even more cross-checks, when the time came to bring it all together I saw that these checks were necessary. I value their input.

Dave and Chris have been valuable (if somewhat unusual) friends. Through them I was exposed to many activities (and several activisms) I would not have otherwise experienced, including a mild appreciation for beer. This last one surprises me most of all.

I also have happy memories of other friends and students I had the pleasure of knowing. Russ and Jill Shermer will always be remembered for great cooking, aquaria, pinochle, and The Great Physics House Tracer Wars. When it comes to tracer guns, it pays to buy American. Dave and Karen have been great friends, although I am not around to see them as often as I'd like.

I would also like to thank all the folks at the Illini Glider Club, who taught me to fly. Kevin has impressed me often with his ability in the 1-26. I may yet do that silver distance flight.

And finally, to Patricia, who made the time pass much too quickly.

This research was supported in part by the U.S. Department of Energy under contracts DE-AC02-76ER-01195 and DOE-FG02-91ER-40677, and the A.P. Sloan Foundation.

TABLE OF CONTENTS

LIST OF TABLES

LIST OF FIGURES

Chapter 1

Introduction

A major part of the success of physics in the 20^{th} century is due to the study of the fundamental units of matter and the forces that govern their interactions. These forces are the strong force, the weak force, the electromagnetic force, and the gravitational force. We study these forces to learn about nature and the structure of the universe we inhabit. This quest has not gone without reward as the last two decades have seen the leading theory governing the first three forces listed above, known as the Standard Model, become one of the most thoroughly tested and most successful theories of modern physics.

After the discovery of radioactivity, Rutherford became the first to use energetic particles to probe nature on an intimate level when he beamed α particles into a thin gold foil to discover the atomic nucleus [1]. With the technological developments to follow we were able to build particle accelerators to artificially boost particles to ever higher energies, allowing even deeper probes of the structure of matter.

A significant part of the Standard Model was developed by Weinberg, Salam, and Glashow when they postulated the unification of the weak and the electromagnetic forces [2, 3, 4], using vector bosons first postulated by Fermi [5]. The first of these bosons to be discovered was the $W^{\pm}$ in 1983 [6, 7], followed by the Z^0 [8, 9]. Their study provides insights into the Standard Model. Currently, the W boson can only be produced at hadron colliders, due to the nature of the coupling of the W boson to fermions. The highest energy hadron collider in the world is the Tevatron at Fermilab. By measuring the production cross section times decay branching ratio of the W boson to leptons, and finding the ratio of it to that of the Z, we test some fundamental aspects of the theory.

Chapter 2

Theory

2.1 The Standard Model

The Standard Model is an enormously successful theory of fundamental particle interactions, incorporating Quantum Chromodynamics (QCD) and Electroweak Theory (which includes Quantum Electrodynamics (QED)). The theory describes the interactions between two types of fundamental particles; fermions and bosons.

The fermions consist of 3 generations each of quarks and leptons, all of which have spin $\frac{1}{2}\hbar$. As seen in Table 2.1, there are 6 of each. The quarks are called Up, Down, Strange, Charm, Top and Bottom. The Top has not yet been experimentally verified, but there is compelling indirect evidence of its existence. The quarks have fractional charge, are massive, and have an additional degree of freedom called color. Color is the "charge" of QCD interactions. There are three charges of color: red, green, and blue. The nature of the color charge prevents quarks from being observed unless they combine into a color singlet state, so they are never seen outside of a composite particle. The leptons have no strong color charge and interact via the Electroweak

Fundamental Particles				
Fermions				Bosons
Q	Quarks	Q	Leptons	$W^{\pm}$,Z^0,γ,
+2/3	u c t	-1	e μ τ	8 gluons (g),
-1/3	d s b	0	ν_e ν_μ ν_τ	Higgs (H)

Table 2.1: The fundamental particles of The Standard Model divided into several groups. The interactions between the fermions are mediated by the bosons.

force only. The Electroweak force behaves as the gauge group $SU(2)_L \otimes U(1)_Y$. There are two types of leptons. They either have charge and mass (e,μ,τ), or they are uncharged and, to the best of our knowledge, are massless (ν_e,ν_μ,ν_τ).

Bosons have integer spin and are the carriers of forces. There are 12 in the Standard Model: γ, $W^{\pm}$, Z^0, and 8 gluons. The photon (γ) and weak bosons ($W^{\pm}$, Z^0) are the carriers of the electroweak force. The $W^{\pm}$ bosons are described totally by the $SU(2)_L$ sector of the Electroweak theory, while the photon (γ) and the Z^0 contain elements of both the $SU(2)_L$ and $U(1)_Y$ sectors. An octet of gluons carry the color charge of the strong force, and they themselves have color so they interact. Thus the QCD theory of $SU(3)_c$ used to describe them is non-abelian. The Higgs particle is necessary for the Standard Model as it is currently understood because it is responsible for giving the bosons their masses, but it has not yet been observed. This thesis deals specifically with the production and decay properties of the W and Z bosons of the electroweak interaction.

2.2 Boson Production in $p\bar{p}$ Collisions

The Drell-Yan subprocess which produces weak bosons in $p\bar{p}$ collisions, $q\bar{q} \to W(Z)$, is directly calculable within the Standard Model. The calculation is complicated by the fact that the quarks do not exist alone; they are confined, along with gluons and virtual $q\bar{q}$ pairs, to the interior of protons and antiprotons. Calculating the boson production cross section requires knowledge of the momentum sharing among the quarks and gluons (partons) comprising the proton so that one can integrate over the range of expected momentum fractions for the partons. The quarks and gluons that do not participate in the event are called *spectators* and will also fragment, contributing a low energy background of charged and neutral particles to the event. This background is called the underlying event.

Using the W as an example, the calculation of a production cross section takes the form

$$\sigma_{tot}(p\bar{p} \to W) = \sum_{ij} \int dx_i dx_j f_a(x_j, Q^2) \bar{f}_{\bar{b}}(x_i, Q^2) \hat{\sigma}(q_i^a \bar{q}_j^{\bar{b}} \to W)$$

where the sum runs over all partons. The quantity $f_a(x_k, Q^2)\bar{f}_a(x_k, Q^2)$ is the probability for having a parton of species k with momentum fraction $x_k = p_k/p_{proton}$ in the (anti)proton a with momentum Q (where $Q^2 = M_W^2$). This probability depends on the parton type. The term $\hat{\sigma}(q_i^a \bar{q}_j^{\bar{b}} \to W)$ is the cross section for parton i from proton a with momentum fraction x_i and parton j from antiproton $\bar{b}$ with momentum fraction x_j to create W.

These functions are found by fitting data from lepton-proton inelastic scattering experiments, and evolving the data to the Q^2 scale of boson production from the lower energies where the data were taken. An example of a proton structure function is shown in Figure 2.1, which displays the HMRSB function [10] at $Q^2 = M_Z^2$. The individual partons are identified in the plot.

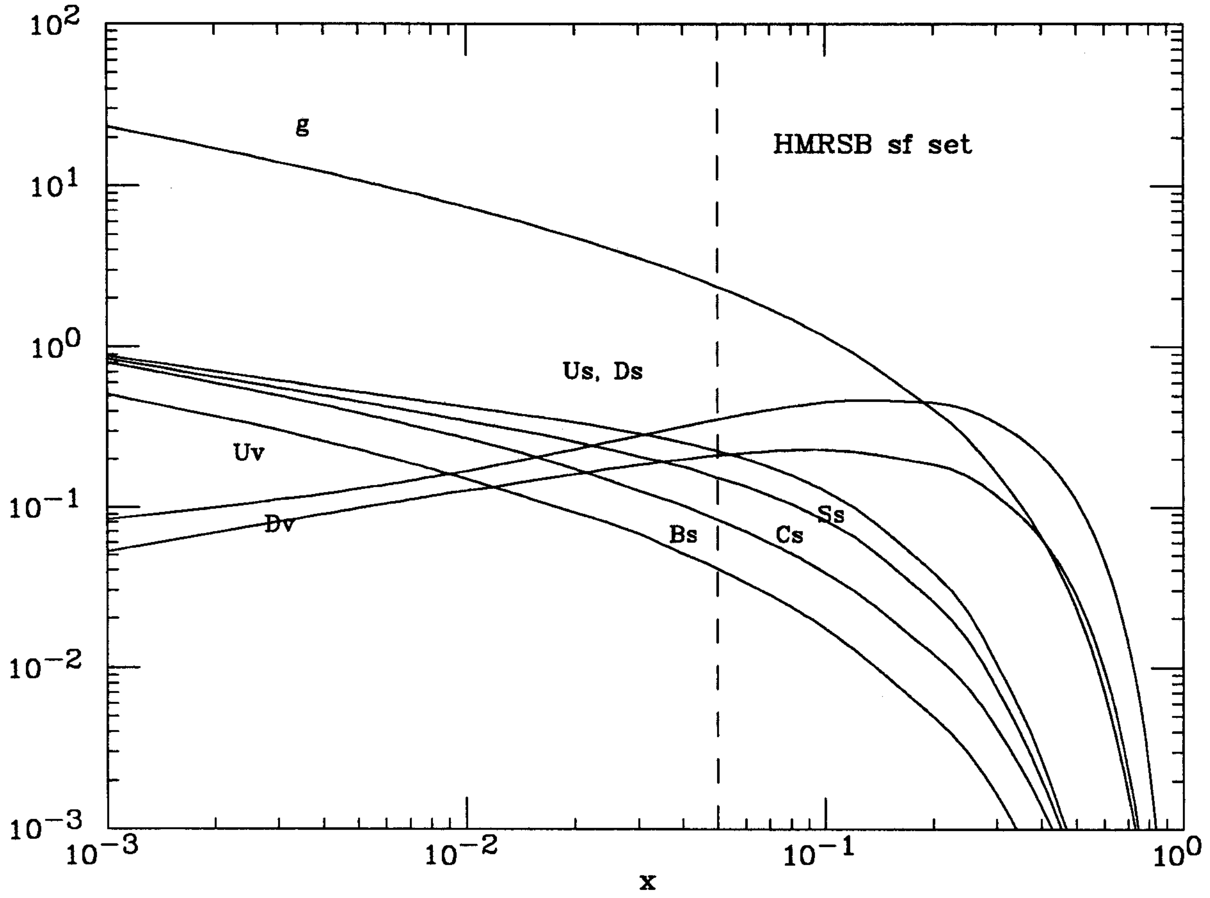

Figure 2.1: The HMRSB proton structure function at the Z mass. The subscripts denote either 'valence' or 'sea' quarks for the types named. The 'g' curve represents the gluons. Z's generated on the mass shell from partons of equal momenta are located at the dashed line, so that the relative contributions of parton types is determined.

Parton	Vector Coupling (g_V)	Axial Coupling (g_A)
ν	$+1/4$	$-1/4$
e, μ, τ	$-1/4 + \sin^2\theta_W$	$+1/4$
u	$+1/4 - \frac{2}{3}\sin^2\theta_W$	$-1/4$
d	$-1/4 + \frac{1}{3}\sin^2\theta_W$	$+1/4$

Table 2.2: The vector and axial coupling constants needed to calculate the partial widths.

2.3 Boson Decay

The W and Z bosons decay into fermions, either leptons or quarks. The fundamental partial widths of the decays are:

$$\Gamma(W \to \mu\nu) = \frac{G_F}{\sqrt{2}}\frac{M_W^3}{6\pi}$$

and

$$\Gamma(Z^0 \to ll) = 8(g_V^2 + g_A^2) \cdot \Gamma(Z^0 \to \nu\nu)$$

where

$$\Gamma(Z^0 \to \nu\nu) = \frac{G_F}{\sqrt{2}}\frac{M_Z^3}{12\pi}$$

and the vector and axial couplings, g_v and g_A are defined in Table 2.2. The theoretical decay widths to massless fermions are $\Gamma(W \to \mu\nu) = 226 \pm 2$ MeV, $\Gamma(Z^0 \to \mu^+\mu^-) = 83.5 \pm 0.1$ MeV, $\Gamma_{tot}(W) = 2.08 \pm 0.02$ GeV and $\Gamma_{tot}(Z) = 2.478 \pm 0.002$ GeV [11].

The branching ratio of a decay is the ratio of the partial to the total decay width. With the widths presented above the branching ratios are $BR(W \to \mu\nu) = 10.87 \pm 0.14\%$ and $BR(Z^0 \to \mu^+\mu^-) = 3.370 \pm 0.005\%$. The measured branching ratios are $BR(W \to \mu\nu) = 10.5 \pm 1.9\%$ and $BR(Z^0 \to \mu^+\mu^-) = 3.34 \pm 0.04\%$ [12]. Although the largest branching fraction for both bosons occurs when they decay to hadron jets, these are difficult to separate from QCD background in $p\bar{p}$ collisions.

2.4 Motivation

Theoretically, the cross section for $W^{\pm}$ bosons produced in $p\bar{p}$ collisions and decaying via the muon channel are described by

$$\sigma \cdot B(W \to \mu\nu) = \sigma(p\bar{p} \to W) \cdot B(W \to \mu\nu) = \sigma(p\bar{p} \to WX)\frac{\Gamma(W \to \mu\nu)}{\Gamma_{tot}(W)} \tag{2.1}$$

and, similarly, for the Z^0, the cross section is

$$\sigma \cdot B(Z^0 \to \mu^+\mu^-) = \sigma(p\bar{p} \to Z) \cdot B(Z^0 \to \mu^+\mu^-) = \sigma(p\bar{p} \to ZX)\frac{\Gamma(Z^0 \to \mu^+\mu^-)}{\Gamma_{tot}(Z)} \tag{2.2}$$

where X represents the additional parts of the event caused by the spectator partons which are not involved in the boson production. The production and decay of the bosons is illustrated by the diagrams in Figure 2.2. The cross section ratio is

$$\mathcal{R}_\mu \equiv \frac{\sigma \cdot B(W \to \mu\nu)}{\sigma \cdot B(Z^0 \to \mu^+\mu^-)} = \frac{\sigma(p\bar{p} \to WX)}{\sigma(p\bar{p} \to ZX)} \cdot \frac{\Gamma(W \to \mu\nu)}{\Gamma(Z^0 \to \mu^+\mu^-)} \cdot \frac{\Gamma_{tot}(Z)}{\Gamma_{tot}(W)}. \tag{2.3}$$

To measure these parameters experimentally, however, we must represent them in quantities which are directly observed, such as the number of candidate events within a window of kinematic and geometric requirements. We describe this explicitly for the W case; the method is identical for the Z. First, we require an expression for the number of W candidate events

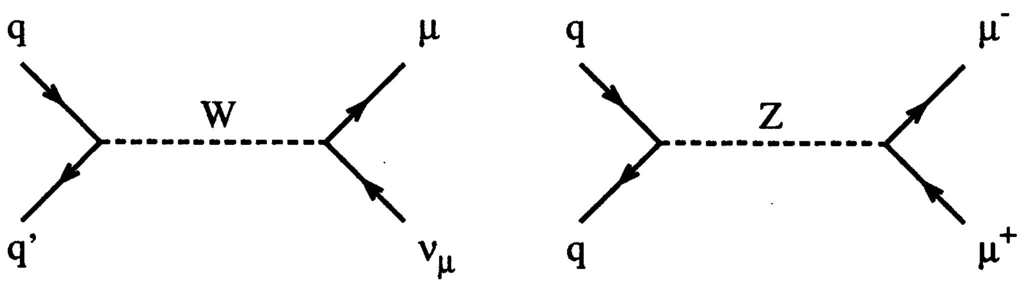

Figure 2.2: The Feynman diagrams describing the $q\bar{q}$ production and muonic decay of W and Z bosons to muons.

that will be observed (N_W^{obs}) when N_W^{gen} are generated by the $p\bar{p}$ collisions within the detector:

$$N_W^{obs} = N_W^{sig} + N_W^{bkg} = [A_W \cdot \epsilon_W \cdot N_W^{gen}] + N_W^{bkg} \tag{2.4}$$

where N_W^{sig} and N_W^{bkg} are the number of signal and background events which pass our W selection criteria, A_W is the geometric and kinematic acceptance of the muon and neutrino produced by the W decay, ϵ_W is our W event selection efficiency.

The number of muonic Ws generated is simply

$$N_W^{gen} = \sigma \cdot B(W \to \mu\nu) \cdot \int \mathcal{L} dt \tag{2.5}$$

where the integrated luminosity, $\int \mathcal{L} dt$ is the time integral of the beam intensity, and is discussed in detail in section 4.4.4

Combining eqns. 2.4 & 2.5 and rearranging, we obtain

$$\sigma \cdot B(W \to \mu\nu) = \frac{N_W^{obs} - N_W^{bkg}}{A_W \cdot \epsilon_W \cdot \int \mathcal{L} dt} = \frac{N_W^{sig}}{A_W \cdot \epsilon_W \cdot \int \mathcal{L} dt}. \tag{2.6}$$

Taking equation 2.6, our experimental calculation of $\sigma \cdot B$, and a similar equation for the Z^0 boson, we find the ratio

$$\mathcal{R}_\mu = \frac{\sigma \cdot B(W \to \mu\nu)}{\sigma \cdot B(Z^0 \to \mu^+\mu^-)} = \frac{N_W^{obs} - N_W^{bkg}}{N_Z^{obs} - N_Z^{bkg}} \cdot \frac{A_Z \cdot \epsilon_Z}{A_W \cdot \epsilon_W} = \frac{N_W^{sig}}{N_Z^{sig}} \cdot \frac{A_Z \cdot \epsilon_Z}{A_W \cdot \epsilon_W} \qquad (2.7)$$

where a factor of $\int \mathcal{L} dt$ has cancelled. This is a strong motivation for this measurement, since this luminosity factor has one of the largest uncertainties in the measurement of the individual cross sections.

2.5 Outline of the Analysis

The method for this analysis is guided by equation 2.7. We begin by applying high-efficiency selection criteria to events from the CDF '88-'89 data-taking run to select good high-p_t isolated muons. These cuts will serve to reject as much background as possible while still accepting real muons. We then take this sample of muons and apply additional, less stringent cuts to search for either a second muon (for Z's) or a significant amount of Missing Transverse Energy [1] (indicating a neutrino from W decay). These additional cuts are intentionally kept loose to maintain a high boson efficiency while rejecting other types of events, producing separate W and Z data samples. This process is described in Chapter 4

By using Monte Carlo simulations we determine the fraction of $W(Z)$ events that traverse the active regions of the detector; a measurement called the geometric acceptance. These are the A_W and A_Z terms in eqn. 2.7 which we use to normalize the number of events that traverse the detector to the number actually produced. Chapter 5 describes this procedure.

---

[1] This term will be fully explained in section 4.2.3.

Chapter 6 details the determination of the boson selection efficiencies. Not all boson events will pass our selection criteria; some will be rejected. The efficiency values will allow the number of observed events to be normalized to the number of events which actually occur in the CDF detector, and is denoted by the ϵ term in equation 2.7.

Chapter 7 describes the measurement of the backgrounds still existing in the data samples. Just as some boson events will not pass the selection criteria, some background events will pass the criteria and remain in the sample. This measurement will determine the $N_{W(Z)}^{bkg}$ terms in eqn. 2.7.

The values are combined in Chapter 9 and used to measure several parameters of the Standard Model. Items to be calculated include the W branching ratio to muons, an upper limit on the number of lepton generations and a lower limit on the top quark mass. We also test lepton universality at the W mass scale.

Chapter 3

Experimental Apparatus

3.1 The Accelerator

The Fermi National Accelerator Laboratory was built in Batavia, Illinois to operate a synchrocyclotron accelerator housed inside a 1 km radius tunnel. This original accelerator had a maximum energy of 400 GeV per beam, and now serves as a injector for a superconducting collider called the Tevatron, named for its design energy of 1 TeV per beam. For this analysis, the Tevatron was operating at 900 GeV per beam. The design energy is expected to be reached in 1994.

The Tevatron is operated in either of two modes; as a fixed target proton accelerator or as a high energy collider using counter-rotating beams of protons and antiprotons. The data for this analysis was collected with the Tevatron operating in the $p\bar{p}$ mode; we shall therefore constrain our explanation to the operation of the Tevatron as a hadron collider.

The protons used in the collisions are accelerated in several steps. Negative hydrogen ions are electrostatically accelerated to an energy of 500 keV in a Cockcroft-Walton accelerator before being injected into a linear accelerator which accelerates them to 200 MeV. The electrons are removed and the remaining protons travel to a small ring booster, which accelerates them up to 8 GeV. The protons are then injected into the original Fermilab accelerator, now called the Main Ring, where they are further accelerated to 150 GeV.

At this point some of the protons are diverted and slowed to collide onto a tungsten-rhenium fixed target at $\sim$ 80 GeV, producing antiprotons. The antiprotons are collected, decelerated, and cooled in a storage ring and the process repeated until enough antiprotons are collected to be transferred back to the Main Ring. There they circulate opposite the protons already occupying it, and are accelerated to 150 GeV. The p's and $\bar{p}$'s are transferred to the Tevatron in six bunches where they are accelerated to 900 GeV and made to collide in six intersection regions, one of which houses the CDF detector. The layout of the site and the accelerators may be seen in Figure 3.1.

3.2 The Detector

The Collider Detector at Fermilab (CDF) is a large, 5000 tonne multi-purpose detector designed to study events generated at the Tevatron at a collision energy of 2 TeV [13]. It is composed of 14 subsystems designed to measure particle momentum, energy, and penetrating ability, thereby identifying the collision products and allowing study of the physics involved. There are three tracking detectors, six calorimeter subsystems, and two muon detection systems. The tracking systems are embedded in a 1.4116 Tesla axial magnetic field generated by a 5 m long and 3 m diameter superconducting solenoid. The measurement of the charged tracks in the magnetic field enables the unique determination of the charged particle's momentum. Outside of the solenoid are layers of hermetic calorimeters arranged in projective towers that point to

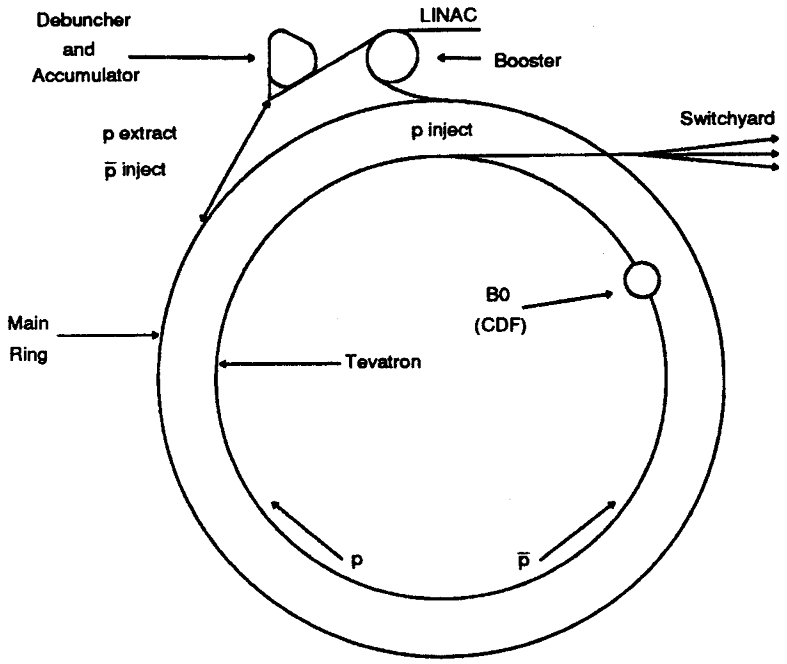

Figure 3.1: The layout of the Fermi National Accelerator Laboratory, located in Batavia, Illinois, showing the boosters, Main Ring, and the switchyard leading to the fixed target areas.

the nominal interaction region with uniform granularity in η and ϕ, and extend to within 2° of the beamline. All of these systems are interleaved to cover most of the 4π steradians of solid angle, in a layout shown in Figures 3.2 and 3.3.

The CDF coordinate system is defined with the z axis being the direction of the proton beam, the y axis is vertical, and the x axis points radially outward from the center of the Tevatron ring. Spherical coordinates are used, and refer to the $+z$ axis as $\theta = 0$ and the $+x$ axis as $\phi = 0$. Another useful parameter in frequent use in high-energy physics is the approximately Lorentz-invariant coordinate $\eta = -log(tan\frac{\theta}{2})$ which corresponds to the polar angle and is called the pseudorapidity.

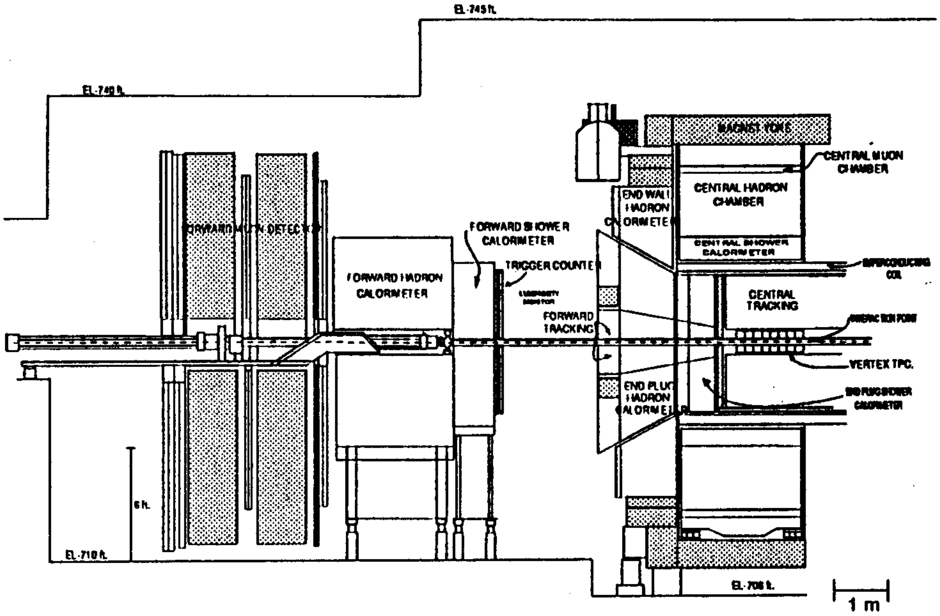

Figure 3.2: A cutaway view showing the main systems of the CDF detector, which is symmetric about the vertical plane through the interaction point.

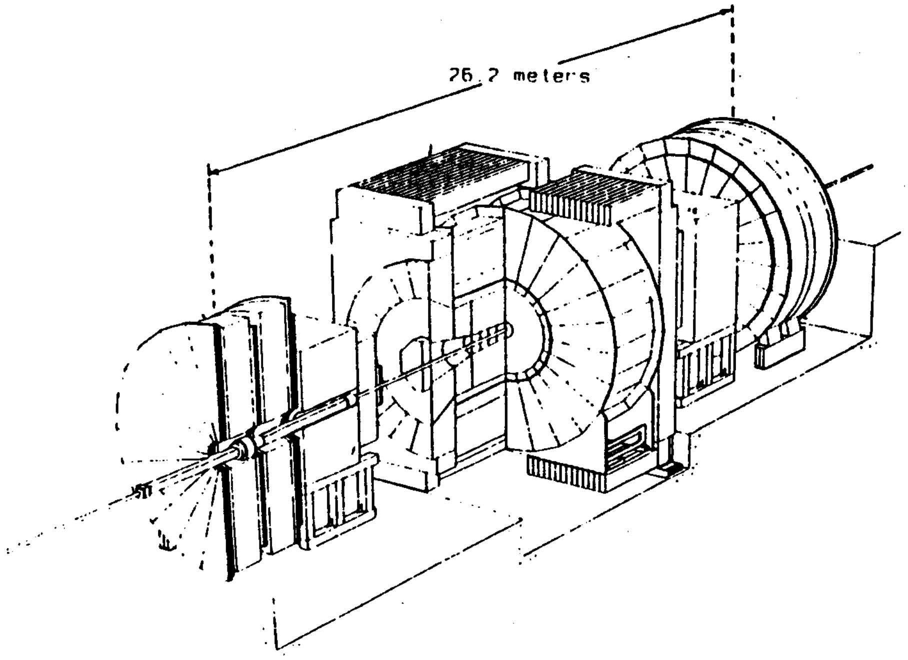

Figure 3.3: A perspective view of the CDF detector, showing the 15° segmentation of the central wedge.

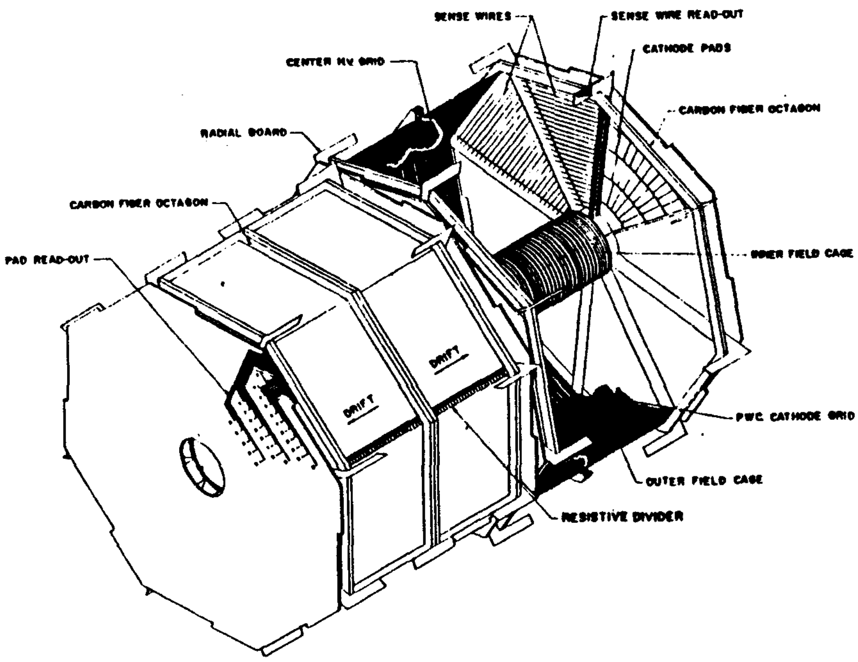

Figure 3.4: A cutaway view of the Vertex Time Projection Chambers (VTPC).

3.2.1 Tracking

The CDF detector contained three tracking systems when the data for this analysis was taken, two of which are used in this analysis. These are discussed in the order that a collision product would encounter them. Combining these systems yields the event vertex location and three dimensional reconstruction for tracks within the range $-1.0 \leq \eta \leq 1.0$.

The Vertex Time Projection Chambers (VTPC) consists of eight modules placed end-to-end for a total length of 2.8 m along the beamline [14], as shown in Figure 3.4. They are designed to measure charged tracks in the r-z plane to within 3.5° of the beamline. Alternating chambers are rotated 11.3° in ϕ so that stereo information is also provided. These tracks are used to identify and locate event vertices in order to tag the resultant collision products to the correct vertex. In the 1988 run, the majority of the events (approximately 80%) were single-interactions, for which the VTPC could measure the vertex location to within 1 mm. The

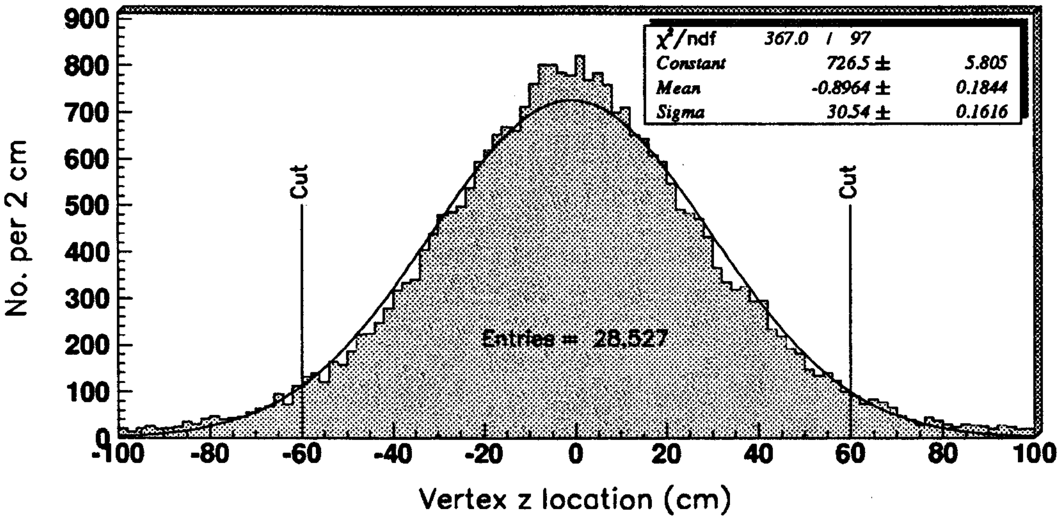

Figure 3.5: The distance (cm) of the event vertex from the origin of the CDF coordinate system. The CDF coordinate system is described in the text. The figure also indicates the event selection criteria we shall impost on the vertex position.

collisions are well-controlled by the Tevatron operators so that the $p\bar{p}$ interactions are made to occur near the origin of the CDF detector, as seen in Figure 3.5. The gaussian spread of the vertex location along the z axis is caused by the beam's ~ 1 m bunch length and the shape of the bunches.

The Central Tracking Chamber (CTC) is a cylindrical drift chamber which surrounds the VTPC and is used to measure tracks in the r-ϕ plane [15]. It consists of 84 layers of sense wires grouped into nine *superlayers*, of which five are axial superlayers containing 12 wire layers designed to measure the track curvature, yielding $\vec{p}_t$, and four are stereo superlayers containing 6 wire layers each which are canted 3° from the beamline to yield θ information. All of the superlayers have cells that are tilted 45° from the radial direction in order to compensate for the Lorentz angle of the electron drift in the magnetic field, allowing track ionization to drift azimuthally which simplifies the time-distance relationship. This tilting of the CTC cells is easily seen in Figure 3.6. The effective rms resolution of the the CTC is approximately

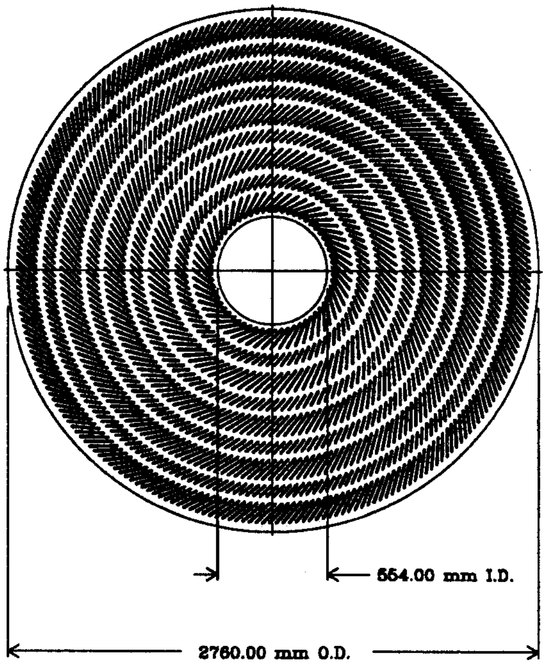

Figure 3.6: An end view of the CTC chamber, showing wire placement into 'superlayers' and the 45° cell-tilt to compensate for the Lorentz angle of the ionization drift.

$\frac{\delta p_t}{p_t} = 0.0011 p_t$ (p_t in GeV/c) for isolated tracks, with an effective coverage of $40^\circ \leq \theta \leq 140^\circ$. Tracks beyond this range in θ begin to suffer degraded resolution. Since the CTC extends from 0.3 m to 1.3 m from the beam axis, it provides most of the information used to reconstruct a charged particle track.

The Central Drift Tube (CDT) array is located between the outer edge of the CTC and the inner wall of the solenoid [16]. It is made up of 2016 drift tubes 12.7 mm in diameter and 3.0 m long, consisting of 3 layers of 672 tubes each. These tubes operate in limited-streamer mode using a 50%-50% argon-ethane mixture, and use drift times and charge division to provide high resolution R-ϕ-z track information. The CDT is not used in this analysis, but is included here for completeness.

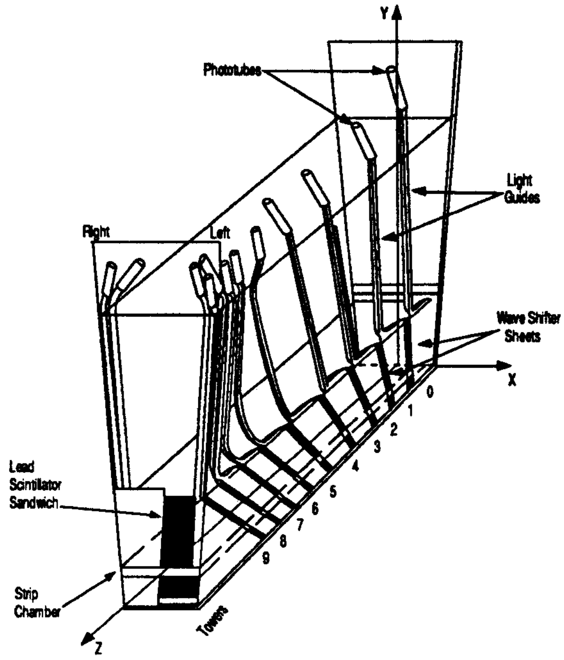

Figure 3.7: A view of a CEM wedge section of the CDF detector, showing the locations of the readout phototubes and strips, as well as the projective tower structure.

3.2.2 Calorimeters

The CDF calorimeter system was designed with a projective tower structure to combine fine granularity with good energy resolution. The towers are inclined to face the nominal interaction region and consist of multiple layers of absorbing material interleaved with a readout mechanism.

The central calorimeters cover the region $|\eta| \leq 1.1$ with a granularity of $\Delta\phi = 15°$ by $\Delta\eta = 0.1$, and consist of two systems, a Central Electromagnetic (CEM) [17] system and a Central Hadronic (CHA) [18] system, which encompass the superconducting solenoid. Each "slice" of 15° in ϕ is called a wedge and consists of, moving outward from the inner surface, the CEM, the CHA and the Central Muon Chambers at the outer edge.

The CEM uses 31 layers of polystyrene scintillator interleaved with 30 layers of lead, with a wave shifting material to redirect the light into acrylic lightguides which carry the signal to photomultiplier tubes. These scintillators offer good energy resolution and the calibration can be maintained to approximately 0.5% during the course of the data taking run by using cesium sources and a xenon flasher. A CEM wedge is shown in Figure 3.7

The CHA is similar to the CEM in construction and geometry except that the CHA uses iron instead of lead as the absorbing material and does not use wave-shifters in the light output path. The CHA was originally calibrated in a test stand using beams of known-energy pions.

Although this analysis does not explicitly use the Plug and Forward calorimeters, they are used in transverse energy calculations in the event reconstruction, so we include a brief description. Outside of the central region ($|\eta| \geq 1.1$) the calorimeter sampling system is based on proportional wire chambers immersed in a 50%-50% argon-ethane gas mixture. This sampling system allows for greater economy while showing a greater radiation resistance and a more adaptable geometry than the scintillator-based central calorimeters. The disadvantages are that the gains vary with the gas pressure and temperature so these calorimeters must be frequently calibrated using an Fe-55 source. They are also vulnerable to electronic noise. This region is divided into two pseudorapidity regions, with the plug systems (PEM & PHA) inside the region $1.1 \leq |\eta| \leq 2.4$ [19, 18] and the forward calorimeters (FEM & FHA) extending beyond the plug to $|\eta| \leq 4.2$ [20, 21]. Each of these regions contain a finer granularity than the central calorimeters, with each tower covering $\Delta\phi = 5°$ and $\Delta\eta = 0.1$.

3.2.3 Beam-Beam Counters

The Beam-Beam Counters (BBC) consist of two planes of scintillation counters which subtend the region $3.3 \leq |\eta| \leq 5.9$ [13]. These counters have good timing resolution (< 200 ps) which are used in coincidence to detect inelastic $p\bar{p}$ interactions. The BBC rate may also be used to directly measure the luminosity of the colliding beams via

$$\mathcal{L} = \frac{R_{BBC}}{\sigma_{BBC}}, \tag{3.1}$$

where R_{BBC} is the BBC rate and σ_{BBC} is the effective $p\bar{p}$ cross section of the counters, including the geometrical acceptance. The effective cross section of the BBC is calculated using the UA4 [22] published values for non-diffractive and diffractive inelastic cross sections at $\sqrt{s} = 540$ GeV which are scaled up to $\sqrt{s} = 1.8$ TeV [23] by using the CDF minimum bias Monte Carlo [24]. The uncertainty in σ_{BBC} is 6.8%, which dominates the uncertainty of the measured integrated luminosity at the CDF interaction region.

3.2.4 Muon Detection

The Central Muon Chambers (CMU) are the outermost part of the central detector apparatus, behind approximately 5 absorption lengths of central calorimeter at a distance of 3470 mm from the interaction region [25]. These drift chambers consist of a four-by-four array of drift cells, seen in Figure 3.8, operated in the limited-streamer mode using a 50%-50% mix of argon-ethane with an additional 0.7% alcohol. There is a nominal 5500 volt potential that is held between the edges of the drift cells and the sense wire, which gives a relatively constant drift velocity of 45 μm/ns in the cell.

In order to reduce the number of electronic channels which need to be read out, the sense wires of alternate layers are "ganged" at $\theta = 90°$. The wires are read out only on the outer sides of the wedges. The CMU uses drift time and charge-division information to provide three dimensional reconstruction of the muon tracks traversing the chambers. Two of the four layers of cells are offset in order to resolve the left-right ambiguity found when attempting to use drift

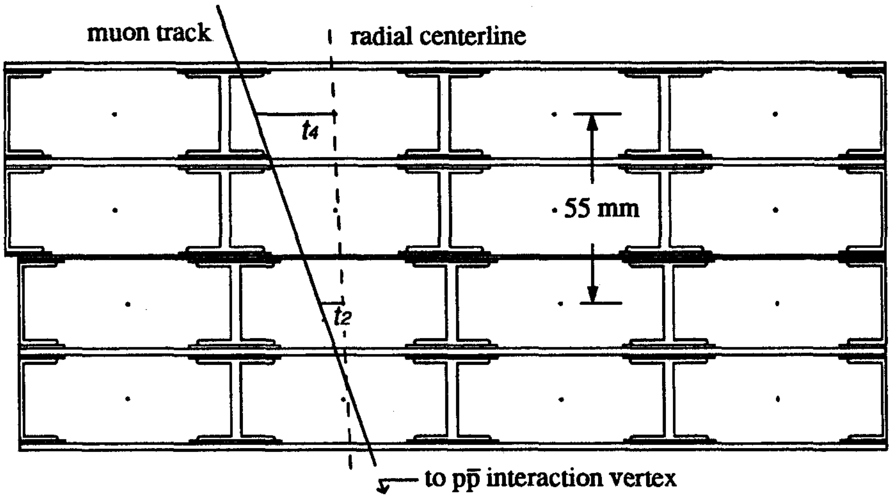

Figure 3.8: An end view of a CMU section showing the 4x4 array of cells that makes up a chamber, three of which are in a wedge. Also seen are a sample muon track and the sense wire locations.

time information. The resulting muon "stubs" are combined with CTC track information to gain a complete picture of the muon's path through the detector.

Three muon chambers are located side-by-side per calorimeter wedge and, discounting small cracks, cover 12.6° of the 15° spanned by the wedge. This leaves a 2.4° gap between adjacent wedges. This arrangement is seen in Figure 3.9. The CMU chambers cover only 226 cm of the 250 cm length of each calorimeter wedge so that within the $56^\circ < \theta < 124^\circ (|\eta| < 0.63)$ covered by the chambers there is a 3° crack at $\theta = 90^\circ$ which divides the positive and negative η wedges.

3.3 Event Triggering

With 6 bunches of protons and antiprotons in the Tevatron collider, as was the normal operating mode during the '88-'89 run, a bunch crossing occurs every 3.5 microseconds. Many of these crossings result in an inelastic $p\bar{p}$ interaction, such that these interactions occur at a rate of $\sim 10^5$ times higher than the rate at which the CDF data acquisition system can record them.

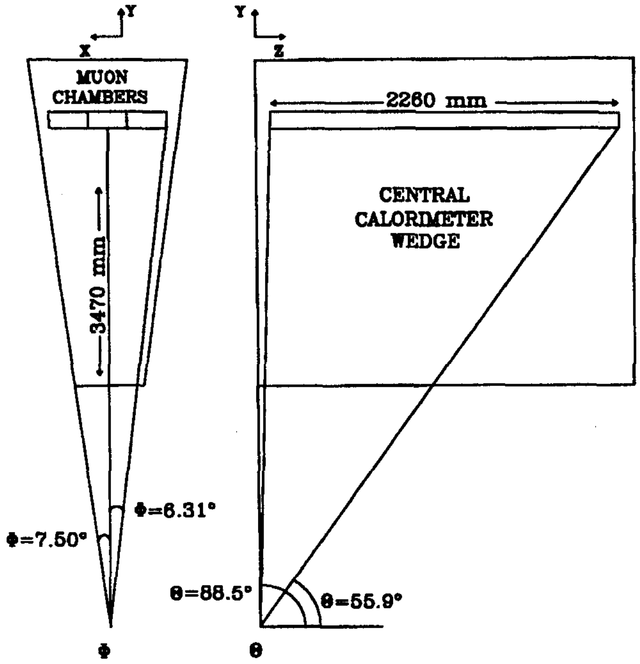

Figure 3.9: Two views of a sample wedge, showing the locations of the calorimeter systems and the muon chambers.

The production cross section of the events studied in this analysis are on the order of 2 nb, while the total inelastic cross section seen by the BBC at $\sqrt{s} = 1.8$ TeV is $\sim$ 50 mb. To reject the uninteresting events we employ a sophisticated four level trigger system [26]. This system was designed so the decision process at each level would reduce the data rate for the next level, where a more sophisticated trigger decision could take place with a minimum of deadtime. Levels 0, 1, and 2 consist of programmable hardware modules and use only a subset of the event data for the decision, while Level 3 is based on a "farm" of computers running filter algorithms and has the full detector data available.

3.3.1 Level 0

The Level 0 trigger is used to signal whether an inelastic collision has occurred in the interaction region by requiring a coincidence of hits in the east and west BBC systems. These hits are required to be within a 15 ns gate centered on the expected beam crossing, and the decision is made within the 3.5 μsec between beam crossings. Thus in the case where the Level 0 trigger rejects an event the system is ready for the next immediate crossing, causing no deadtime for the system. If the Level 0 trigger is satisfied by an east-west hit coincidence data-taking is inhibited during the next bunch crossing so that a Level 1 trigger decision can be made. At a nominal instantaneous luminosity of 10^{30} cm^{-2}sec^{-1} the Level 0 trigger rate is approximately 50 kHz.

3.3.2 Level 1 Muon Trigger

The Level 1 muon trigger uses prompt hit information from the muon TDCs to identify high p_t tracks in the muon chambers [27]. The angle of a track with respect to the radial (infinite momentum) direction from the $p\bar{p}$ vertex is correlated to the transverse momentum of the track, as seen in Figure 3.10 where α is the angle of interest. A cut of the order $p_t = \frac{154}{\Delta t}$ GeV/c (Δt in ns) is imposed on the time difference of hits in alternate layers of the four layer muon system, allowing this angle to determine the momentum threshold of the Level 1 muon trigger. Either of the two possible alternate pairs passing the cut allows the event to pass the Level 1 muon trigger. This trigger decision is performed separately for each muon tower, and any towers in the event which passed the requirement satisfies the trigger.

Although this sort of trigger requirement might be naively expected to show a prompt turn-on at the designed p_t, multiple coulomb scattering insures that in practice this is not the case. Instead, as portrayed in Figure 3.11 we see a soft turn-on of the trigger with increasing track p_t. Some of the data from the 1988-89 run was taken with a Level 1 p_t threshold of 5 GeV/c, but the threshold was decreased to 3 GeV/c for the last two-thirds of the run.

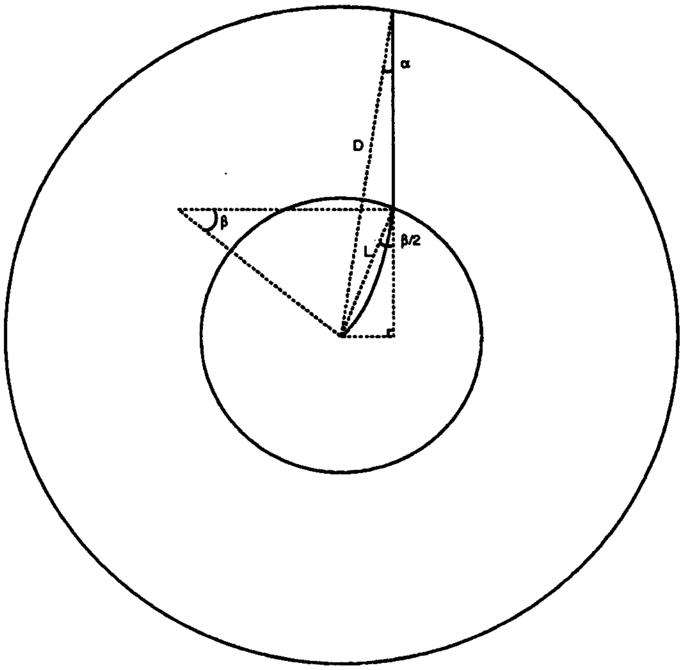

Figure 3.10: A diagram of a muon traversing the detector from the interaction region to the CMU. The inner circle represents the CDF solenoid, and the outer circle represents the layer of CMU chambers. Note that the angle α is correlated with the muon p_t.

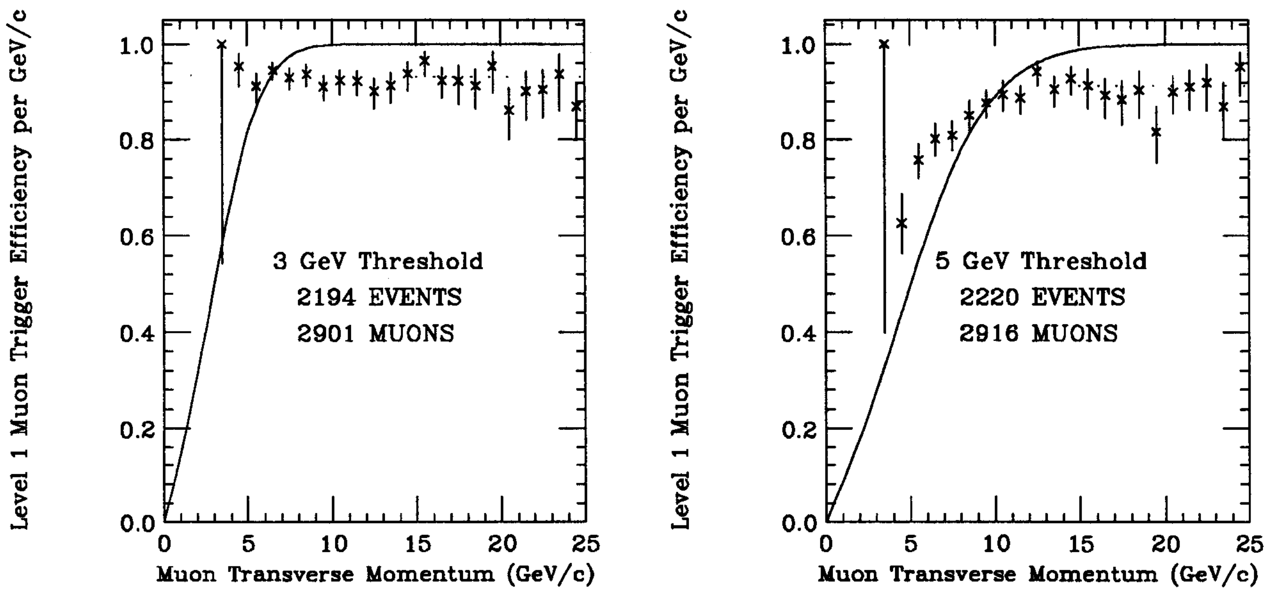

Figure 3.11: The efficiency of the Level 1 muon trigger with respect to track p_t, for a 3 and 5 GeV/c threshold. The data sample for these plots consists of cosmic rays. The curve is an analytic calculation of the effects of multiple scattering assuming 100% muon chamber efficiency.

In addition to the muon trigger there are also Level 1 decisions made about overall calorimeter deposition, energy balance, and the presence of high-p_t tracks. In order to understand the next level of the muon trigger the Level 1 high-p_t track trigger is of interest to this analysis. The Central Fast Tracker (CFT) is briefly discussed below. A Level 1 trigger decision is made in the 7 μsec allowed by Level 0. If the event fails all of the Level 1 decision requirements, the front end electronics are reset so that data taking can resume only two bunch crossings after the initial Level 1 decision.

3.3.3 Level 2 Muon Trigger

The Level 2 trigger system makes the final decision on whether the detector electronics are read out. This decision is critical to the efficiency of the detector, as the readout of the detector electronics typically takes 10-15 msec.

To understand the Level 2 muon trigger it is necessary to have a basic familiarity with the Central Fast Tracker (CFT). This is a hardware track processor which uses fast timing information from the 4392 axial sense wires of the CTC to find tracks [28]. The CFT matches CTC hits with a set of predetermined hit patterns for the range of p_t allowed by the CFT trigger threshold. The CFT processor has 8 p_t bins over the range 2.5 GeV/c to 15 GeV/c, with a momentum resolution of $\frac{\delta p_t}{{p_t}^2} = 3.5\%$. The CFT trigger threshold for the data in this analysis was 9 GeV/c, with an efficiency of 98% for tracks exceeding this p_t value. In an average processing time of 2.5 μsec per event, the CFT presents a list of identified two dimensional tracks to the rest of the CDF triggering system for use in Level 2 trigger decisions.

Once the Level 2 muon trigger receives the list of CFT tracks, a look-up table is consulted to determine which muon towers should be traversed by each track. An attempt is made to match

CFT tracks with CMU Level 1 trigger information to within 15°. A match between the two fires the Level 2 muon trigger. The Level 2 trigger decision typically required approximately 100 μsec per event.

3.3.4 Level 3 Muon Trigger

The CDF Level 3 trigger system consisted of a "farm" of sixty Motorola 68020 processor nodes which analyzed the data from different events in parallel, using streamlined versions of the CDF reconstruction code. The Level 3 decision takes an average of 20 seconds per processor per event.

The Level 3 muon trigger verifies the Level 2 result by using a fast two dimensional algorithm to reconstruct the tracks found by the CFT and determine the p_t and the ϕ of the track at the muon chambers. An attempt is made to match a track passing the CFT requirement of $p_t \geq 11$ GeV/c with the CMU hits identified by the Level 1 muon trigger. This match is done using a local variable x, where the x axis points in the ϕ direction and lies along the lowest layer of the CMU, and where $x = 0$ is defined at the radial line passing from the interaction region to the center of three muon chambers in a wedge. If the extrapolated track and the muon hits can be matched within $|\Delta x| = 10$ cm, then the Level 3 muon trigger is satisfied and the event is written to tape. If no track is found or a match is not made the event is rejected. The tape writing rate was limited to about 1 Hz.

Chapter 4

Data Selection

The cross section measurement is essentially one of counting events, so it is heavily dependent upon the criteria which are used to collect, reconstruct, and select the data sample. To avoid an inadvertent bias in the sample we must keep an accounting of the selection criteria imposed on the data. This section traces the collection, reconstruction and selection of the boson data sample for this analysis.

4.1 Data Collection

The events for this analysis were collected from June 1988 through May 1989. In this period, the Tevatron delivered an integrated luminosity of 9.1 pb^{-1}, of which 4.7 pb^{-1} was written to tape by the CDF data acquisition system. This corresponds to an average efficiency of 52%, with the accumulation of data during the run shown in Figure 4.1.

Data collection usually started after the proton and antiproton beams had been injected into the Tevatron and the beams had been focused and stabilized. This is called a collider *store*. The data would be collected for a typical period of 10 to 20 hours, until the Tevatron operators

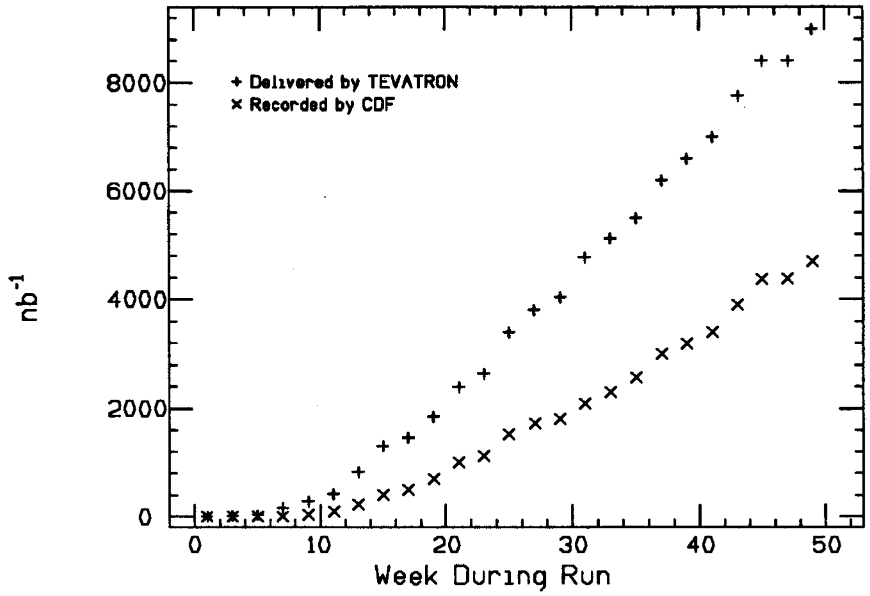

Figure 4.1: The integrated luminosity delivered by the accelerator and collected by CDF. The difference is caused by data collection inefficiencies in the experiment.

had prepared another *stack* of antiprotons for injection. Data collection was stopped when the beams were dumped. The time between stores was used in various calibration, monitoring and maintenance tasks. For example, the gas calorimeters were sensitive to changes in atmospheric pressure and had to have their energy scales calibrated regularly.

4.2 Event Reconstruction

The raw data from of the detector was recorded on magnetic tape during the run. In order to perform physics analysis the data must first undergo a process of reconstruction. The raw data for the detector systems was first translated into detector *elements*, with one detector element describing a particular hit in a detector in ADC and TDC counts. These elements were then grouped into *segments*, which is a clustering of related elements for each detector subsystem, resulting in identification of tracks and calorimeter clusters. The last stage of the reconstruction translated these segments into physics *objects*, later enabling our analysis to quickly scan an event for the objects we associate with a particular physics process. These objects correspond to real physical particles in the event such as electrons, muons or jets.

4.2.1 Track Reconstruction

The standard track reconstruction includes a mixture of two reconstruction philosophies. The first emphasizes precision by finding the sets of hits giving the best fits, and is good for analyses such as a mass measurement. The second philosophy tends to reject kinked tracks, as from decay-in-flight events, which is good for cross-section work as it eliminates much of the background. In the standard CDF event reconstruction both are used to obtain the highest efficiency.

The first method of track reconstruction involves sorting through the collected record of hits in the CTC for an event and searching along a path emanating from the vertex for elements (hits). These elements are fitted to a track as best as possible. The code then reviews the elements that were used in the fit and eliminates those with the worst residuals. The track is refit with the remaining elements, and the process is repeated until a stable local minimum is obtained in the χ^2 of the fit. When this minimum is obtained, the elements that were used to obtain this best fit are eliminated from the global list of CTC elements and the process is repeated until all possible tracks are reconstructed. This method obtains a minimum χ^2 for the track, but at the cost of sometimes "averaging" the two branches of a kinked track into a single calculated track by removing the "kink" (actually the point of particle decay) from the fit.

The second method entails sorting through the elements and fitting track *sections*. It takes four elements in an axial superlayer of the CTC to make a section, so these sections are sometimes very short. When a list of these sections has been compiled the code tries to match the sections into a track by calculating a curvature from two of the sections and extrapolating to determine where another section might be found. The list of remaining sections is then examined in an attempt to find one at the predicted location. Once a number of sections are found and fitted to the best possible track a quality requirement is imposed. If the track passes, those sections are removed from the list of available sections. This process is repeated until tracks are no longer found. This method tends to reject kinked tracks because it does not locate the "misplaced" extension of the track. This rejection reduces the background in the sample for across section measurement.

The standard CDF event reconstruction initially used the first method of tracking. The second method was applied to any remaining elements. Combining these methods was appropriate for a general-use data sample as the combination yielded both good precision and a high efficiency for finding tracks. The track resolution for this method is generally the resolution of the precision method, being $\frac{\delta p_t}{p_t} = 0.0011\, p_t = \frac{p_t}{909\ \mathrm{GeV/c}}$ (where p_t is the momentum in the transverse plane in GeV/c) for isolated tracks using a beam constraint. The momentum scale and resolution was determined using $J/\psi \to \mu\mu$ and $\Upsilon \to \mu\mu$ events in the process of measuring the Z mass [29, 30]. The measured masses of $M_{J/\psi} = 3.097 \pm 0.001$, $M_{\Upsilon\to\mu^+\mu^-} = 9.469 \pm 0.010$, and $M_Z = 90.9 \pm 0.3(stat + syst) \pm 0.2(scale)$ confirm the track momentum scale.

For this analysis the tracking code was rerun using the second method exclusively to reduce background. Since this analysis is simply one of counting events, high precision in the track parameters was not necessary if we accurately measured the selection efficiencies. We measured the CTC tracking resolution for our final data sample in order to accurately model the detector in a Monte Carlo simulation. By using Z events and adjusting the resolution of the model, a match was found for a track momentum resolution of $\frac{\delta p_t}{p_t} = 0.0020\ p_t = \frac{p_t}{500\ \mathrm{GeV}/c}$.

4.2.2 Calorimeter Energy Scale Determination

The calorimeter calibration originally came from 50 GeV electrons in the testbeam [31]. These calibrations were preserved during the run by comparing them to Cs^{137} source signals, which was good to 2.5%. Once the CTC momentum scale was determined, the CEM energy scale was determined using the measured electron momenta. This was further refined by using the electron E/p measurement for low p_t electrons. The last step was to extend the calibration to the high energy region using E/p from $W \rightarrow e\nu$ events [32, 33].

4.2.3 Neutrino ($\not{E}_t^{\nu}$) Reconstruction

Neutrinos do not interact with the detector, so for the decay $W \rightarrow \mu\nu$, indirect methods must be used to infer their existence and kinematic parameters. The Missing Transverse Energy, $\vec{\not{E}}_t$ is a measurement that has been developed to accomplish this. By summing up the visible transverse energies and using conservation of momentum, i.e. $\Sigma \vec{E}_t^{fin} = \Sigma \vec{E}_t^{ini} = 0$, the $\vec{\not{E}}_t$ is calculated via

$$\vec{\not{E}}_t = -\Sigma E_t^i \hat{n} \tag{4.1}$$

where $\hat{n}$ is a unit vector in the direction in the calorimeter tower being considered. This sum is calculated using all calorimeter towers with $|\eta| < 3.6$ containing $E_t > 100$ MeV. Were we dealing with $W \rightarrow e\nu$ events where the electron deposits all of its energy in the calorimeter, this would be sufficient to identify and measure neutrinos as $p_t^{\nu} = \not{E}_t$. However, since this

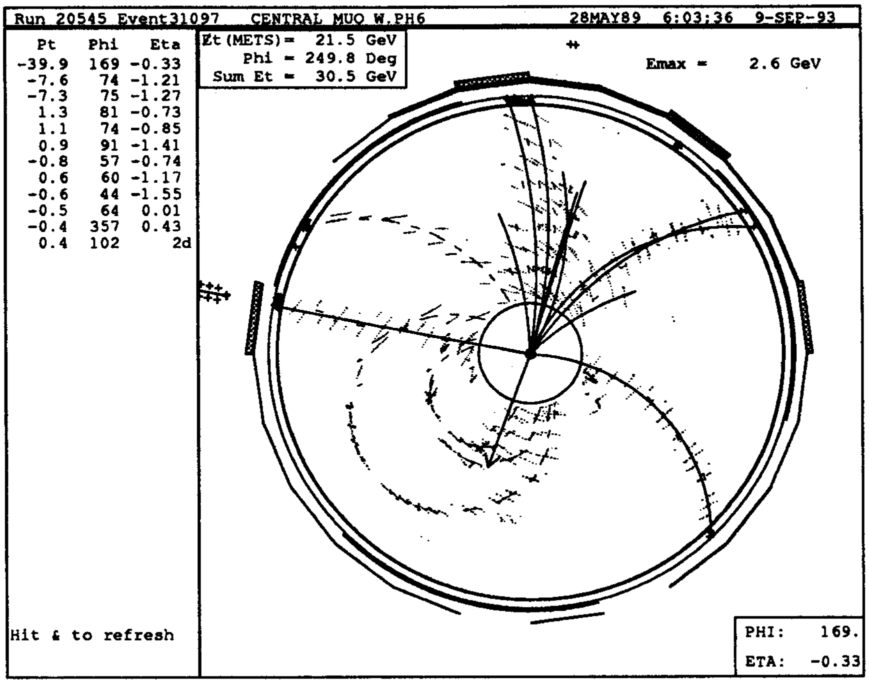

```
Run 20545 Event31097   CENTRAL MUO W.PH6           28MAY89  6:03:36  9-SEP-93
  Pt    Phi   Eta  Et(METS)=  21.5 GeV
-39.9   169 -0.33      Phi = 249.8 Deg
 -7.6    74 -1.21   Sum Et =  30.5 GeV
 -7.3    75 -1.27
  1.3    81 -0.73
  1.1    74 -0.85
  0.9    91 -1.41
 -0.8    57 -0.74
  0.6    60 -1.17
 -0.6    44 -1.55
 -0.5    64  0.01
 -0.4   357  0.43
  0.4   102    2d
```

```
Hit & to refresh
PHI:    169.
ETA:   -0.33
```

Figure 4.2: A beamline view of a $W \rightarrow \mu\nu$ event in CDF, with an opposing jet. The uncorrected $\not{E}_t$ is represented by the arrow, while the muon is the straight track with the CMU signal shown to the left.

analysis uses muons another post-reconstruction step is necessary to correct for the lack of a muon calorimeter energy deposition.

Figure 4.2 shows the situation for a typical W event. The jet is measured by the calorimeter signal but we must use the muon track p_t to calculate p_t^ν. The $\vec{\not{E}}_t$ is corrected by adding the muon track $\vec{p}_t$. We then subtract the muons calorimeter deposit from the new $\vec{\not{E}}_t$ value. This correction is expressed in the equation

$$\vec{\not{E}}_t^\nu = \vec{\not{E}}_t + \vec{p}_t^\mu - (E_{em}^\mu + E_{had}^\mu)\hat{n}, \qquad (4.2)$$

where E_{em}^μ and E_{had}^μ are the energy deposition in the electromagnetic and hadronic calorimeter towers traversed by the muon and $\hat{n}$ is a unit vector in the direction of the calorimeter tower.

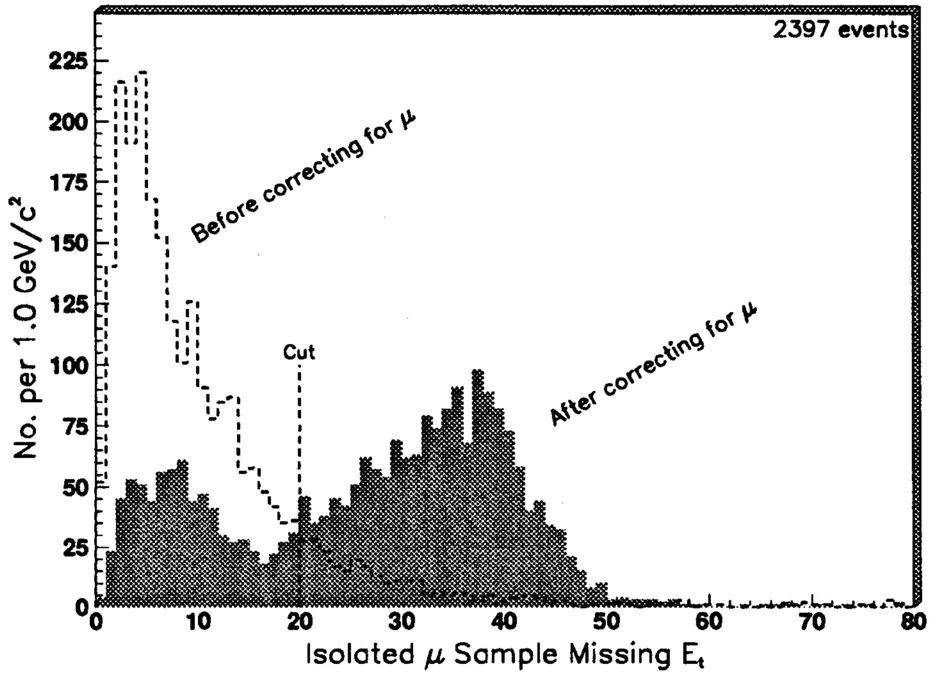

Figure 4.3: The Missing Transverse Energy for the data sample, both before ($\not\!\!E_t$) and after correcting for the minimum ionizing muon ($\not\!\!E_t^\nu$). The W's dominate the corrected distribution above $\not\!\!E_t^\nu \sim 20GeV$, while those events below 20 GeV are mostly QCD events, where one jet has fluctuated to mimic a muon. The dotted line at $/MET = 20$ GeV is the event selection criteria we shall impose for an event to be included in the W sample.

This calorimeter energy deposition must be subtracted because it was included in the original, uncorrected $\not\!\!E_t$ value.

Applying this correction to a W sample of high-p_t central muons (described below), the benefits are immediately seen. Figure 4.3 plots both the uncorrected $\not\!\!E_t$ and the corrected $\not\!\!E_t^\nu$ of the sample. The W events are those with a large value of $\not\!\!E_t^\nu$, while the events with smaller $\not\!\!E_t^\nu$ must be something else as the muon has for the most part been balanced by observables in the event. This analysis uses an $\not\!\!E_t^\nu$ requirement of $\not\!\!E_t^\nu \geq 20$ GeV to select W events.

4.2.4 Muon Reconstruction

A Central Muon Object(CMUO) is an object in the data that has passed basic muon selection requirements and corresponds to a physical muon. To identify a CMUO in the data the reconstruction requires that there be track segments in the CMU chambers and in the CTC system, and the extrapolated CTC track segment must match the location of the CMU track segment stub within $|\Delta x| \leq 17$ cm in the R-ϕ plane.

To be included in the muon data stream, an event must contain a CMUO satisfying two additional requirements: the track-stub matching distance must satisfy $\Delta x \leq 10$ cm, and the associated track must pass a trigger-dependent p_t requirement. For the high-p_t muon trigger of this analysis the p_t threshold was 9 GeV/c.

There is also an alternative type of muon object called a Central Minimum Ionizing Object (CMIO) which is useful for this analysis. These are particles satisfying the CMUO requirements except that no track segment is observed in the CMU chambers. This is useful when expanding the number of Z candidates which may be identified since we shall require a CMU signal from only one of the muons in the event. This allows us to accept muon data from a larger η range than that allowed by the CMU physical boundaries.

4.3 Muon Parameters

The CDF detector makes several measurements of muons from a $p\bar{p}$ event. By using these parameters and imposing selection criteria on them a cleaner sample of W and Z events is obtained. This section will briefly describe the muon parameters and the reasons for the cuts we impose.

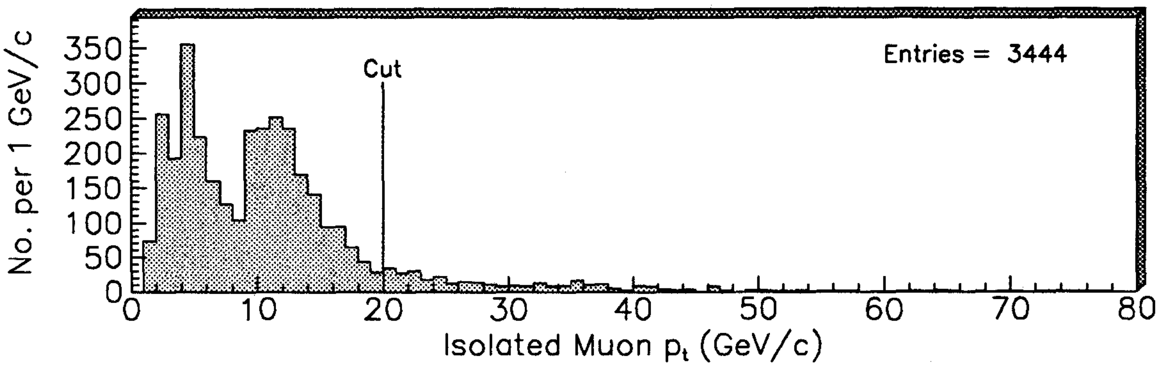

Figure 4.4: **The p_t of inclusive muons from CDF events. The muons of interest to this analysis are in the high-p_t region. The structure in the low p_t region is caused by triggering and reconstruction criteria.**
We shall impost a $p_t^\mu \geq 20$ GeV/c requirement on the events in the boson data sample.

4.3.1 Track p_t

The primary muon parameter that is used to select W and Z events is the muon transverse momentum. Since the masses of these bosons are higher than most physics processes resulting from $p\bar{p}$ collisions the leptons from their decays will have a higher momentum, allowing a simple p_t requirement to be quite effective in selecting boson events. There are relatively few other event types that will pass this first requirement as seen in Figure 4.4, where the p_t spectrum of several thousand CMUOs is plotted. We require $p_t^\mu \geq 20$ GeV/c for our data sample, as shown on the figure.

4.3.2 Calorimeter Energy

Muons may be further differentiated from other particles by a minimum ionizing signal in the calorimeter. Whereas a high-p_t electron will deposit nearly all of its energy into the calorimeter systems, a muon, being more massive, will leave very little. A typical muon will deposit 300 MeV in the electromagnetic calorimeter and 2 GeV in the hadronic system. Figure 4.5.{a,c} shows these peaks quite clearly for CMUOs with $p_t \geq 18$ GeV, while Figures 4.5.{b,d} shows

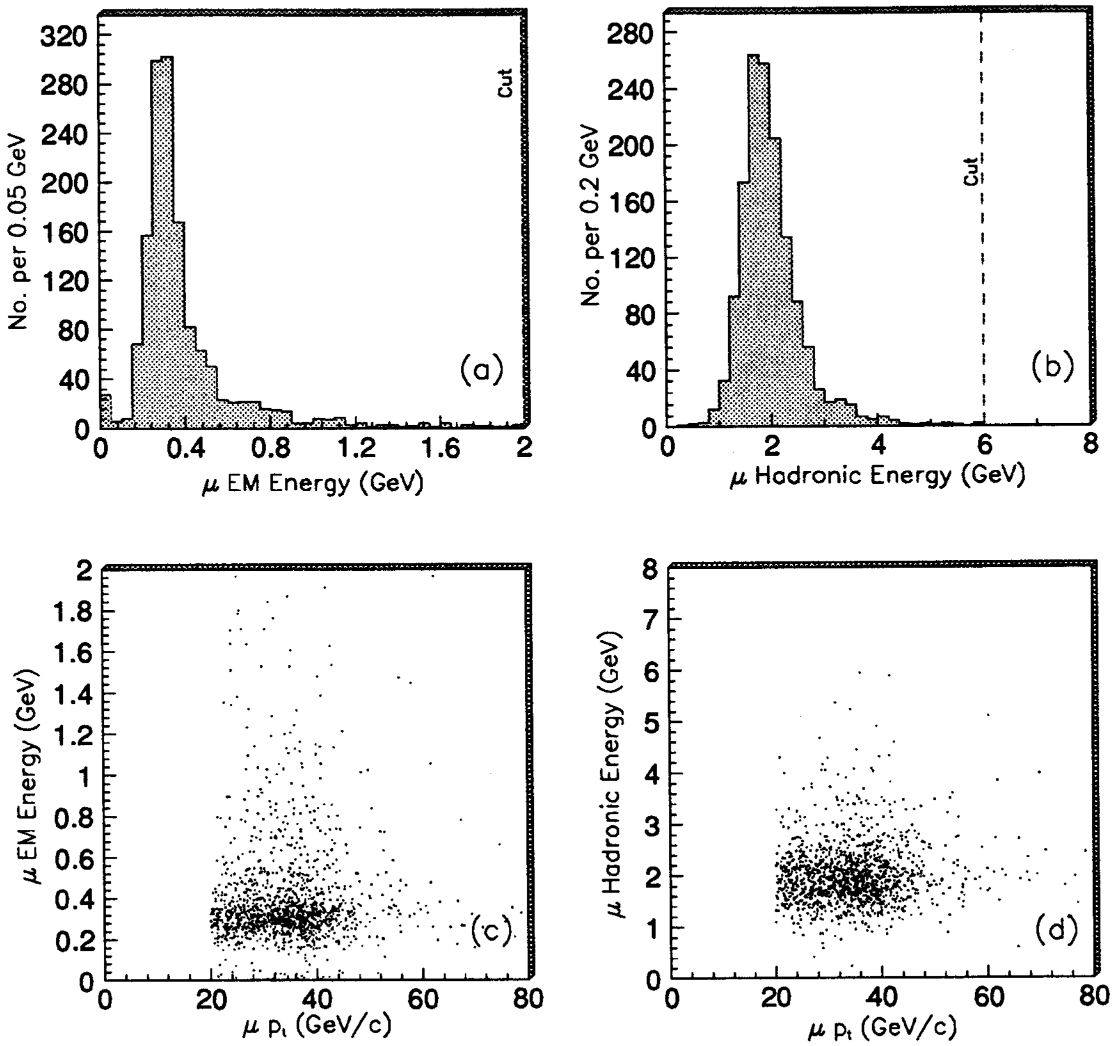

Figure 4.5: The muon calorimeter deposition and its dependence on the muon p_t.

that the energy deposition does not depend on the p_t of the muon. For this analysis we impose a requirement of $E_{em} \leq 2$ GeV and $E_{had} \leq 6$ GeV.

4.3.3 Track-'stub' matching

We require that the signal in the CMU is associated with the high-p_t track. Other particles such as pions can leave a minimum ionizing signal in the calorimeter but will usually not continue beyond into the CMU chambers. The punchthrough probability for a hadron to penetrate the

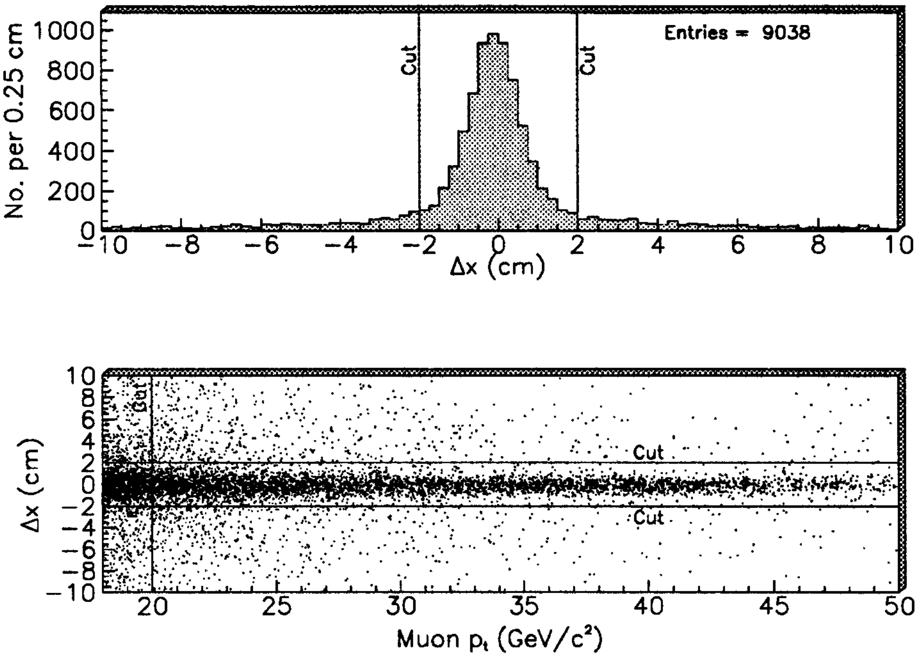

Figure 4.6: A plot of the CTC track – CMU stub matching distance in the ϕ direction, and the dependence of this parameter on the track p_t. The cuts we impose are shown in the figure.

CMU has been measured at less than 1 in 50 for 57 GeV particles [34, 35, 36]. It is also possible that a low-p_t muon stub might happen to line up with a high-p_t track, so we impose a maximum distance requirement for this track-stub match.

Figure 4.6 shows the CTC track–CMU stub matching distance in the ϕ direction (measured at the first layer of CMU cells), and the dependence of this value on the track p_t. This data was taken from the high-p_t muon sample. The default matching requirement imposed by the reconstruction code is 10 cm, but this can be reduced significantly without penalty. We require $|\Delta x| \leq 2$ cm to reduce background contamination in the sample.

4.3.4 Vertex Location

Control of the location of the $p\bar{p}$ collision along the z axis is limited by the proton and antiproton bunch length. Figure 3.5 shows this distribution is a gaussian centered at z=0 with σ = 30 cm. We insure that the muons originate in the well-understood central region of the detector and avoid the ends of the tracking chamber by imposing a 2σ requirement for the event vertex location. This has the added benefit of eliminating some cosmic rays which may be mistaken for muons from W and Z events.

4.4 Event Selection

The selection requirements for the W and Z events should be similar so that some of the systematics of the individual W and Z cross section measurements will cancel. This analysis concentrates on the selection of an isolated, high-p_t muon in the fiducial region of the CMU detector. Additional criteria are then imposed; either requiring a second muon (for Z's) or seeking indirect evidence of a neutrino.

4.4.1 Common High-p_t Muon Sample

As a first step of the analysis, we defined an inclusive sample of high-p_t central muon events. The requirements for the sample were initially not stringent, as this common sample was meant to be used for a variety of analysis. An event was required to have a candidate CMUO with the following characteristics:

a. $p_t \geq 18$ GeV/c;

b. $E_{em} \leq 2$ GeV and $E_{had} \leq 6$ GeV in the electromagnetic and hadronic calorimeter towers traversed by the extrapolated muon track;

c. $|\Delta x| \leq 10$ cm, requiring that the track and stub are associated.

Imposing these requirements resulted in a sample containing 11,485 events.

Once the 1988-89 run was over and all of the event reconstruction was completed, we were presented with an opportunity to refine the CTC track reconstruction. Since the second method of track-finding discussed previously is more suited for this type of measurement the 11k events in the above sample were reprocessed. This removed kinked tracks which might result from decay-in-flight candidates and decrease the background in the sample. Later in this analysis we compensate for the possibility of losing a good track on the second pass by introducing an efficiency term.

4.4.2 Removing Bad Runs

During the run there was a minimum bias trigger to randomly select events during the data taking. These events were used to study some overall characteristics of the data, and to check that no inherent biasing of the data sample was taking place. One way this was accomplished was to determine the mean and sigma of $\vec{\not\!E}_t$ projections in two directions, $\not\!E_t^x$ and $\not\!E_t^y$, which are gaussian and centered at 0 for good data [37]. Several runs were flagged as having large $\vec{\not\!E}_t$ offsets or sigmas and were removed from the sample.

Routine maintenance and calibration of the detector indicated that some channels in the Plug Electromagnetic (PEM) detector were dead for part or all of the run, with several runs having greater than 30 dead channels. These dead channels would affect the $\vec{\not\!E}_t$ summation, thereby affecting the neutrino p_t^ν measurement. These runs were explicitly removed from the data sample. The integrated luminosity for these runs was 170 nb^{-1}, or roughly 3.4% of the data. All of these problems and the runs involved are summarized in Table 4.1.

Run Number	Problem
$\leq$ 17265, 17278	Broken muon trigger
16785	Large $\not\!\!E_t$ mean and sigma in minimum bias data.
17469,17475,18869-18947	Large number of PEM dead channels.
17512-17516	Luminosity & Trigger problems.

Table 4.1: Bad runs removed from the data sample. The run numbers for the '88-'89 data-taking were in the range 15339-20607.

4.4.3 Cosmic Ray Rejection

Many of the high p_t muons in the sample are expected to be cosmic rays, either alone in the event or happening concurrently with a real $p\bar{p}$ interaction. A cosmic ray filter was written which executed the following tests on each muon candidate in the event [38]. If the muon candidate satisfied any of these tests, it was flagged as a cosmic ray for future rejection.

a) Muon not attached to any vertex with $|z_{vtx}| > 60$ cm;

b) Muon candidate is separated from a 'primary' event vertex by > 5 cm in the z direction or >0.5 cm in the radial direction;

c) There is a track with $p_t > 10$ GeV within 2° of back-to-back in ϕ, which is

  i) two dimensional, or

  ii) separated from a primary event vertex (see above), or

  iii) has a low fraction of possible CTC hits, or

  iv) has too few track segments;

d) There is a three dimensional back-to-back track in ϕ within 0.2 of equal-and-opposite η. Also, the combination (muon + opposing track) has a travel time through the CTC of > 4.5 ns.

These requirements formed an acceptable cosmic ray filter, the efficiency of which shall be examined later.

4.4.4 The Integrated Luminosity of the Data Sample

The instantaneous luminosity of the beam is calculated by accelerator physicists using

$$\mathcal{L} = \frac{a n_p n_{\bar{p}} f_{col}}{4\pi \sigma_x \sigma_y},$$

where n_p and $n_{\bar{p}}$ are the number of (anti)protons in a bunch, f_{col} is the bunch collision frequency, $\sigma_{x(y)}$ are the $x(y)$ size of the bunch (where the beam moves in the z direction, typically $\sigma_{x(y)} \sim$ 50 μm) and a is a parameter describing the longitudinal shape of the bunch. The measurement of the instantaneous luminosity at the CDF interaction region as described in section 3.2.3.

Once the bad runs and cosmics have been removed, we determine the total integrated luminosity of the data sample. This is determined during the data taking by the Beam-Beam Counters and calculated by using the time integral of equation 3.1. The BBC rate was read out during the run, allowing us to calculate the integrated luminosity of the final data sample. The total integrated luminosity for the runs in the data sample is $\int \mathcal{L} dt = 3.54 \pm 0.24$ pb^{-1}.

4.4.5 The Fiducial Regions of CMU and CTC

The fiducial region of a detector is defined as that part of the detector where the response is both well understood and relatively uniform. We must know the fiducial regions of the CMU and the CTC so that an accurate efficiency measurement may be made for the detector systems and, more importantly, so that we may make a measurement of the geometric acceptance of the systems. The size of the fiducial region will determine the geometric acceptance of the detector

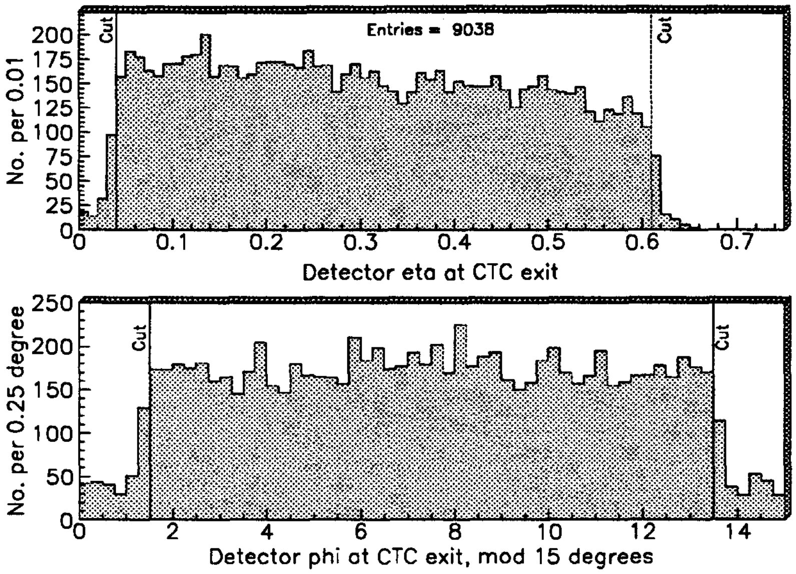

Figure 4.7: Plots with all of the CMU wedges 'folded' into one unit so that the fiducial regions can be easily determined. The fiducial limits obtained are shown.

so we try to increase the fiducial volume as much as possible to increase the event collection rate.

For this purpose we look at the high-p_t data sample and observe where the extrapolated track of the muon strikes the CMU chambers. In Figure 4.7 all of the wedges have been 'folded' into one 15 degree wedge so that the fiducial region of a typical wedge can be determined. The CMU fiducial region is, in local coordinates for each wedge, $0.04 < |\eta| < 0.61$ and $1.5^\circ < |\phi| < 13.5^\circ$. These limits are included in the figure.

In order to find as many Z events as possible we shall impose less stringent requirements on the second muon in an event. We do not require that the second muon traverse a CMU chamber but only that it have a well-measured track. The fiducial region of the CTC must therefore be determined. Since the CTC was designed to cover all of ϕ, we need only determine it's efficiency in the η direction. Recall that the CTC consists of 9 superlayers but is of limited length; a particle at a sufficiently high η will exit the end of the CTC while traveling through

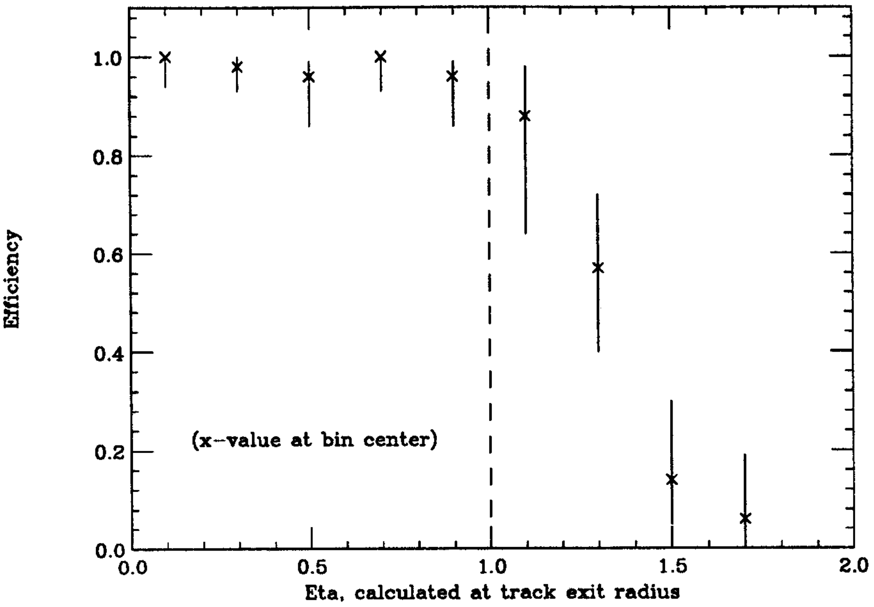

Figure 4.8: The CTC tracking efficiency taken from $Z^0 \rightarrow e^+e^-$ events. The maximum muon eta we allow in the data sample is indicated by the dashed line.

only a subset of the superlayers. We examine a sample of $Z^0 \rightarrow e^+e^-$ events which are detected solely by seeking the electron energy clusters in the calorimeter. A CTC track pointing to the energy cluster is then sought. The tracking efficiency of the CTC versus the η of the track is plotted in Figure 4.8. The CTC tracking efficiency remains high until around $|\eta| \sim 1.0$, at which point it begins to fall rapidly. This is discussed in more detail in section 6.4.

As another check we compare the output of a fast detector simulation with the Z^0 data. This simulation is discussed in more detail in Chapter 5. In particular the ratio of Z events which are seen as a CMU-CMU muon pair (subscript "mm") to those seen as a single CMU muon and a high-p_t CTC track (subscript "mt") is plotted versus the location where the track exits the CTC. As seen in Figure 5.9 the simulation and the data agree out to approximately $|\eta| = 1.0$, at which point they diverge. This divergence is caused by the increasing inefficiency of the CTC in the data as tracks begin exiting the endplates before traversing all superlayers,

Chamber	η	ϕ
CMU	$0.04 < \|\eta\| < 0.61$	$1.5^\circ < \|\phi\| < 13.5^\circ$
CTC	$\|\eta\| = 1.0$	no limits

Table 4.2: The fiducial limits of the CMU and the CTC chambers.

while in the simulation no such degradation in track efficiency is modelled. This determines the CTC fiducial region as $|\eta| \leq 1.0$. These fiducial requirements are summarized in Table 4.2.

4.4.6 'Re-Tracked' High-p_t Central Muon Sample

Returning to the high-p_t muon sample and examining the interesting muon in the event, we require:

1. Reject bad runs and cosmic rays, as defined previously;

2. Event contains a CMUO which

    a. had $p_t^{old} \geq 18$ GeV/c prior to retracking, and has ${p_t}^{new} \geq 20$ GeV/c [1];

    b. $E_{em} \leq 2$ GeV and $E_{had} \leq 6$ GeV in the calorimeter tower traversed by the track;

    c. has $|z_0 - z_{vtx}| < 5$ cm for some $p\bar{p}$ vertex with $|z_{vtx}| < 60$ cm;

    d. has track-stub matching $|\Delta x| \leq 10$ cm;

    e. the track extrapolates to be within the fiducial region of the CMU. If the track extrapolates to be outside the CMU fiducial region but due to multiple scattering there is a CMU stub, the event is rejected.

4. Event has a traceable trigger - Level 0 BBC trigger and Levels 1 and 2 muon trigger.

---

[1] For the rest of this analysis, we shall simply refer to the p_t of the track, with the understanding that we are discussing the new, i.e. 'retracked' p_t

These requirements leave 3425 events, including non-isolated muons which will be used for background studies. A non-isolated muon is one that has a significant amount of calorimeter energy deposited around the tower traversed by the muon. This type of calorimeter signal is indicative of a gluon jet in the event that is either colinear with the muon or has fluctuated to appear to be a muon, in either case something that is probably not a primary muon from a W or Z decay.

4.4.7 'Golden' Muons

A 'golden' muon is defined as one that passes all of the above requirements and in addition:

- A CTC–CMU track match of $|\Delta x| \leq 2$ cm;
- the muon is isolated: $ISO < 0.1$, where

$$ISO \equiv \frac{\Sigma_{0.4}E_t - E_t^{\mu}}{p_t^{\mu}}, \tag{4.3}$$

  $\Sigma_{0.4}E_t$ is the transverse energy in a cone of $\Delta R = \sqrt{\Delta\phi^2 + \Delta\eta^2} = 0.4$ around the muon, E_t^{μ} is the transverse energy deposited in the calorimeter tower traversed by the muon, and p_t^{μ} is the traverse momentum of the muon track.

- muon stub not in wedge 17-East of the CMU for runs 20278-20446, as the associated HV cable for those chambers was discovered to be unplugged during the data-taking.
- muon stub not in the middle chamber of wedge 2-East, where we observed unusually high values of Δx

These requirements defining a golden muon are the most stringent we shall impose on the muons in W and Z events. They are the common requirements for both types of events that will allow cancelling of some efficiency terms when calculating the final measurements.

4.4.8 Z Sample

A Z event is identified by two high-p_t tracks. Two views of a Z event are shown in Figure 4.9. In the data we define a Z candidate as an event that has one golden muon, and another CMUO or CMIO which passes requirements 3a-3c above and which passes completely through superlayer 8 of the CTC. We define these loose muon selection criteria as 'silver' cuts. This leaves us with 117 events, with the invariant mass distribution shown in Figure 4.11. Of these events, 109 are in the mass window $65 \leq M_{\mu\mu} \leq 115$ GeV/c^2 where

$$M_{\mu\mu} = \sqrt{2 \cdot |\vec{p}_1||\vec{p}_2|[1 - cos(\theta)]}, \tag{4.4}$$

and θ is the three dimensional opening angle of the muons. A Level 2 muon trigger is also required for the event, rejecting one event. One event did not have a BBC Level 0 trigger, so it is rejected. We also require that if the second muon projects to the fiducial region of the CMU system then it must have a stub associated with it, to simplify the $A_Z \cdot \varepsilon_Z$ term (discussed in section 8.2). This leaves us with 106 Z-candidates. The cuts are summarized in Table 4.3.

4.4.9 W Sample

Figure 4.10 shows a plot from the high-p_t muon data of the two primary kinematic parameters we use to identify W events. A W candidate is an event containing 1 golden muon and also has $\not\!\!E_t^\nu \geq 20$ GeV. The event is also required to not be in the Z sample, and is required to have a

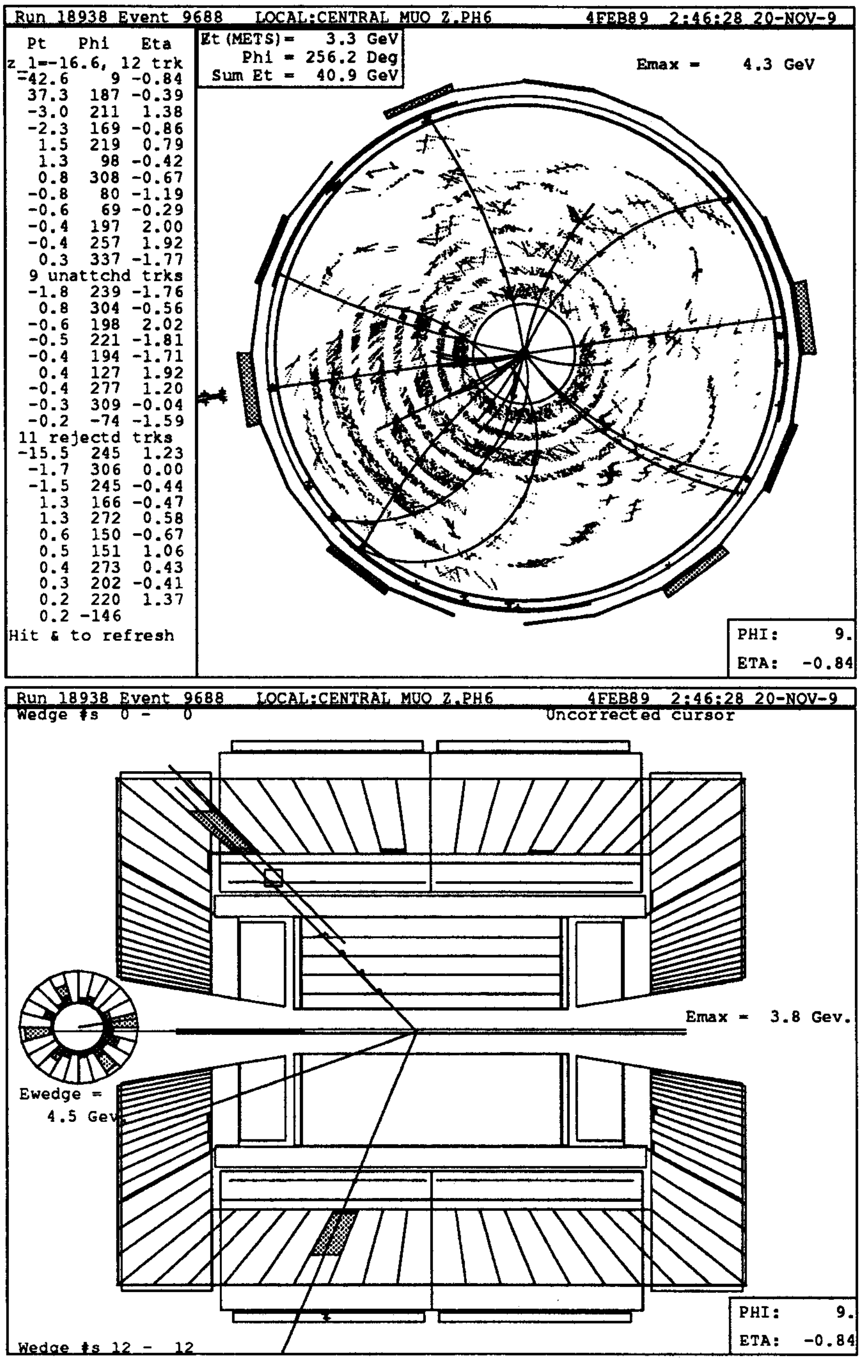

```
Run 18938 Event 9688    LOCAL:CENTRAL MUO Z.PH6        4FEB89  2:46:28 20-NOV-9
  Pt   Phi   Eta
z_1=-16.6, 12 trk
 -42.6    9 -0.84
 37.3  187 -0.39
 -3.0  211  1.38
 -2.3  169 -0.86
  1.5  219  0.79
  1.3   98 -0.42
  0.8  308 -0.67
 -0.8   80 -1.19
 -0.6   69 -0.29
 -0.4  197  2.00
 -0.4  257  1.92
  0.3  337 -1.77
 9 unattchd trks
 -1.8  239 -1.76
  0.8  304 -0.56
 -0.6  198  2.02
 -0.5  221 -1.81
 -0.4  194 -1.71
  0.4  127  1.92
 -0.4  277  1.20
 -0.3  309 -0.04
 -0.2  -74 -1.59
11 rejectd trks
-15.5  245  1.23
 -1.7  306  0.00
 -1.5  245 -0.44
  1.3  166 -0.47
  1.3  272  0.58
  0.6  150 -0.67
  0.5  151  1.06
  0.4  273  0.43
  0.3  202 -0.41
  0.2  220  1.37
  0.2 -146
Hit & to refresh
```

```
Et(METS)=   3.3 GeV
   Phi = 256.2 Deg
 Sum Et =  40.9 GeV
```

```
Run 18938 Event 9688    LOCAL:CENTRAL MUO Z.PH6        4FEB89  2:46:28 20-NOV-9
Wedge #s  0 -   0                                  Uncorrected cursor
```

Figure 4.9: Two views of a Z event in the CDF detector. The top picture is a view looking along the beamline into the CTC, where the two high-p_t (low curvature) tracks are easily identified. The bottom is a side view of the same event, showing that only one of the muons is at an η that traverses the CMU chambers. The other muon is at too high an η to be recorded in the CMU, but is still identified by the track.

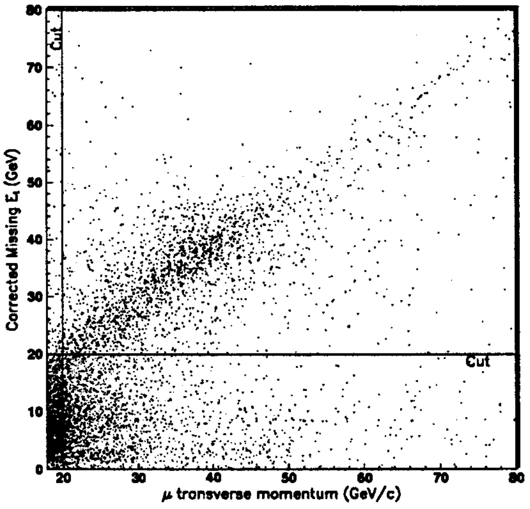

Figure 4.10: A plot of the $\not\!\!E_t^\nu$ vs. muon p_t in the high-p_t data sample. The W events are those with $\not\!\!E_t^\nu \sim p_t^\mu$. The cuts imposed on the values are shown.

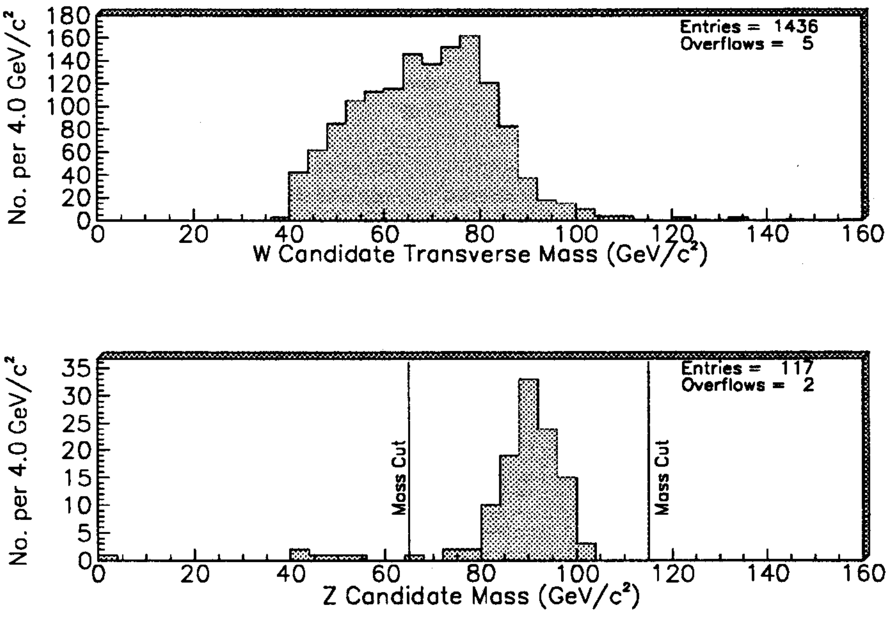

Figure 4.11: The invariant masses of our W and Z samples, where for the W a transverse mass is plotted. The mass cuts for the Z are included.

<table>
<tr><th>W events</th><th>Z events</th></tr>
<tr><td colspan="2">Golden Muon:
$p_t^\mu \geq 20$ GeV/c
$E_{em} \leq 2$ GeV
$E_{had} \leq 6$ GeV
$|z_{vtx}| \leq 60$ cm
$|\Delta x| \leq 2$ cm
$ISO \leq 0.1$
μ within fiducial CMU</td></tr>
<tr><td>Silver Muon
$p_t^\mu \geq 20$ GeV/c
$E_{em} \leq 2$ GeV
$E_{had} \leq 6$ GeV
$|z_{vtx}| \leq 60$ cm
μ within fiducial CTC</td><td>Neutrino
$\not{E}_t^\nu \geq 20$ GeV</td></tr>
<tr><td>$65 \leq M_{\mu\mu} \leq 115$ GeV/c</td><td>Not in Z sample</td></tr>
<tr><td colspan="2">Pass Cosmic & Bad Run filters
Level 2 Muon Trigger</td></tr>
<tr><td>106 Z events</td><td>1436 W events</td></tr>
</table>

Table 4.3: Summary of W and Z selection criteria.

Level 2 muon trigger and a Level 0 BBC trigger. This leaves us with 1436 events. Figure 4.11 shows the transverse mass of the W's, defined as

$$M_t = \sqrt{2|\vec{p}_{t1}||\vec{\not{E}}_t^\nu|[1 - cos(\Delta\phi)]}, \tag{4.5}$$

where $\Delta\phi$ is the two dimensional opening angle of the muon and $\vec{\not{E}}_t^\nu$. It is necessary to use the transverse mass for W events because the method which was used to reconstruct the neutrino doesn't yield p_z information. The z information for the neutrino cannot be reliably measured because of event-by-event fluctuations in the p_z of the underlying event which cannot be measured due to the fact that CDF doesn't cover all of the solid angle. The cuts for this sample are summarized in Table 4.3.

Chapter 5

Kinematic and Geometric Acceptances

When counting events to determine a cross section, the process of event selection naturally breaks into two terms; one for the geometrical acceptance of the detector components and one for the efficiency of the muon and neutrino selection criteria. The first accounts for the probability that the $W(Z)$ decay products will strike an active region of the detector while the second is the probability that a muon or neutrino will pass the identification requirements we impose. We use a Monte Carlo detector simulation to measure the acceptance. We impose the same kinematic requirements for the simulated muons as are imposed on the data. The p_t selection criteria of both the muon and neutrino have been included in the detector simulation discussed below.

5.1 Monte Carlo Generators

We use a fast Least Order Monte Carlo (LOMC) generator which simulates only the subprocess diagram $q\bar{q} \to W(Z^0) \to ll$ to generate four-vectors for the leptons resulting from the boson decays. The generator includes polarization effects and the correct matrix element for the decays $W \to \mu\nu$ and $Z^0 \to \mu^+\mu^-$, and uses a relativistic Breit-Wigner shape extending to ± 25 widths [39]. The Drell-Yan photon diagram for $p\bar{p} \to \gamma \to \mu^+\mu^-$ is indistinguishable from the production and decay of a Z^0 and will therefore have a small effect on our measurement. The Drell-Yan contribution is not explicitly included, but we shall correct for this effect later.

5.1.1 Selecting the Proton Structure Function

A significant uncertainty in the theoretical calculation of the $W(Z)$ cross sections is due to poorly measured parton distribution functions. The functions usually arise from a fitting procedure which includes the results of several experiments. The differences in the functions depend upon which fitting procedure and data was used. We use HMRSB [10] because it has its origins in data from collider experiments, it is well understood and it is also widely used, facilitating comparisons of results within CDF [40] and with UA1 and UA2 experiments at CERN [41, 42].

5.2 The Fast Detector Simulation

A simple detector model is used to determine the kinematic and geometrical acceptances. The simulation was derived from one originally written for use in the CDF $W \to \mu\nu$ mass measurement [43]. Because the mass measurement was sensitive to uncertainties in event structure and detector resolution, the basic simulation is sufficient for this analysis. The $W \to \mu\nu$ mass measurement, however, was not concerned with the fraction of events that were captured by the detector, only the event characteristics that affected the mass. The cross section measurement is intimately concerned with the fraction of events observed, hence the simulation was modified to include the CTC and CMU detector fiducial regions and to reject muons outside of those regions.

5.2.1 The Detector Simulation Model

The detector simulation model depended on several input parameters which were studied separately. We shall discuss the simulation for Z events in detail since, as seen below, it necessarily contains the W event simulation.

The least order generator produces bosons at rest, so we introduce an artificial p_t^{boson} distribution as observed in the data. The boson decay products are boosted using a boson p_t taken randomly from the distribution resulting from the CDF W and Z $d\sigma/dp_t$ measurements [44, 45], which agree well with the theoretical predictions [46]. The p_t spectra are acceptance and resolution corrected and are shown in Figure 5.1. Corrections introduced to account for other higher-order effects in the decays are discussed later.

The simulation models the spread of the event origin in the longitudinal direction. In real CDF events, the location of the interaction vertex along the Z axis is smeared along a gaussian, centered at $z = 0$ with $\sigma = 30$ cm. We introduce this spread into our simulated event, and reject events with $|z_{vtx}| > 60$ cm as is done in the data.

The CTC measures track curvature, not the transverse momentum. To simulate the momentum resolution of the CTC, the p_t of the generated muons is transformed into a curvature value, which is smeared by adding a random value from a gaussian distribution with $\sigma = 0.0020$,

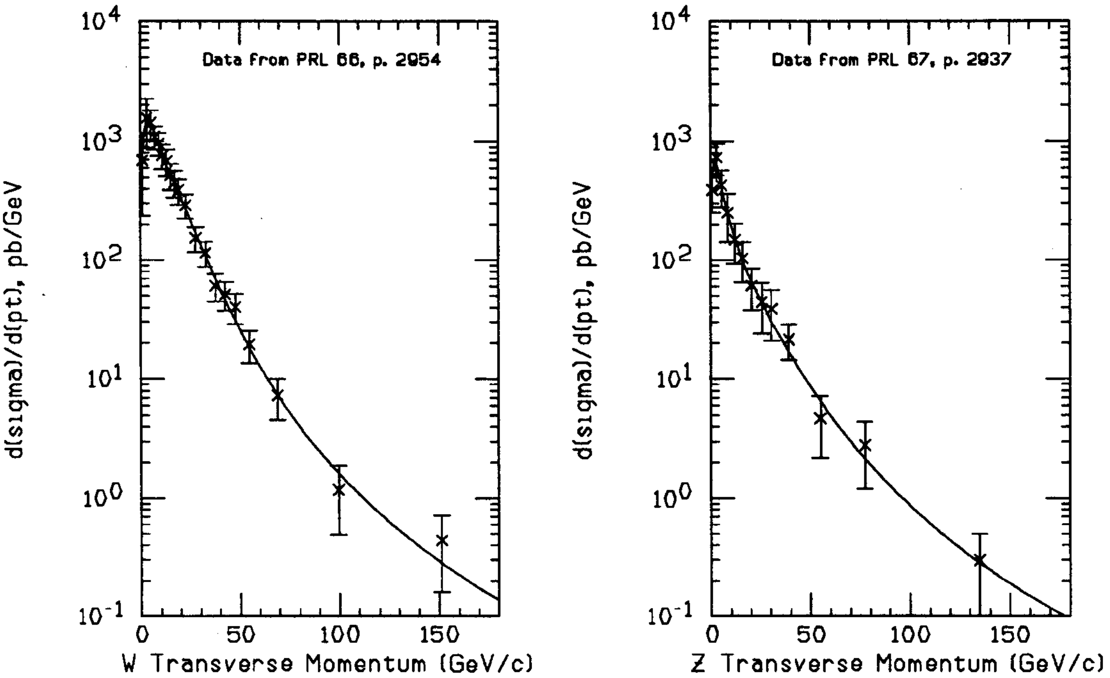

Figure 5.1: The W and Z transverse momentum spectra that were used for the detector simulation, taken from the CDF $d\sigma/dp_t$ analysis.

and then translated back into p_t. We require each muon to satisfy $p_t \geq 20$ GeV/c; those that do not will remain "unseen" for the rest of the simulation.

A complication arises when counting these events. While there is only one type of W event, where it is either accepted or not, a Z event may be one of several types. If both muons from the Z decay are observed in the CMU chambers, both of them have a chance of firing the Level 2 muon trigger. If only one muon is in the CMU and the other is a high-p_t track in the CTC, then there is only one chance to fire the trigger. These two event types have different detection efficiencies, and are considered separately. An added complication is introduced when one realizes that a Z event with only one good CMU muon may be observed as a W event and erroneously inflate the W signal. These factors are taken into account by counting these event topographies separately when calculating acceptances.

We extrapolate the remaining muons using the smeared p_t and assign a flag for each muon, determining whether it projects to the fiducial regions of the CMU, the CTC, or neither. If neither, that muon will remain "unseen" for the rest of the simulation. If both muons are detected in the simulation a mass requirement of 65 GeV/c^2 $\leq M_{\mu\mu} \leq$ 115 GeV/c^2 is applied, as done in the Z data.

After the extrapolation and flagging of both muons, Table 5.1 is consulted to determine the class of the simulated Z event. A Z event may be one of four classes depending on how, or if, the muons are detected. These classes are: muon-muon, muon-track, muon-unseen, or completely undetected according to our requirements. A track-unseen event is considered as undetected, due to the event selection requirement of at least one golden CMU muon. By cross-referencing the table by the fiducial classes of the two muons, a Z event classification is obtained. We count events where both muons are observed in the muon chambers as $N_{m\cdot m}$, and events where one muon is in the CMU and the other is seen only in the CTC as $N_{m\cdot t}$. Thus we count the acceptances of each Z classification separately, as

$$A_{x\cdot x} = \frac{N_{x\cdot x}}{N_{total}}.$$

The most restrictive type of Z event is one in which both of the muons have $p_t \geq 20$ GeV/c and both extrapolate to the fiducial region of the CMU. We define f to be the fraction of accepted Zs which are these types of events, calculated as

$$f = \frac{A_{m\cdot m}}{A_Z}$$

	CMU	CTC	Unseen
CMU	$A_{m\cdot m}$	$A_{m\cdot t}$	"W-like"
CTC	$A_{m\cdot t}$	*rejected*	*rejected*
Unseen	"W-like"	*rejected*	*rejected*

Table 5.1: A table of Z event classifications in the detector simulation for measuring acceptance. An event's class is determined by the fiducial regions to which it's muons propagate. W events, in contrast, are of only one type, and are simply seen or unseen.

where $A_Z = A_{m\cdot m} + A_{m\cdot t}$. In the data this comprises about 1/3 of the Z sample. The other 2/3 are Z's with one CMU muon and one high-p_t CTC track. If a simulated Z event is one of these two types, it is counted and the simulation continues with the next event. If the event is "W-like", the simulation continues with a W simulation to determine whether the event will appear in the W sample.

A Z event in which one muon propagates to the muon chambers and the other remains unseen, either due to event geometry or failing the p_t requirement, will have a high probability to be seen as a W event because the unseen muon will resemble a neutrino. The acceptance of these false Ws is measured by allowing any simulated events that reach this stage to continue the simulation as a W event. This acceptance number, A_{ZW}, will be useful later as a method of measuring the Z contribution to the W data sample, and allow a correction to be applied for this background source.

For events with a single muon, either a simulated W event or a misidentified Z event, the effects of the spectator hadrons in the event must be simulated. The underlying energy from these hadrons will greatly affect the measurement of the neutrino p_t in W events. We therefore describe the underlying event model in detail.

The p_t of the boson is balanced by recoil energy in the form of jets. However, only a portion of the jet energy is observed in the detector. The response to lower p_t jets typical of the boson data is depressed by calorimeter non-linearities and magnetic field effects. Low p_t charged particles will spiral in the magnetic field and never reach the calorimeter, and even those jet components with $p_t < 800$ MeV/c may be misread because they will curl enough to defeat the projective nature of the CEM and CHA towers. We use a jet degradation function of the form

$$E_t^{jet} = \frac{p_t^{jet}}{f(p_t^{jet})},$$

with $f(p_t^{jet})$ shown in Figure 5.6 to model the calorimeter jet energy response.

The degraded E_t^{jet} is smeared with $\sigma = 0.85\sqrt{E_t^{jet}}$, to model the jet energy resolution of the calorimeter. The determination of this resolution is discussed below.

Once the E_t of the jet is smeared an underlying event vector is added to the simulated event. The p_t of the neutrino is calculated by looking at the missing transverse energy and using momentum conservation,

$$\Sigma \vec{E}_t^f = \Sigma \vec{E}_t^i = 0.$$

Since we expect the underlying event to be isotropic in the transverse plane, the total calorimeter resolution of $\sigma = 0.43 + 0.0013 \cdot \Sigma E_t$, which is explained in greater detail in 5.2.2.3 is used for the underlying event vector. The parameter ΣE_t is defined as the scalar sum of the underlying transverse energy in the detector, discounting the energy deposition directly related to the W muon or the opposing jet. A value for the event ΣE_t is randomly chosen from the distribution shown in Figure 5.7.d to calculate the resolution for gaussian smearing in the x and y direction. These values are then combined with the degraded and smeared jet. The calculation of the neutrino p_t is nearly complete, and needs only one further correction to complete the event simulation.

In the data we subtract the small calorimeter signal deposited by the muon; so the same is done in the simulation. A muon will leave an energy deposition in the calorimeter of approximately 3 GeV, so a 3 GeV transverse energy vector (pointing in the direction of the simulated muon) is subtracted from the calculated neutrino $\vec{p}_t$ to get a final value of $\vec{p}_t^{\nu}$. This value corresponds to the corrected $\vec{\not{E}}_t^{\nu}$ in the data sample. We require $\vec{\not{E}}_t^{\nu} \geq 20$ GeV/c, to count the event as a W.

5.2.2 Including the Higher Order Corrections

Real W and Z events are a combination of Feynman diagrams of all orders. In the LO generator, however, only the simplest diagram is used and it is assumed that the muons produced in boson decay are back-to-back. Although we artifically add a boson p_t boost to the Monte Carlo events, we anticipate there might be some other higher-order effects on the event geometry.

For higher values of the boson p_t we therefore wish to use the event geometry that comes from a next-to-leading-order diagram. We use the PAPAGENO W+1 jet Monte Carlo generator [47]. The total acceptance will then be defined as a linear combination of the LO and NLO generators, as

$$A_t = \rho A_0 + (1-\rho)A_1 \tag{5.1}$$

where ρ is the fraction of the boson data that comes from a low boson p_t, and A_0 and A_1 are the acceptances found from the LO and NLO generators, respectively. We find ρ as follows:

i) Obtain the W p_t spectrum found from PAPAGENO;

ii) overlay with the same spectrum from the data sample;

Lower W p_t cut	8	10	12	14	16 GeV/c
$(1-\rho)$	0.55	0.45	0.38	0.32	0.27

Table 5.2: Fraction of Events from Leading Order Diagram versus p_t cut

Acceptance term	LO M.C.	Papageno 1 jet	Combined
W acceptance (A_W)	$19.08 \pm 0.06\%$	$18.76 \pm 0.06\%$	$18.96 \pm 0.06\%$
Z acceptance			
A_Z	$14.90 \pm 0.05\%$	$16.21 \pm 0.05\%$	$15.40 \pm 0.05\%$
f	$0.310 \pm 0.002\%$	$0.310 \pm 0.02\%$	$0.310 \pm 0.02\%$
'One-legged Z' (A_{ZW})	$20.36 \pm 0.06\%$	$19.33 \pm 0.06\%$	$19.97 \pm 0.06\%$

Table 5.3: The nominal acceptance values for muonic W's and Z's using the LO and NLO generators. The LO simulation uses $p_t^{W(Z)} \leq$ 12GeV, while the PAPAGENO NLO uses $p_t^{W(Z)} > 12$ GeV. The weighted average is shown on the right. The uncertainties are statistical only.

iii) find the boson p_t above which the two spectra have the same shape. We define this value as p_t^0, above which the NLO diagram dominates the boson process;

iv) ρ is the fraction of the observed spectrum lying below p_t^0.

Figure 5.2 shows the measured CDF p_t^W spectrum from [44] overlaid with the Papageno $W + 1$ jet p_t^W spectrum. At very large p_t the statistics in the data put a large uncertainty on the measured p_t^W. We try to match in the region $20 < p_t^W < 30$ GeV/c and look at the value of p_t^W below which the two curves diverge, which is at $p_t^W = 12$ GeV/c. Table 5.2 is made from the parametrization of the PRL W spectrum. We use $\rho = 62\%$ (p_t^0 of 12 GeV/c) and vary it down to 55% and up to 80%.

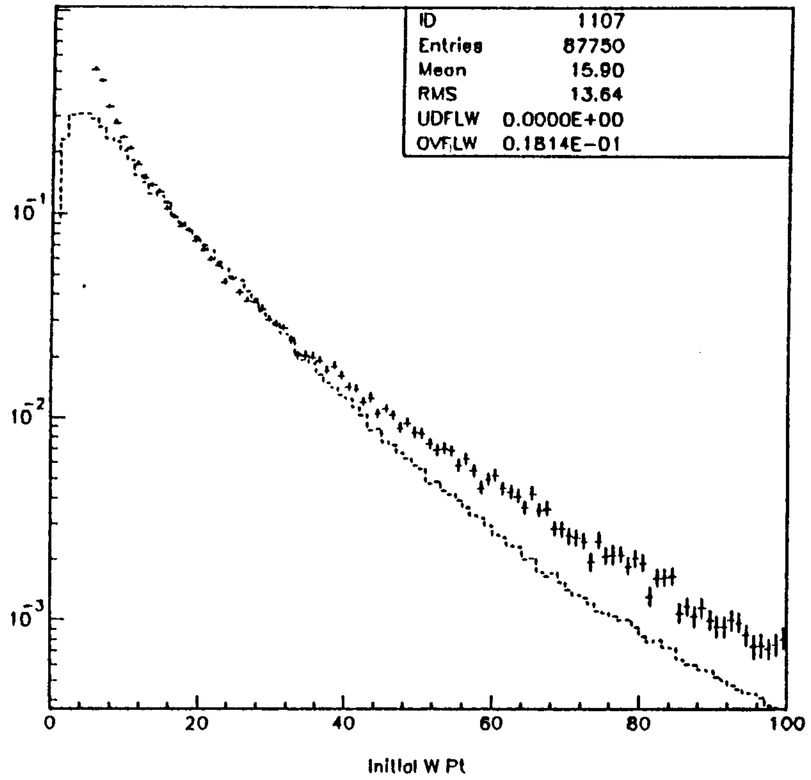

Figure 5.2: The measured W p_t spectrum from [44] (dash) overlaid with the spectrum from the PAPAGENO W+ 1 jet Monte Carlo generator (crosses). The data contains almost no events above 40 GeV/c, where the statistical uncertainty is large. The measured spectrum is the same one shown in Figure 5.1.

5.2.2.1 Measuring the Jet Degradation Function

In the model the basic jet degradation function has three parameters; a high E_t^{jet} behavior, a low E_t^{jet} behavior, and a transition E_t where the degradation changes from one to the other. The model assumes that the degradation is linear both above and below the transition point.

For the high E_t^{jet} behavior we use the CDF standard jet energy correction [48] and compare corrected versus uncorrected jet energies. The CDF standard correction is a complex function of jet parameters, so we wish to simplify it for use with our detector simulation. Figure 5.3 shows a scatter plot of the corrected jet energy versus the raw jet energy for our W sample, while 5.4 shows the mean value of the corrected jet energy versus the raw jet energy with a fit overlaid. We find that the correction yields

$$E_t^{jet}(true) = 3.7 + 1.15 \cdot E_t^{jet}(measured)$$

which when averaged over the jet energies in our W data sample, approximates

$$E_t^{jet}(true) = 1.3 \cdot E_t^{jet}(measured).$$

We use this value for the nominal high E_t^{jet} degradation.

By plotting the ratio of the corrected jet energy to the raw jet energy as a function of η as done in Figure 5.5 we can estimate a statistical uncertainty for this value. The range of 1.1 to 1.6 includes nearly all of the points, so we conservatively use a statistical uncertainty of $(^{+0.4}_{-0.2})$.

For lower values of E_t^{jet} a different degradation is expected for the jet because more of the component particles of the jet will spiral in the magnetic field without ever reaching the calorimeter. This happens to jet particles with $p_t < 400$ MeV/c, resulting in a lower jet energy

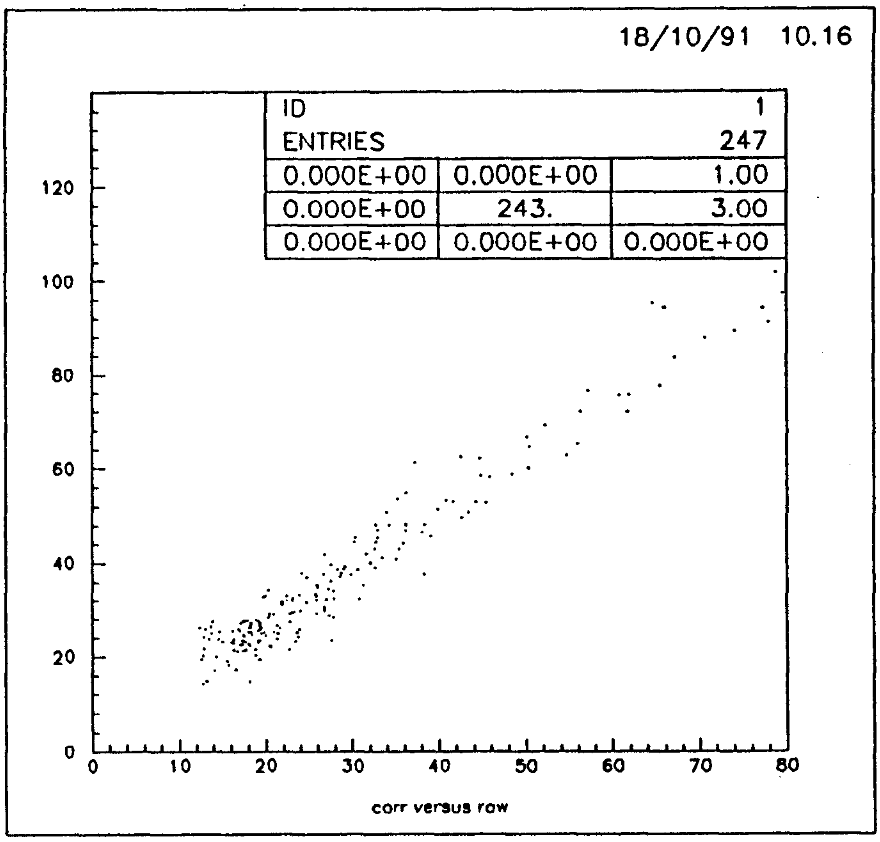

Figure 5.3: A scatter plot of the corrected jet energy versus raw jet energy of the W sample. Each axis has units of GeV.

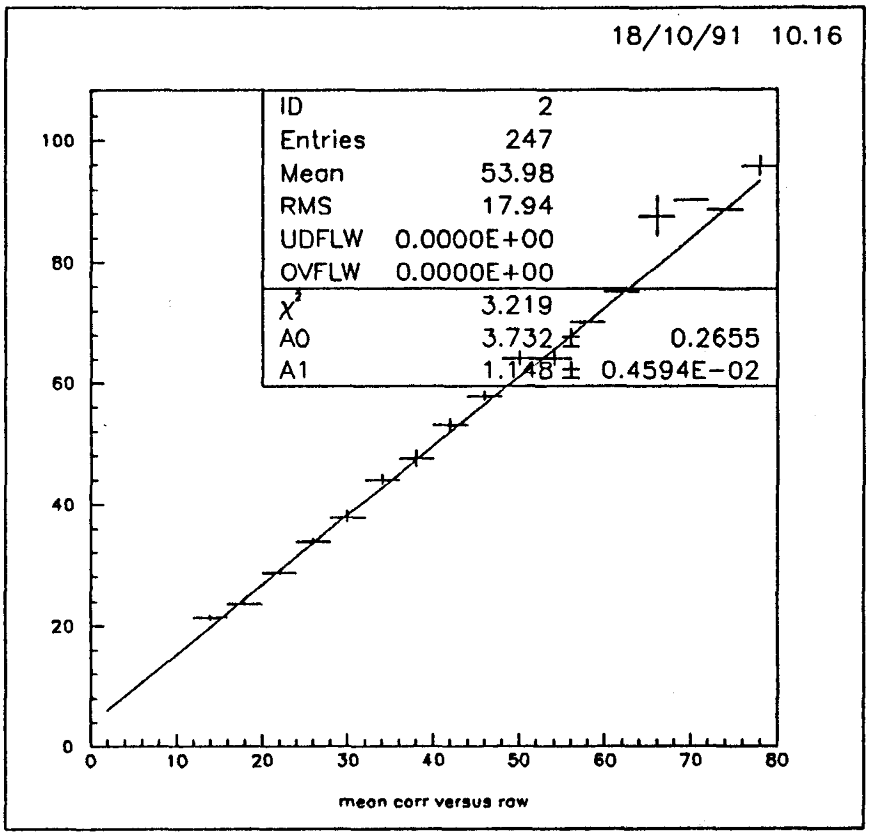

Figure 5.4: The mean corrected jet energy versus raw jet energy of the W sample, where each axis is in GeV. This is the same data as Figure 5.3 except that a fit to the mean of each 4 GeV wide bin is found.

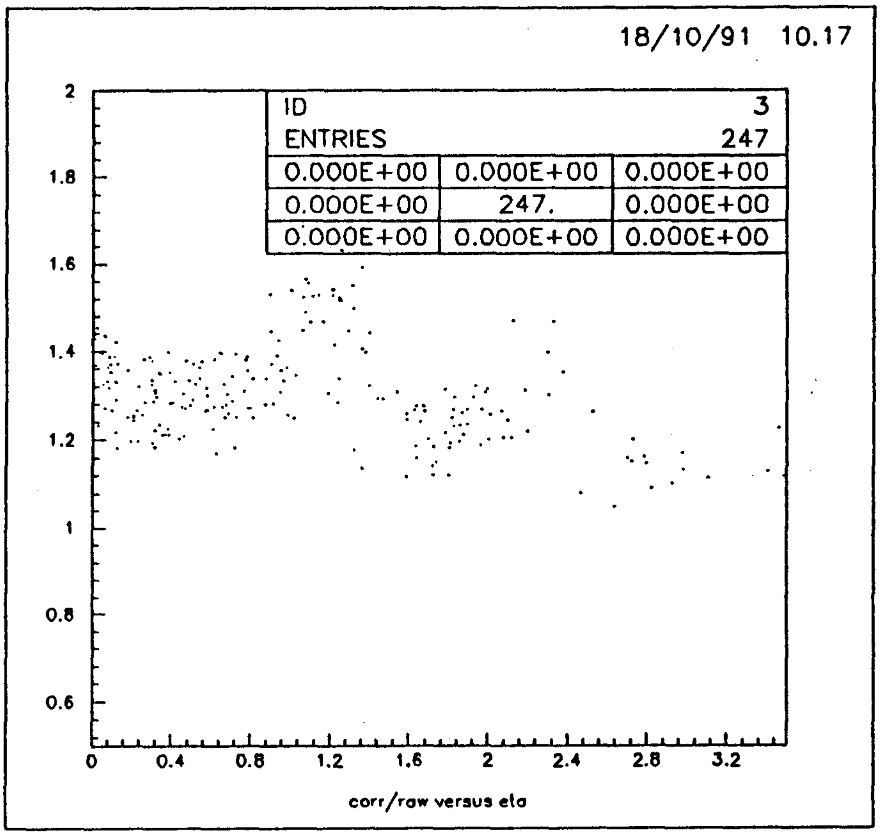

Figure 5.5: The ratio of the corrected jet energy over the raw jet energy measured in the detector versus the η of the jet.

bin center($p_{\|\|}^Z$) (GeV)	$p_{\|\|}^{ee} - p_{\|\|}^{cal}$ (GeV)	$p_{\|\|}^{ee}/p_{\|\|}^{cal}$
1.	0.11 ± 0.40	1.12 ± 0.50
3.	1.36 ± 0.28	1.83 ± 0.30
5.	2.80 ± 0.52	2.27 ± 0.50
7.	3.55 ± 0.34	2.03 ± 0.20
9.	3.97 ± 0.57	1.79 ± 0.20
11.	5.28 ± 0.24	1.92 ± 0.09
15 ± 5	5.00 ± 0.47	1.50 ± 0.26
28.0 ± 8.5	8.46 ± 1.52	1.43 ± 0.21

Table 5.4: The relationship between corrected and raw jet energy as function of p_t^Z

deposition in the calorimeter. To find the low E_t^{jet} endpoint we refer to Table 5.4. This table, obtained from $Z^0 \rightarrow e^+e^-$ data, shows the component of the Z p_t which is parallel to the bisector of the two electrons opening angle minus the opposing jet energy calculated using the calorimeter. The ratio of these values also are shown in the table and plotted in Figure 5.6. For the low E_t^{jet} endpoint degradation we use the values from the second and third bin, where we find a mean of 2.0 ± 0.3. The figure also shows the resulting jet degradation function with uncertainties overlaid.

We use the bisector of the electron opening angle because the electrons may radiate colinear radiation, which would affect the momentum measurement of the track. The opening angle is thus a measurement that has more event-by-event stability. We do not suffer by using the track p_t in the muon analysis because of the calorimeter tower energy limits we impose.

When the high p_t^{jet} behavior of the jet degradation was found, the data sample which was used was limited to jets with $E_t > 30$ GeV. Thus we define this as the transition point. We see in Figure 5.6 that a lower value of approximately 15 GeV for the transition is also consistent with the data, so we use 30^{+0}_{-15} GeV as the transition value.

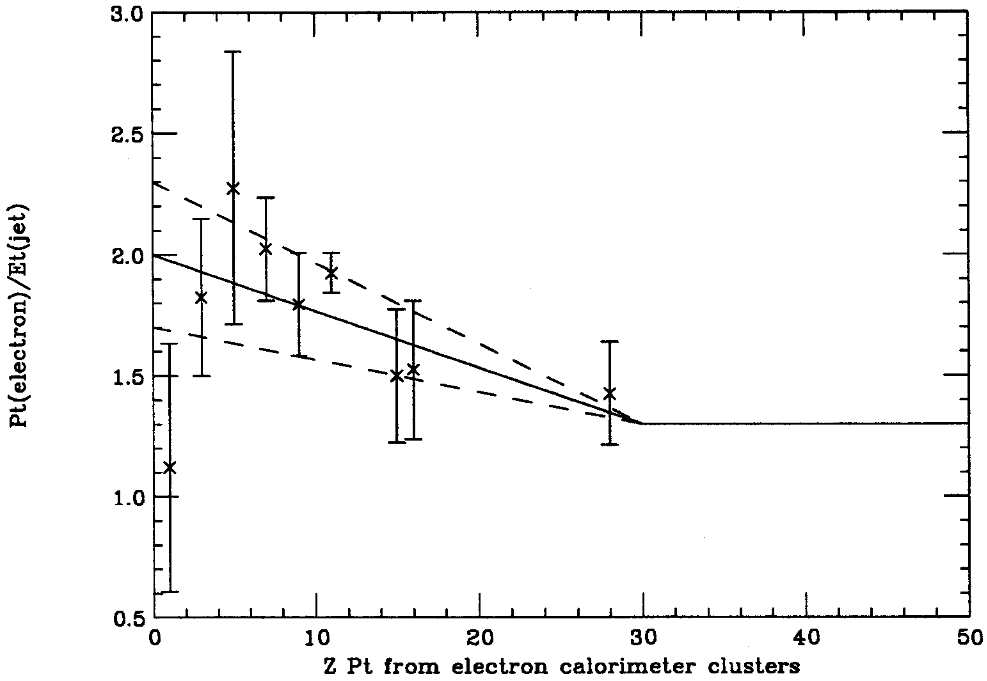

Figure 5.6: The p_t^Z parallel to $Z^0 \to e^+e^-$ bisector calculated from the electron calorimeter clusters divided by the recoil jet energy deposition, versus the p_t^Z calculated from the electron calorimeter clusters. The line is the jet energy degradation function used in the model. Uncertainties in the model are also shown for the low p_t region.

5.2.2.2 Obtaining the ΣE_t distribution

The ΣE_t distribution was obtained from $W \to e\nu$ and $W \to \mu\nu$ data. Figure 5.7 shows the progression from the raw ΣE_t for each data sample to a usable distribution. In part figure (a) we show the raw ΣE_t for both samples. The difference between the samples is caused by the calorimeter energy deposition of the electrons and muons. In part (b) the calorimeter energy deposition of the $e(\mu)$ has been subtracted. The next task is to subtract the E_t of the jet that is opposing the boson. The Wp_t is divided by the 'mean' jet degradation value of 1.75 and this value is subtracted from the event ΣE_t, with the results shown in part (c) of the plot. The similarity between the two samples at this point confirms that we understand these contributions to W event structure, and increases confidence in the detector simulation model.

Plot (d) shows the sum of the $W \rightarrow e\nu$ and $W \rightarrow \mu\nu$ corrected distributions. This is the distribution we use in the simulation.

5.2.2.3 Obtaining the Calorimeter E_t Resolution

The underlying event caused by the spectator hadrons is assumed to be isotropic in the transverse plane due to momentum conservation. Any deviation from this is therefore due to random fluxuations in the calorimeter energy measurement, which is modeled as a calorimeter E_t resolution. This value is obtained from a study of minimum bias events from which the $\not\!\!E_t$ is plotted against the total scalar energy in the event. Dividing the plot into 5 GeV bins and fitting a line to the points on the figure indicates that the calorimeter E_t resolution is $\sigma = (0.43 \pm 0.0007) + (0.0013 \pm 0.00003) \cdot \Sigma E_t$, as seen in Figure 5.8.

5.2.2.4 The Origin of the Calorimeter Jet Energy Resolution

The factor of $\sigma = 0.85^{+0.3}_{-0.2}\sqrt{E_t^{jet}}$ that is used for smearing the jet energy measurement in the simulation has two independent origins. By using single pions impacting on a calorimeter segment in the test-beam a factor of 0.83 ± 0.02 GeV$^{\frac{1}{2}}$ was obtained [48]. In the CDF $W \rightarrow \mu\nu$ mass analysis [43], a factor of $0.85^{+0.3}_{-0.2}$ GeV$^{\frac{1}{2}}$ was determined by measuring the distribution of the jet E_t recoiling against a measured $Z^0 \rightarrow e^+e^-$ p_t, and then subtracting the underlying event resolution in quadrature [43]. To be conservative we use the larger uncertainties. We find the model is insensitive to this parameter.

5.2.3 Comparison with Data

By using the simulation and applying the same basic kinematic requirements ($p_t^\mu \geq 20$ GeV/c, $\not\!\!E_t^\nu \geq 20$ GeV) to the simulated events as in the data, the acceptance of the detector to W and

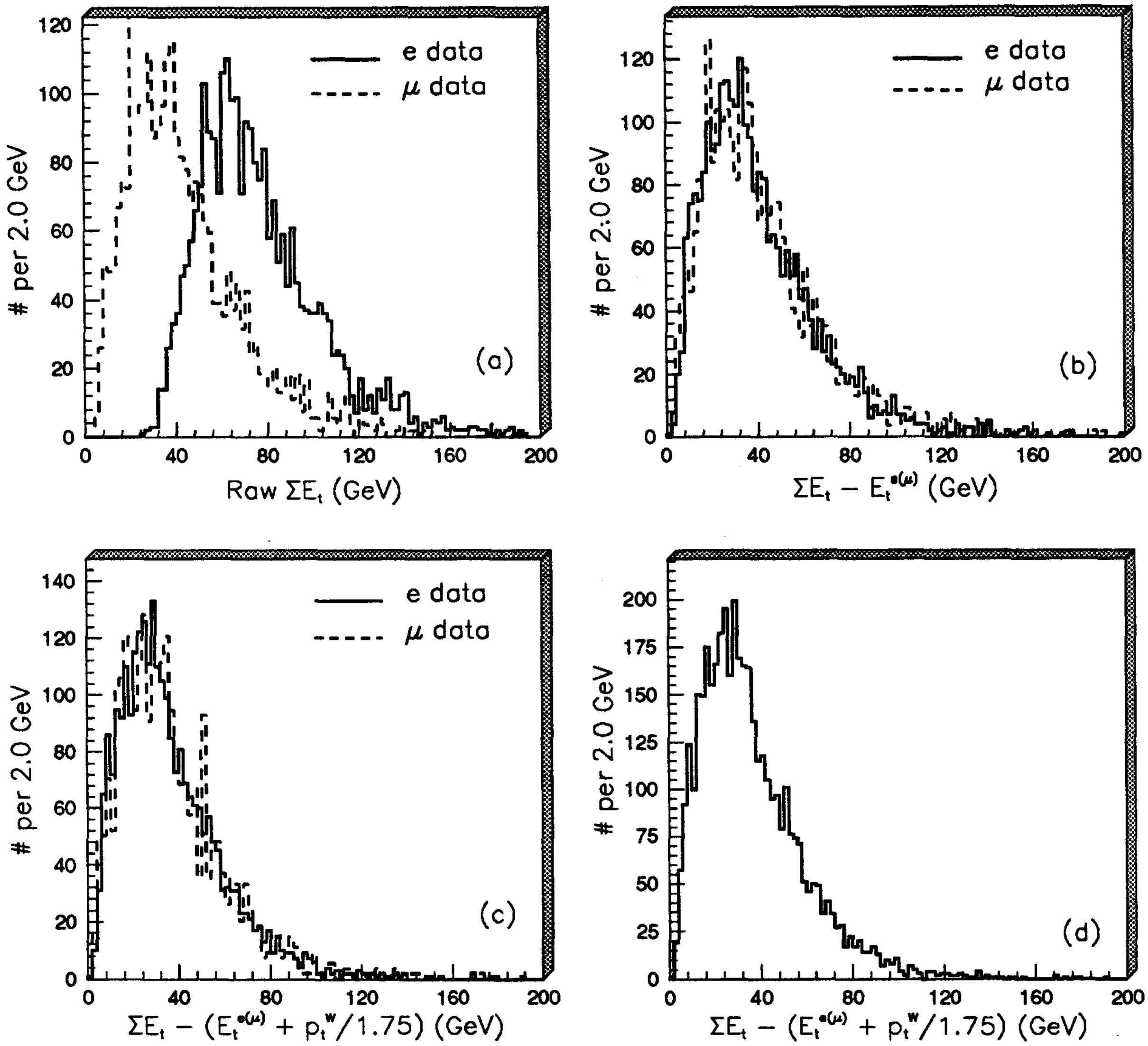

Figure 5.7: Four plots showing the progression from raw ΣE_t for e and μ W events to that used in the simulation. The details of the operations are in the text.

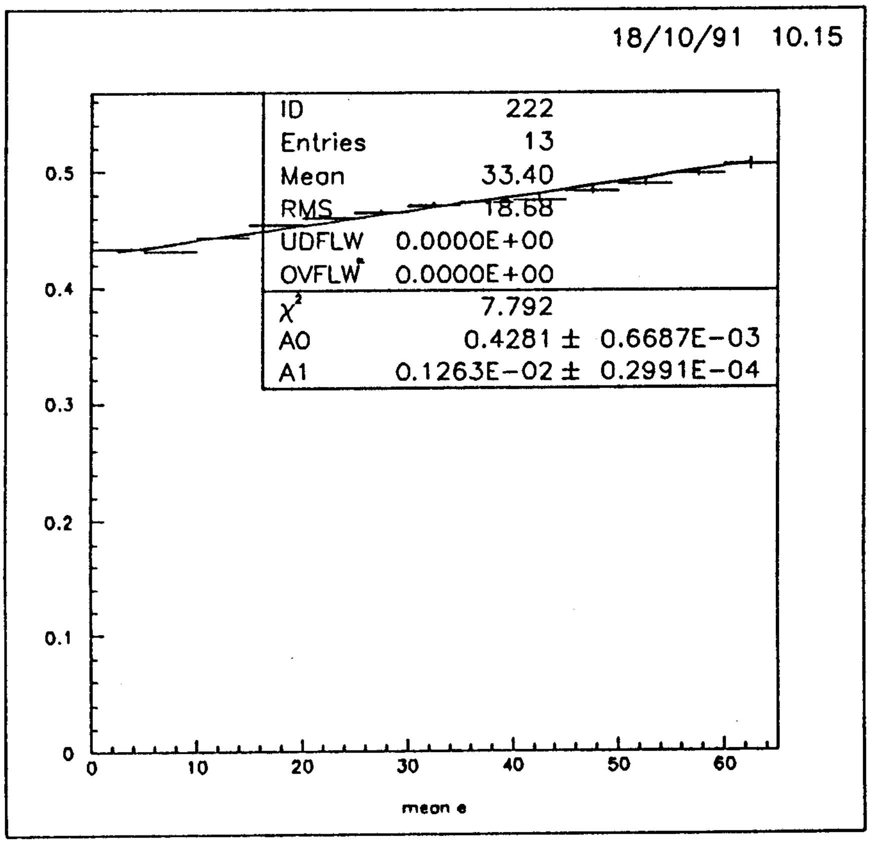

Figure 5.8: Taken from minimum bias events, a plot of the event $\not{E}_t$ versus the total scalar E_t seen in the event. We get our values from the fit superimposed on the plot.

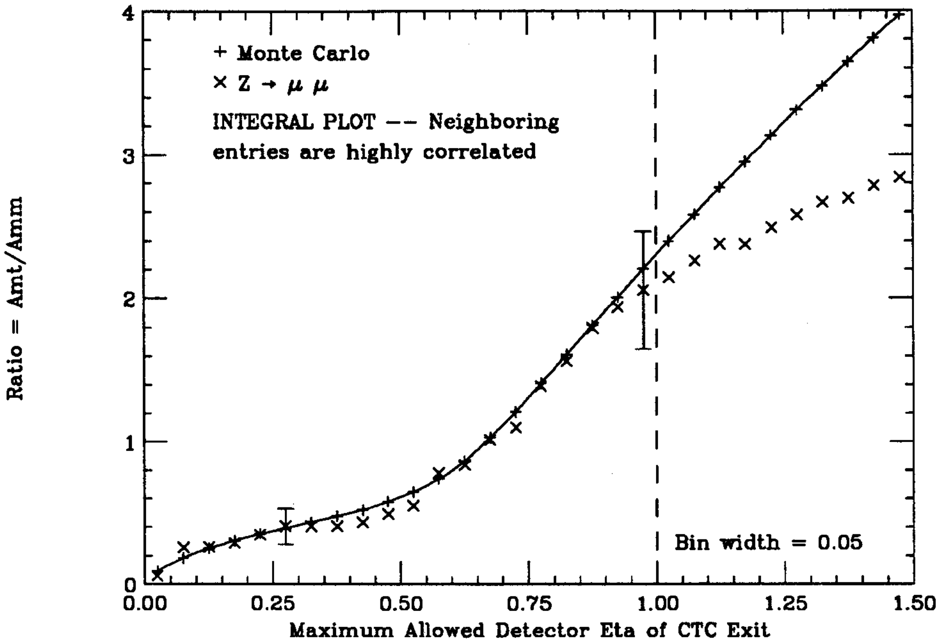

Figure 5.9: CTC integral efficiency, with sample uncertainties. The ratio of muon-muon and muon-track Z events for the simulation and the data agree below $\eta \sim 1.0$. The divergence in the region $|\eta| \geq 1.0$ reflects the reduced CTC efficiency for high-η tracks. The dashed line represents the highest muon η we shall allow into the sample.

Z muonic events is measured. As a check on the model we compare the simulation results with the data.

For the Z's we compare the ratio A_{mt}/A_{mm} from the Monte Carlo with the observed number of events N_{mt}/N_{mm} in the data, corrected for efficiency. Recall that the "mm" subscript means that both muons traverse the fiducial region of the CMU chambers, while the "mt" subscript means that one of the muons was detected only as a high-p_t track that traversed all CTC superlayers. Figure 5.9 summarizes the result, where η is calculated for the point where the track leaves the CTC volume. The data and Monte Carlo agree well until around $\eta \sim 1.0$ or 1.1, where CTC efficiency begins to suffer as tracks leave the CTC without hitting all axial superlayers. This result agrees with Figure 4.8 and the tracking efficiency study.

For the W events we examine several projections of the underlying event $\vec{E}_t$, as seen in Figure 5.10. The underlying event $\vec{E}_t$ is the vector sum of all the $\vec{E}_t$ in the event, excluding the W. Figure 5.10 shows the magnitude of $\vec{E}_t$ and the components both parallel and perpendicular to the muon direction for both the W data and the Monte Carlo, normalized to the number of W events. The agreement between the simulation and the data indicates that we have a reasonable model of W-like events.

5.2.4 Acceptance Uncertainties

We initially run the detector simulation with all parameters at their nominal value to obtain the nominal acceptances, listed in Table 5.3. Once these values were obtained the simulation parameters are adjusted by their uncertainty values. The parameters that are complicated to estimate are described in detail below.

If two parameters are correlated in their effect on the acceptance, examining them independently will yield under- or overestimates of their effect on the acceptance uncertainty. Therefore, several of the parameters to the detector simulation were studied concurrently. The results are presented so that each associated set of parameters is listed together in Table 5.7. The systematic uncertainties for the geometrical acceptances comes from uncertainties in the Monte Carlo inputs. These are

- the structure functions,
- contributions from higher-order diagrams,
- the modeling of the underlying event for W's,
- the boson p_t spectrum,

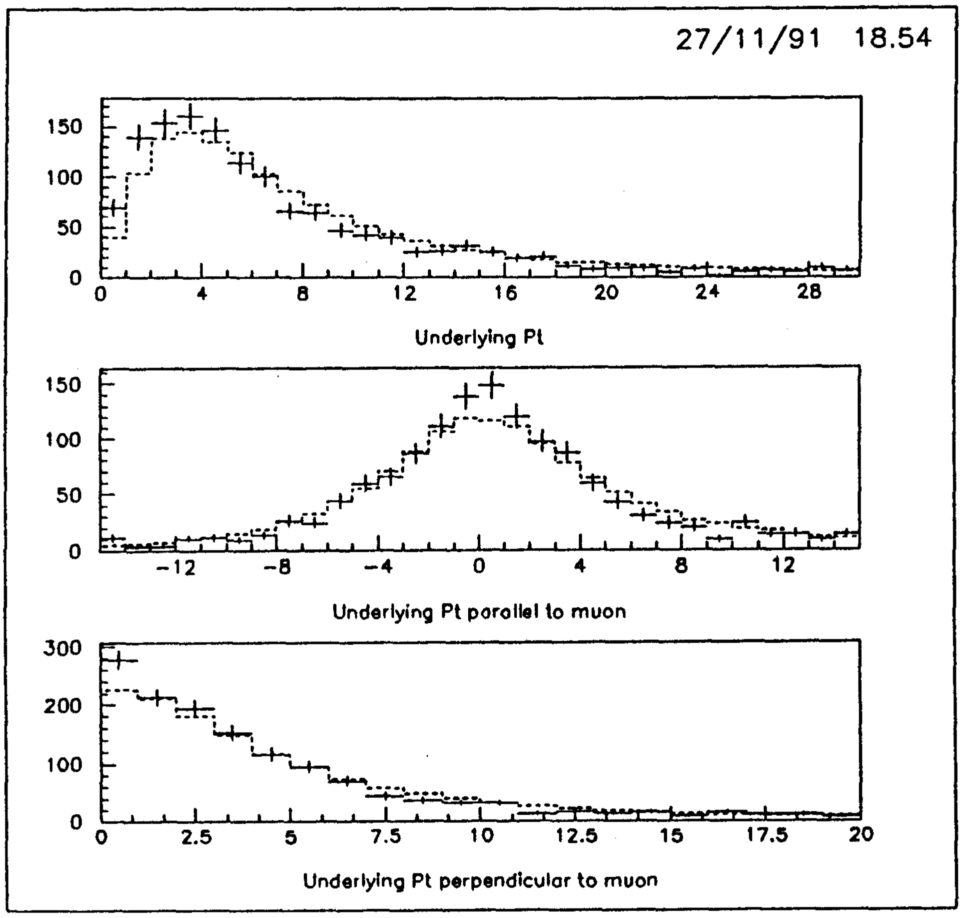

Figure 5.10: Comparison of the underlying event energy for the *W* sample (crosses) and the fast simulation (dashes). Shown are the scalar sum and the components parallel and perpendicular to the muon direction.

- Standard Model parameters – $sin^2\theta_W$, M_W,
- detector resolution effects,
- modeling of the energy deposition of the unseen second muon leg for A_{ZW}, and
- effects of 2 jet events.

5.2.4.1 Systematics due to Choice of Proton Structure Function

Although we use what we considered the optimum proton structure function for this analysis, there were several others that would also have been appropriate. All of these structure functions were consistent with the data that generated them, and the main reason for choosing HMRSB was for ease of comparison with other measurements.

The uncertainty due to our choice of structure function is determined by recalculating the acceptance for each of five different structure function sets: DFLM1,2, and 3 [49], and MT-B1 and B2 [50]. Table 5.5 lists the results for each set. We use half of the range found for each set for the uncertainties.

When we calculate the ratio of cross sections we see that it is the spread of the ratio A_W/A_Z that should be used (see eq. 8.5). This is because some of the impact of structure functions on the result will cancel in the ratio, decreasing the overall systematic uncertainty.

5.2.4.2 Systematics on the Higher Order Contribution

When we included the effect of higher-order terms into the simulation (section 5.2.2) we used a value of $p_t^0 = 12$ GeV/c for the transition from the LO generator to the Papageno NLO generator, which gave a mixing value of $\rho = 62\%$. We measure the uncertainty by varying

Str. func.	A_W	A_Z	f	A_{ZW}	A_W/A_Z
HMRSB	18.71 ± 0.06	15.20 ± 0.05	0.310 ± 0.002	19.83 ± 0.06	1.231 ± 0.006
DFLM1	18.46	14.35	0.308	20.15	1.286
DFLM2	18.28	14.39	0.308	20.07	1.270
DFLM3	18.27	14.27	0.305	20.23	1.280
MT-B1	17.87	14.17	0.307	20.00	1.261
MT-B2	17.11	13.46	0.302	19.83	1.271
δ_{sf}	0.80	0.87	0.004	0.20	0.028

Table 5.5: Structure function dependence of W acceptance, with statistical uncertainties appropriate for each acceptance term.

this mixing parameter within the range of 55% – 80%, causing < 1% change in the acceptance parameters. The results are listed in table 5.7.

5.2.4.3 Systematics Due to Uncertainty in Standard Model Parameters

The value of the weak mixing angle found at LEP is $sin^2\theta_W = 0.2327 \pm 0.00085$ [52]. When we ran the simulation we used an older value of, 0.2272 ± 0.004[51]. To determine the effect, we recalculate the acceptances using 0.2232 and 0.2336 (the extrema of the two values) for $sin^2\theta_W$. The effects are negligible for A_{ZW} and f, while for A_Z we find $\delta A_Z = 0.20$. The construction of the LO generator required that we adjust M_W when simulating W events instead of $sin^2\theta_W$, so we used the extrema of $M_W = 79.9 \pm 0.4$ GeV/c^2 with the results shown in Table 5.7.

5.2.4.4 Systematics Due to Boson p_t Spectrum

Figure 5.1 shows the nominal W and Z boson p_t spectra which was used for the detector simulation. A parameterization was determined from these distributions [53] having the form

$$\frac{d\sigma}{dp_t} = \frac{2p_t(p_t^2 - D)^{(C-1)}}{B[(Ep_t)^F + 1]}. \tag{5.2}$$

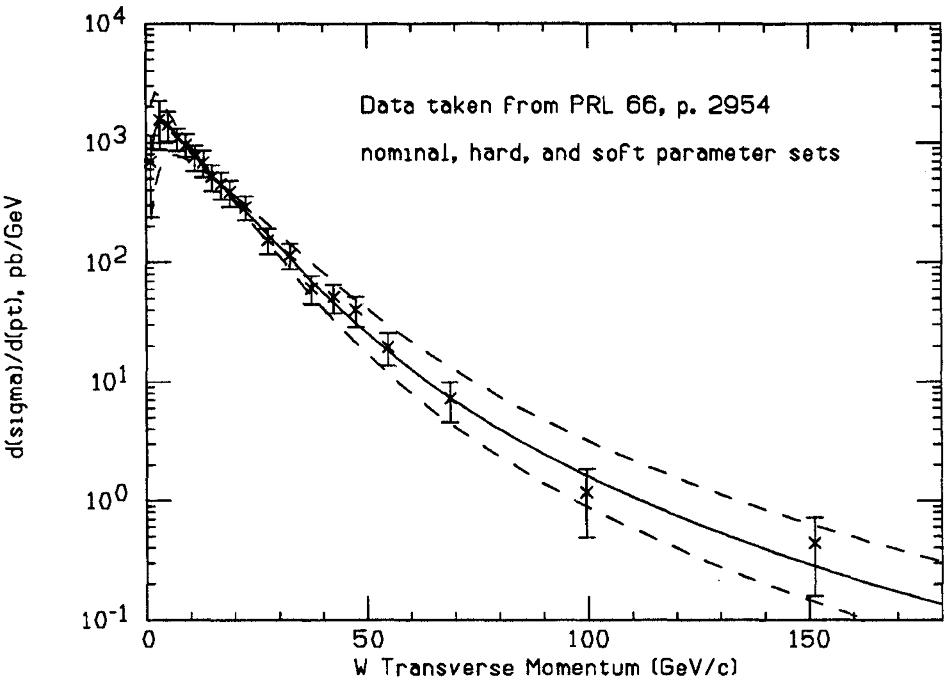

Figure 5.11: The hard and soft W p_t spectra parameterization superimposed on the nominal parameterization and the data.

The best-fit values for the W spectrum are B=1.434E-04, C = -0.07, D = -13.8, E = 0.0342, F = 3.09.

To determine the effect uncertainties in this spectrum would have on the final acceptance result, we found two sets of parameters that give an eyeball-fit to the hardest and softest distributions compatible with the data. The three distributions are shown in Figure 5.11 and have the following parameter sets.

- HARD parameter values: B = 1.3E-04, C = -0.07, D = -50.0, E = 0.03, F = 2.90
- SOFT parameter values: B = 1.4340E-04, C = -0.07, D = -5.0, E = 0.038, F = 3.30

The systematic uncertainty on the acceptance is found by using the different p_t spectra in the simulation and noting the changes in the resulting acceptances.

Acceptance term	Soft p_t spectrum	Hard p_t spectrum	$\delta_{p_t} = \frac{1}{2}\cdot$ range
W acceptance (A_W)	0.1884	0.1859	0.0013
Z acceptance			
A_Z	0.1508	0.1544	0.0018
f	0.308	0.304	0.002
'One-legged Zs' (A_{ZW})	0.1992	0.1940	0.0026

Table 5.6: The dependence of the acceptances on the boson p_t spectrum, and the resulting systematic uncertainties.

Table 5.6 shows the results. The systematic uncertainty is taken as half of the range between the acceptances found using the high-p_t and the low-p_t spectra.

Figure 5.12 shows the boson p_t dependence of the Z acceptance terms. As p_t^Z increases, we observe a decrease in the lab angle of the daughter muons, and when the angle is a multiple of 15° (the angle subtended by one wedge) then $A_{m\cdot m}$ hits a local maximum and $A_{m\cdot t}$ is at a minimum. This is an expected result, and increases confidence in the simulation.

5.2.4.5 Systematics Due to Modeling of the Detector Resolution

The unseen leg of the one-legged background Z's deposits energy in the calorimeter, shifting $\not{E}_t$ to lower values. The Monte Carlo inserts a constant calorimeter deposition along the unseen Z leg. The contribution in the transverse direction is reduced by $\sin\theta$, where θ is the polar angle of the calorimeter tower from the beamline. Figure 5.13 shows the change in A_{ZW} for different values of this fixed energy deposition, from 0 to 25 GeV. In reality the amount of energy deposited obeys a Landau distribution but in practice the bias is small enough that using a constant value gives a good approximation. We use a value of 3 GeV, which reduces the one-legged Z background to 131 events, compared to 134 events calculated without the effect.

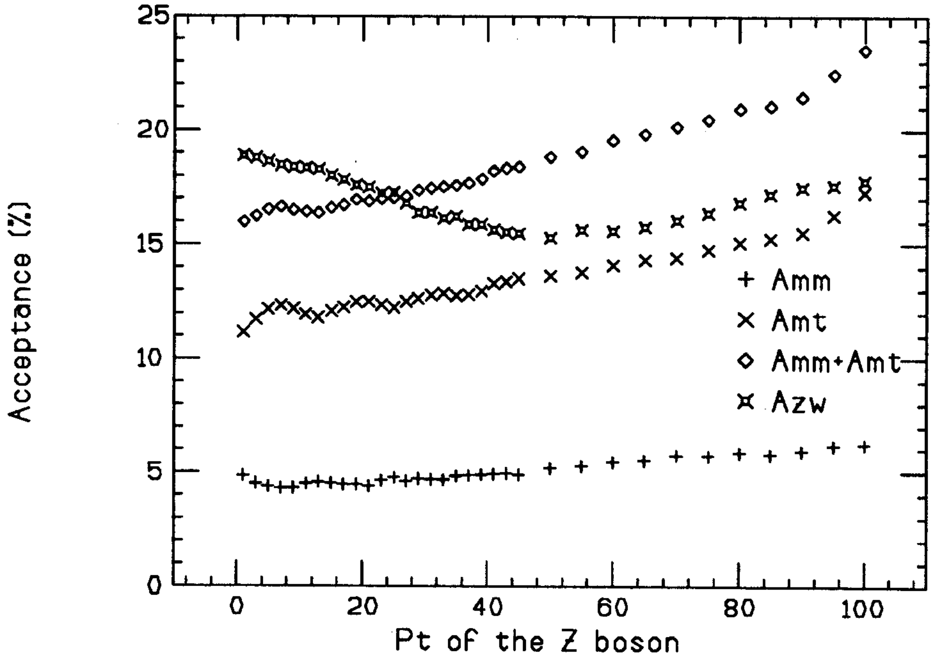

Figure 5.12: The acceptance of the Z event classes as the Z boson p_t is increased.

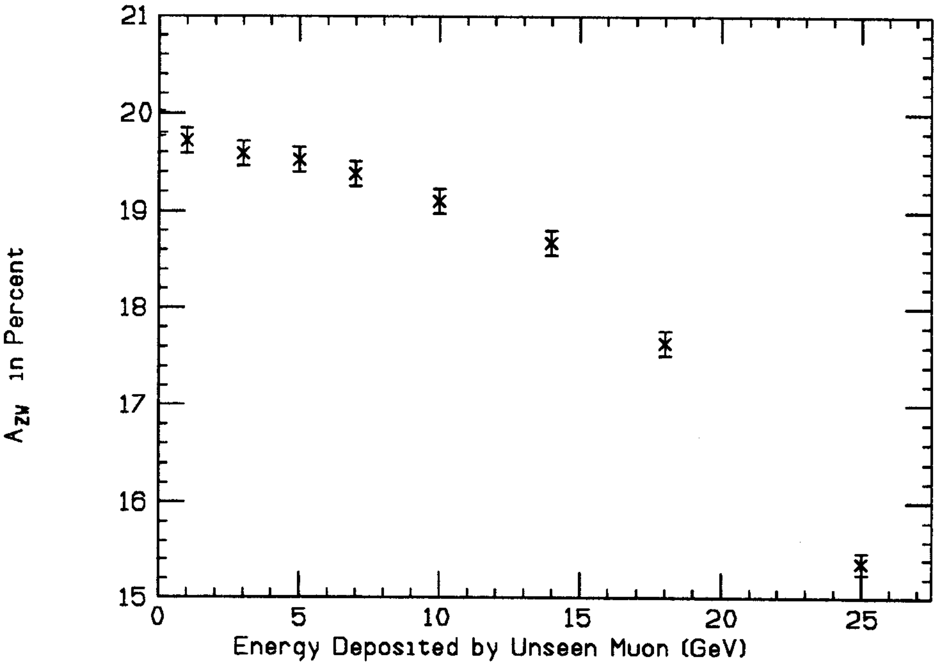

Figure 5.13: A plot of the "false W" acceptances versus the fixed amount of simulated calorimeter deposition caused by the muon. A fixed value of 3 GeV was used for the fast simulation.

5.2.4.6 Systematics Due to Modeling of $\not{E}_t$ Resolution in 2 Jet Events

The simple method used to model the jet recoiling against the W in the LO simulation raised concerns on its accuracy for acceptance determination, since we modeled a single jet opposite to the W in ϕ and a small portion of the real events have more than one jet. If the acceptance of two jet events was substantially different from that of the single jet events, our failure to take this into consideration would result in unrealistic acceptances.

To test this we changed our single jet model to produce two jets, 45 degrees on either side of being back-to-back with the W so that the vector sum of the transverse momentum of these jets exactly balances the W p_t. We smear each jet as we previously did the single jet and measure the resulting acceptance. To be conservative we made the jet smearing perfectly correlated, using the same smearing for both to magnify any effect this might have.

To properly model the two jet events we looked at the data and required two jets with $E_t^{jet} > 10$ GeV, keeping 92 events. We took the p_t spectrum for the W's in these events and used it as the input to the modified simulation.

The acceptance obtained from this two-jet model was $18.36 \pm 0.12\%$, while the old single jet method gave $18.45 \pm 0.12\%$, the difference being within the statistical uncertainty. Even if we ignore the statistical uncertainty, the two-jet events account for only 6.6% of the events, thereby causing a difference of only $(18.45 - 18.36) * 0.066 = 0.006\%$. We conclude from this that our model does not cause a bias in the acceptance calculations.

5.2.4.7 Systematic Uncertainty due to the ΣE_t Spectrum

The simulation uses a ΣE_t distribution taken from data for modeling the neutrino p_t calculation. Since the real interest in this spectrum lies only in it's interaction with the jet opposing the boson, we focus on this interaction. As described above, we obtain the ΣE_t spectrum by using a raw spectrum from electron and muon events and subtracting a degraded value of E_t^{jet}; using a constant degradation factor of 1.75. For an estimate of this systematic uncertainty this degradation function is treated as a constant and varied from 1.0 to 2.0. As seen in Table 5.7, the model is very insensitive to this parameter.

5.2.4.8 Systematic Uncertainty due to the Jet Degradation Function

The jet degradation function has three parameters with associated uncertainties. To estimate the systematic uncertainty this imposes on the acceptance, the simulation was run for W and Z events while each parameter was individually placed at an extremum. All permutations were modeled and the resulting eight values for each acceptance parameter were fitted to a gaussian to determine the uncertainty, with the result shown in Table 5.7.

5.2.4.9 Systematic Uncertainty due to the Calorimeter E_t Resolution

The systematic uncertainty caused by the resolution of the calorimeter E_t measurement was found in much the same way as the Jet Degradation Function uncertainty. There were two parameters to the linear function defining this resolution, and they were set to each permutation, with the resulting values fitted to a gaussian. The results are in Table 5.7.

	A_W	A_Z	f	A_{ZW}
Systematic uncertainties				
Higher-order correction	0.02	0.05	0.002	0.05
Structure functions	0.80	0.85	0.004	0.20
Event ΣE_t	0.05	–	–	0.02
Boson P_t	0.13	0.18	0.002	0.26
$sin^2\theta_W$ $(* \Rightarrow M_W)$	0.07*	0.20	0.001	0.02
Underlying event model	0.21	–	–	0.35
Total	0.84	0.89	0.004	0.48
Statistical Uncertainty	0.06	0.05	0.002	0.06
Total Uncertainty	0.84	0.89	0.005	0.48
Final Corrected Acceptances	18.96%	15.40%	0.310	19.97%

Table 5.7: Summary of acceptance results. Units for uncertainties are the same as for the acceptance on the bottom line. The total systematic uncertainty includes only those effects that are larger than the statistical uncertainty from the monte carlo. The '*' indicates that the Monte Carlo W generator did not allow adjustment of $\sin^2\theta_W$, but only allowed adjustment of the W mass.

Chapter 6

Efficiencies

Each of the muon selection criteria has an associated risk that real muons will be rejected. While loose cuts decrease the number of muons rejected, loose selection criteria increase the backgrounds. To study these efficiencies a sample of muons is required that, while uncorrelated with the data sample, still resembles the general morphology of events in the data. Cosmic rays, direct production J/ψ events, and in some cases the second muons of Z events were useful for these studies.

These samples were complementary. While muons from J/ψ events were mainly at low p_t, those from the second muon in Z events covered the higher momentum range. Cosmics covered the whole range of p_t and were also useful in extending the η range of these studies; this was possible with the knowledge that we are almost guaranteed to be looking at muons.

6.1 Minimum Ionization Efficiency

There are three methods available to measure the efficiency of the muon calorimeter tower energy cut [54], but they use data samples of relatively few events, yielding low statistics and associated high statistical uncertainties. All three methods are discussed, as well as a Monte Carlo method used as a cross-check of the results.

6.1.1 Using the Second Muon from Z Events

Since a calorimeter energy signature consistent with a minimum ionizing particle ($E_{em} \leq 2$ GeV, $E_{had} \leq 6$ GeV) was required to identify a golden muon, we cannot use these muons to study the efficiency of the requirement. The second muon of Z events may be exploited, however, since no energy requirement was made for them. The selection requirements imposed to get a sample of Z's for this study are similar, but not identical, to the cuts made to obtain the data sample. The difference is that for this study the cuts were not as stringent on the second muon. The requirements that the second muon had to pass for this efficiency study are:

(a) $p_t \geq 20$ GeV/c;

(b) not a cosmic ray;

(c) $|z_{vtx}| \leq 60$ cm;

(d) $|\eta$ of track exit from CTC$| \leq 1.1$;

(e) $ISO \leq 0.2$;

(f) Charge opposite to that of the first muon;

(g) $75 \leq M_{\mu\mu} \leq 105$ GeV/c^2 (near the Z mass);

(h) $|z_{\mu^1} - z_{\mu^2}| \leq 6$ cm (tracks from the same vertex).

Note that requirements d-h are different from those used to generate the Z data sample for the cross section measurement. These requirements are only used for this efficiency study.

Using these requirements on the second leg of Z events, we find 46 events where both muons traverse the CMU. Of these events, 30 have 2 legs that would each pass the golden muon cuts. Since the muons in these events are interchangeable, both can be used as the second muon for this study, yielding a total of 76 CMU muon legs. The calorimeter requirements were satisfied by 73 of these muons, for an efficiency of $96.0^{+2.2}_{-3.7}$.

There were also 71 events where one muon was golden and the other high-p_t track satisfied the loose cuts. Out of the 71 tracks, 67 pass the calorimeter cuts; yielding an efficiency of $94.4^{+2.7}_{-4.3}\%$. The combined result from Z events is $\varepsilon_{m.i.} = 95.2^{+1.8}_{-2.5}\%$.

6.1.2 Using Muons from J/ψ events

A second method of studying this efficiency uses J/ψ events. The J/ψ data has two types of events, those produced by B decays and direct production events. The direct production events should be similar to Z events, and therefore useful for this study. In order to select J/ψ events similar to Z events we require one muon which satisfies:

(a) $|z_{vtx}| \leq 60$ cm;

(b) Track extrapolates to a good CMU fiducial region;

(c) Track-to-muon-stub match $|\Delta x| \leq 10.0$ cm;

(d) ${E_t}^{0.4} - {E_t}^{tower} \leq 5.0$ Gev (see below);

and a second muon satisfying:

(a) requirements a-c of the first muon;

(b) Charge opposite to that of the first muon;

(c) 3.0 GeV $\leq M_{\mu\mu} \leq$ 3.2 GeV (near the J/ψ peak).

In the W/Z data sample, an isolation cut

$$ISO = \frac{E_t{}^{0.4} - E_t{}^{\mu}}{p_t{}^{\mu}} \leq 0.1 \tag{6.1}$$

was imposed on the golden muons, where $E_t{}^{0.4}$ is the transverse energy in a cone with radius 0.4 (in $\eta\phi$), $E_t{}^{\mu}$ is the transverse energy in the calorimeter tower traversed by the muon, and $p_t{}^{\mu}$ is the transverse momentum of the muon track. Since this cut would be meaningless at the p_t of the J/ψ muons, we take only the numerator and scale the limit accordingly. For Z's the upper limit on the muon p_t is approximately 40-50 GeV, so we scale the upper limit on the numerator to be approximately 50.0 × 0.1 or 5.0 GeV. We keep the $|\Delta x| \leq 10$ cm instead of the value used for W/Z events because the lower p_t of the J/ψ muons causes an increase in multiple scattering.

We find 1448 J/ψ events pass the above cuts, yielding 2896 muons. Of these, only 37 muons fail the combined requirements of $E_{em} \leq 2.0$ GeV and $E_{had} \leq 6.0$ GeV, yielding an efficiency of $\varepsilon_{m.i.} = 98.7^{+0.23}_{-0.26}\%$. Increasing the energy cut discussed above from 5.0 GeV to 7.0 GeV lowers the efficiency to $98.6^{+0.20}_{-0.24}\%$, while lowering it to 3.0 GeV increases the efficiency to $98.9^{+0.21}_{-0.23}\%$. These are also summarized in Table 6.1.

6.1.3 Using Cosmic Rays

A third method of studying the efficiency of the minimum ionizing calorimeter requirement uses cosmic rays with $p_t > 20$ GeV/c. One concern about using a cosmic ray sample for this measurement is that for the top half of the detector the cosmics were traversing the calorimeter in the opposite direction than a muon from a $p\bar{p}$ event. To differentiate these cosmics from those

Method	Efficiency(%)
Z second leg	
CMU Muon	$96.0^{+2.2}_{-3.7}$
High-p_t track	$94.4^{+2.7}_{-4.3}$
J/ψ second leg	
ISO $\sim$ 3 GeV	$98.9^{+0.21}_{-0.23}$
ISO $\sim$ 5 GeV	$98.7^{+0.23}_{-0.26}$
ISO $\sim$ 7 GeV	$98.6^{+0.20}_{-0.24}$
Cosmics	$98.65^{+0.19}_{-0.25}$
Monte Carlo	98.3 ± 0.2

Table 6.1: Summary of the Minimum Ionization efficiencies.

which were moving in the nominal direction through the calorimeter, we examine the cosmic ray sample in two ways; first by looking at all of the cosmic ray data, and then by looking only at cosmics with $\pi \leq \phi < 2\pi$, where the cosmic is traversing the calorimeter in the nominal direction. No difference is expected since the integration time for the calorimeter is long.

Using all of the cosmics (no ϕ cuts) we obtain an efficiency of $\varepsilon_{m.i.} = 98.6^{+0.19}_{-0.25}\%$, while for tracks between π and 2π it was $\varepsilon_{m.i.} = 98.61\%$. As expected the direction of the muon through the calorimeter has no discernable effect.

6.1.4 Using a Monte Carlo Simulation

As a cross-check we use the full CDF detector simulation [55] to model the energy deposition for 25 GeV muons, matching the cosmic ray sample. We use the full detector simulation instead of the the fast simulation because it contains a calorimeter model. We also generate 50 GeV muons to determine if the higher p_t muons from $W(Z)$ decays might have a different energy deposition than the lower p_t muons. We see no difference in energy deposition in this simple Monte Carlo test. We find $\varepsilon_{m.i.} = 98.3 \pm 0.2\%$ where the uncertainty comes from the Monte Carlo statistics and also from the effect of cracks in the calorimeter. This result agrees with

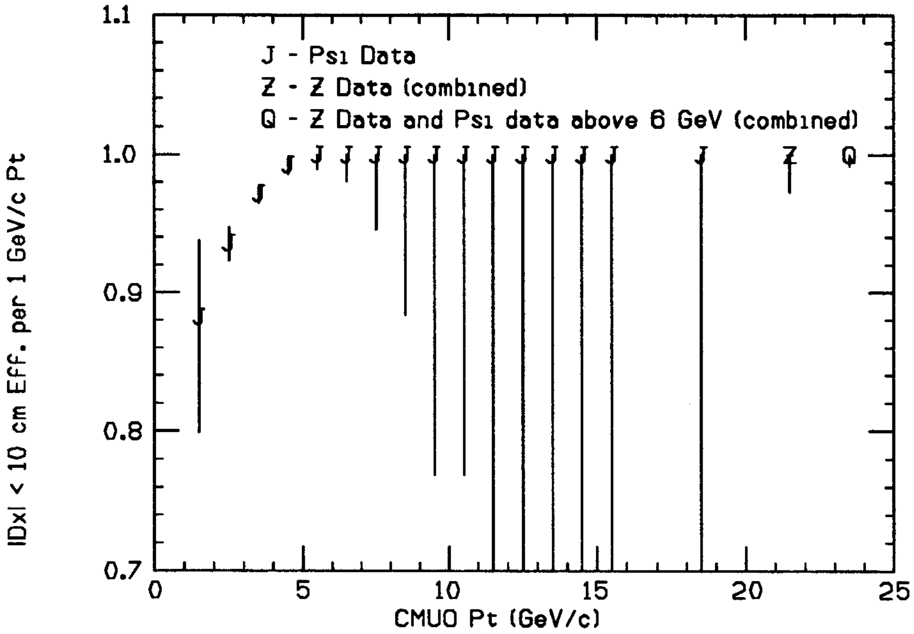

Figure 6.1: The $|\Delta x| \leq 10$ cm cut efficiency for J/ψ events as a function of muon p_t. The efficiency for the second muons from Z's, and that of a combined result, are included. The combined result $\varepsilon_{m.i.} = 100.0^{+0.0}_{-0.8}\%$.

the cosmic ray and the J/ψ values. We shall use the previous results after slightly expanding the uncertainties to include the Monte Carlo result, yielding $\varepsilon_{m.i.} = 98.7^{+0.3}_{-0.4}\%$.

6.2 Δx Matching Cut Efficiency

There were three data samples available to study the efficiency of the Δx matching cut; The W and Z samples, and a J/ψ sample [54, 56]. All of the samples required at least one Central Muon Object (CMUO) with $|\Delta x| \leq 10$ cm so a combined technique was required. The CMUOs in the W and Z samples were used to find the efficiency of the $|\Delta x| \leq 2$ cm requirement of our data sample relative to the $|\Delta x| \leq 10$ cm cut, while the second muons of the Z and J/ψ samples would find the overall efficiency of the $|\Delta x| \leq 10$ cm cut. The product of these two efficiencies would then be the effective efficiency of the $|\Delta x| \leq 2$ cm cut used in the boson sample.

Cut	# Events	# pass	Eff. (%)	Uncert.(%)
Basic W cuts	1434	1379	96.2	$\pm^{0.51}_{0.58}$
Basic W cuts + $\not{E}_t^{\nu} \geq 30$ GeV	982	944	96.1	$\pm^{0.62}_{0.72}$
Basic W cuts + M_t cut	783	757	96.7	$\pm^{0.64}_{0.77}$
Basic W cuts $+E_t^{jet} < 10$ GeV	1041	999	96.0	$\pm^{0.61}_{0.71}$
Basic W cuts $+E_t^{jet} < 10$ GeV + $\not{E}_t^{\nu}$	703	673	95.7	$\pm^{0.76}_{0.91}$
Basic W cuts $+E_t^{jet} < 10$ GeV + $\not{E}_t^{\nu}$ + M_t	568	546	96.1	$\pm^{0.81}_{0.99}$

Table 6.2: Summary of $|\Delta x| \leq 2$ cm results from W data.

Since no Δx cut had been made on the second legs of the muon-muon Z events they could be used to study the $|\Delta x| \leq 10$ cm requirement. All 70 legs from the 35 muon-muon Z events were within 10 cm, so with these low statistics the efficiency of the cut is 100%. The efficiency of the 10 cm cut versus the p_t of the muon is shown in Figure 6.1. The efficiency of the cut above $p_t = 6$ GeV/c is $\varepsilon_{\Delta x} = 100.0^{+0.0}_{-0.8}$, found by combining J/$\psi$'s and Z second legs.

In a separate study a loose W sample was created using the standard W criteria except for the Δx requirement. Out of 1434 events, 1379 muons pass the $|\Delta x| \leq 2$ cm cut for a 96.1% efficiency. Since the sample probably contained some backgrounds, several sets of tighter cuts were imposed to try to further refine the measurement. These tighter cuts included a higher Missing Transverse Energy threshold of $\not{E}_t \geq 30$ GeV, rejecting events containing jets with $E_t \geq 10$ GeV and limiting the W transverse mass to the range 65 GeV $\leq M_t \leq$ 95 GeV. The results are shown in Table 6.2.

Combining the J/ψ and Z results with the W results, we find a combined efficiency of the $|\Delta x| \leq 2$ cm of $\varepsilon_{\Delta x} = 96.0 \pm 1.0\%$.

6.3 Isolation Efficiency

If a W event had significant calorimeter energy deposition which was unrelated to the muon but occupied the same section of the calorimeter, this might cause a valid W event to be rejected. To measure this efficiency we must determine the probability that this type of energy deposition would appear in the detector. The method used is one of *throwing cones*, which consists of measuring the calorimeter energy within a cone projected from the origin to various locations of the calorimeter, said cone having a radius of 0.4 in $\eta\phi$-coordinates where it impacts the calorimeter. The basic procedure for throwing the cones is as follows:

1) throw 7 cones at the same η as the W muon, but at $\phi = \phi_\mu + (2\pi/7) * i$, where $1 \leq i \leq 7$;

2) discard any cone overlapping the cone containing the muon;

3) discard any cone within R=0.4 of back-to-back in ϕ with the W p_t.

For a cone we define

$$ISO = \sum_{0.4} \frac{(E_t - E_t^c)}{p_t^\mu}, \tag{6.2}$$

where E_t^c is the transverse energy in the tower at the center of the cone; yielding the ISO distribution shown in Figure 6.2. In order to determine the systematic uncertainty, the selection requirements and the method were slightly varied. The results of these studies are shown in Table 6.3.

The higher Z mass compared to the W mass will give a slightly elevated μ p_t spectrum for the Zs. Since the calorimeter energy deposit for muons is independent to the muon p_t, equation 6.2 may give W events a smaller ISO parameter then that for Zs, leading to different efficiencies. We check this possibility by using the calorimeter signal from W muons with the

Procedure	Result
Standard	6862/7017 = 0.978
Standard, veto jets with $E_t^{jet} > 10$ GeV.	5002/5060 = 0.989
Standard, but assign random $\|\eta\| < 0.8$ to cone	7596/7781 = 0.976
Standard, but require cone to be in CMU fiducial region	5295/5420 = 0.977
Standard, but require muon tower in cone to pass E_{em}, E_{had} cuts	6856/7009 = 0.978
Standard, but allow cone to overlap jet	8045/8282 = 0.971
Standard, but require $p_t^\mu > 30$, $\not\!\!E_t > 30$	4121/4202 = 0.981
Standard, but require $p_t^\mu > 35$, $\not\!\!E_t > 35$	2419/2457 = 0.985
from clean W's (defined in text)	600/612 = 0.980
from clean W's, drop $\|z_0 - z_{vtx}\|$ and Δx_{slope} cuts,– loosen Δx cut to 2 cm	777/792 = 0.981
from clean W's, tighten p_t^μ, $\not\!\!E_t^\nu$ cuts to 35 GeV	383/386 = 0.992
Same as above 3, but reject events with $E_t^{jet} > 10$ GeV	440/441 = 0.998
	569/572 = 0.995
	288/288 = 1.000
Convolute E_{cone} spectrum from W's with Z p_t spectrum	0.986
Ditto, but reject events with $E_t^{jet} > 10$ GeV	0.996
Final (ε_{iso})	0.98 ± 0.01

Table 6.3: Summary of the isolation efficiency study, with the resulting ε_{ISO} for different W cuts.

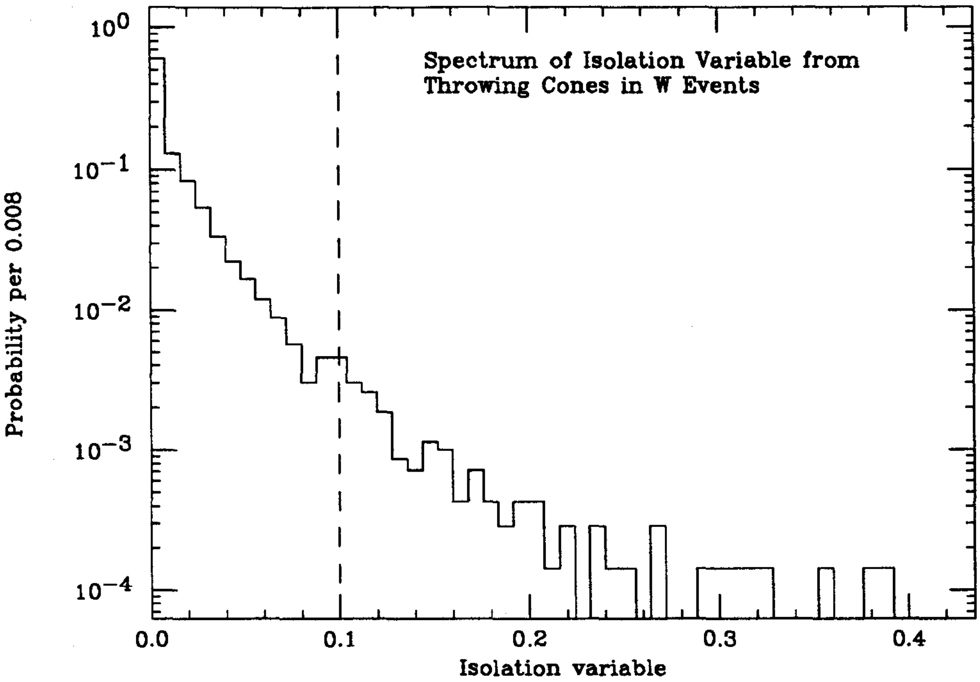

Figure 6.2: The *ISO* distribution obtained by throwing cones in W events. The dashed line shows the maximum value of *ISO* allowed for a golden muon in the data sample.

p_t spectrum from Z muons to recalculate the *ISO* efficiency. Table 6.3 lists the results, which lead us to conclude that it is not a problem.

Another check on the *ISO* efficiency uses a sample of very clean W events, taken without the *ISO* cut imposed but with other cuts tightened. The cuts for these Ws are different from the cuts we use for the W data sample in the following ways:

- $p_t > 30$ GeV/c, $\not{E}_t^\nu > 30$ GeV;
- track has impact parameter relative to the beam axis < 0.05 cm;
- $|\Delta x| < 1$ cm, $|z_{trk} - z_{vtx}| < 2.5$ cm, $|\Delta x_{slope}| < 20$ mrad;

For this sample, Δx_{slope} refers to the difference of the slope of the muon stub in the chambers to that of the extrapolated track. A Δx_{slope} that is too high may result from either pairing up a stub with the wrong track, or from muon bremsstrahlung, or from mis-measured jet punchthrough. Again, the results are summarized in Table 6.3.

6.4 CTC Track Reconstruction Efficiency

Although the tracking efficiency for event reconstruction is very good, it is not perfect. When we retracked the sample using a somewhat different reconstruction method, it is possible for more tracks to be lost. We note that the efficiency for the original tracking was flat over the central acceptance region [57, 58, 59]. The acceptance studies for this analysis indicate that the inefficiency is small for the central region, as seen in the $|\eta| \leq 1.0$ region of figure 5.9. We examine a sample of $Z^0 \rightarrow e^+e^-$ events which were reconstructed using the original tracking method. This sample had no track requirement on the second electron, identifying it instead by the calorimeter signal only. We then find the number of these electrons that had tracks associated with them. The resulting efficiency is binned by the detector eta where the electron left the CTC, and plotted in figure 4.8. We note that in the central region of interest the efficiency remains flat.

We then consider the effect of retracking. By retracking the same $Z^0 \rightarrow e^+e^-$ sample mentioned above, we find that 3 of the 237 electrons in the sample with tracks lost them in the retracking process, giving $\varepsilon_{trk} = 0.987 \pm 0.01\%$.

6.5 CMU Muon Reconstruction Efficiency

Some muons which are projected to impact the CMU near the edge of the fiducial region may be deflected to fall outside this region due to multiple scattering. This combined with inefficiencies of muon stub reconstruction is included into the CMU efficiency, called ε_{CMU}.

We use the second muon of Z events to study ε_{CMU}. There were 35 events where both tracks project to the CMU. Of the 70 muons involved, 69 passed the 'silver' cuts and only one failed to make a good CMUO, due to failing the track-stub matching requirement. The result is $\varepsilon_{CMU} = 98.6^{+1.2}_{-3.3}\%$.

We check this result with a sample of cosmic rays. These cosmics were recorded in a special run to study the muon trigger efficiencies by using a simple CDT-CTC coincidence trigger. Out of the 2056 cosmic ray events collected, we found that 70 of the tracks extrapolated to the active region of the CMU left no muon stub; yielding an efficiency of $\varepsilon_{CMU} = 0.966 \pm 0.004\%$. This result is statistically consistent with the previous result. We shall use the $p\bar{p}$ result because of unanswered questions of the impact of the nonstandard timing of the cosmic ray events in relation to the data acquisition systems clock.

6.6 Trigger Efficiencies

There are three levels of the Central Muon Trigger system. The basic function of these is described in section 3.3.

The Level 1 Muon trigger efficiency was studied using $p\bar{p}$ and cosmic ray events [60]. Briefly, we needed to insure that we were studying muons and that the sample was not biased by use of the L1 Muon trigger itself. For $p\bar{p}$ events we require that the event fire at least two non-muon triggers, and require $E_{em} < 0.7$ GeV, $E_{had} < 3.1$ GeV and $|\Delta x| \leq 10$ cm. Since the trigger threshold was changed during the run from 5 GeV to 3 GeV, we study the efficiencies of the two thresholds separately. Examining the triggers for each event, we determine the trigger efficiency by

$$\varepsilon_T^{L1} = \frac{\#\text{ with L1 }\mu\text{ trigger}}{\text{Total }\#\text{ of events}}. \tag{6.3}$$

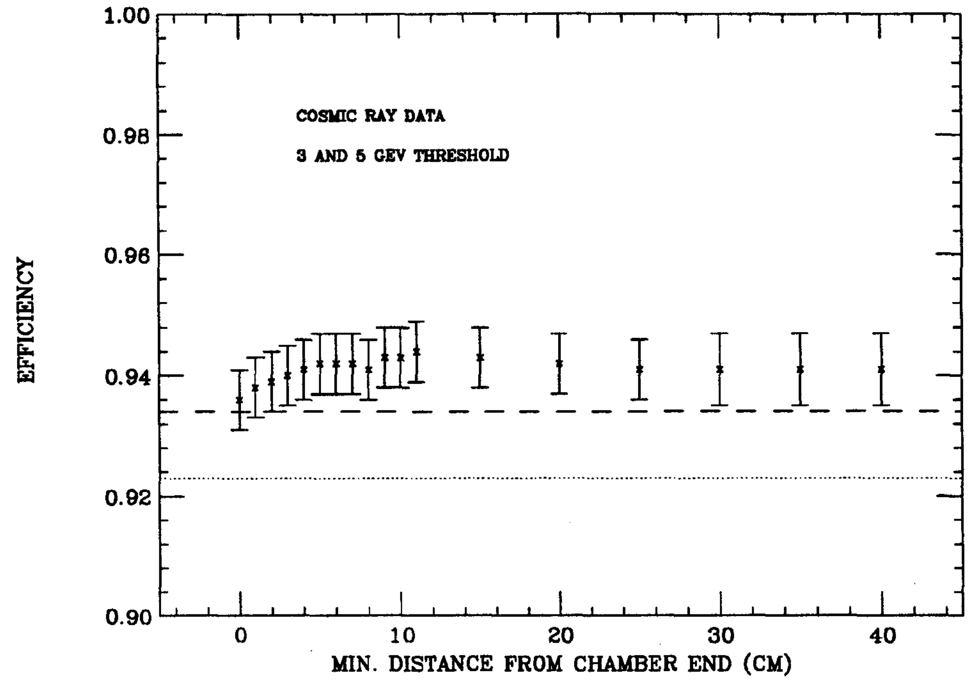

Figure 6.3: The L1 Muon trigger efficiency versus a minimum distance requirement from the end of the chambers. The dotted line is the Level 1 trigger efficiency from [60], and the dashed line is the nominal L1 trigger efficiency used for this analysis, as explained in the text.

The sample of cosmic rays described in the previous section serve as a cross check. Since we are sure to have muons, no calorimeter isolation requirements are necessary. Using the same technique of examining the event trigger as above, and binning by muon p_t, we obtain Figure 3.11. Another factor must be considered, however, before a final L1 trigger efficiency is obtained.

The Level 1 Muon trigger efficiency falls off near the ends of the chambers due to multiple scattering, as seen in in figure 6.3. If muons are required to be a few cm away from the ends of the chambers, the Level 1 trigger efficiency increases by about 0.5%. The fiducial cuts which we applied to the W and Z samples restrict the muons to the high-efficiency zone, hence we re-evaluated the L1 trigger efficiency. The Level 1 efficiency for fiducial muons with $p_t \geq 15$ GeV/c is $\varepsilon_T^{L1} = 93.4 \pm 0.5\%$.

Note that the efficiency plateau of Figure 6.3 seems to be over 94%. This is higher than the value in [60]. This is caused by events with ADC overflows; to plot the z position of the muon stub we had to reject events which exhibited overflows. The overflows are caused by processes such as a bremsstrahlung shower or by a jet punching through the calorimeters to the CMU. This is not a large problem in electroweak boson events because Ws and Zs are fairly isolated, but it may have a small effect on our trigger rates. Considering this we assign an additional systematic uncertainty of ±0.5% to the trigger efficiency.

The Level 2 Muon trigger matches a CFT track with a CMU stub within a 15 degree window. Although the L2 trigger doesn't explicitly require a L1 trigger, the CMU stub will not be located without the L1 trigger firing, so we must include the effect that the L1 efficiency will have on the L2 efficiency. Since the CFT depends on the timing of the event we used $p\bar{p}$ data for this study [61]; cosmics have uncertain timing information.

The study required that the event have a trigger other than a CFT or Level 2 muon trigger, and we also required $E_{em} < 0.7$ GeV, $E_{had} < 3.1$ GeV, $|\Delta x| \leq 10$ cm, and that the total sum of E_t in the calorimeter towers neighboring the muon tower satisfy $\sum E_t < 10$ GeV for background rejection. A L1 muon trigger was also required. By compensating for the L1 trigger effect in this way the data no longer had to be separated into two samples (of 3 and 5 GeV thresholds). Figure 6.4 shows the final efficiencies versus track p_t. For the region of interest for this analysis, $p_t > 15$ GeV/c, an efficiency of $\varepsilon_T^{L2} = 97.2\%$ was obtained.

We can check the combined L1*L2 trigger efficiency by looking at Zs where both muons impact the CMU. Recall that we required a L2 muon trigger for the event as a whole but we did not specify that the trigger had to come from a particular muon. We can thus examine the 70 CMUOs resulting from the 35 Z events where both muons impact the chambers. By looking at a

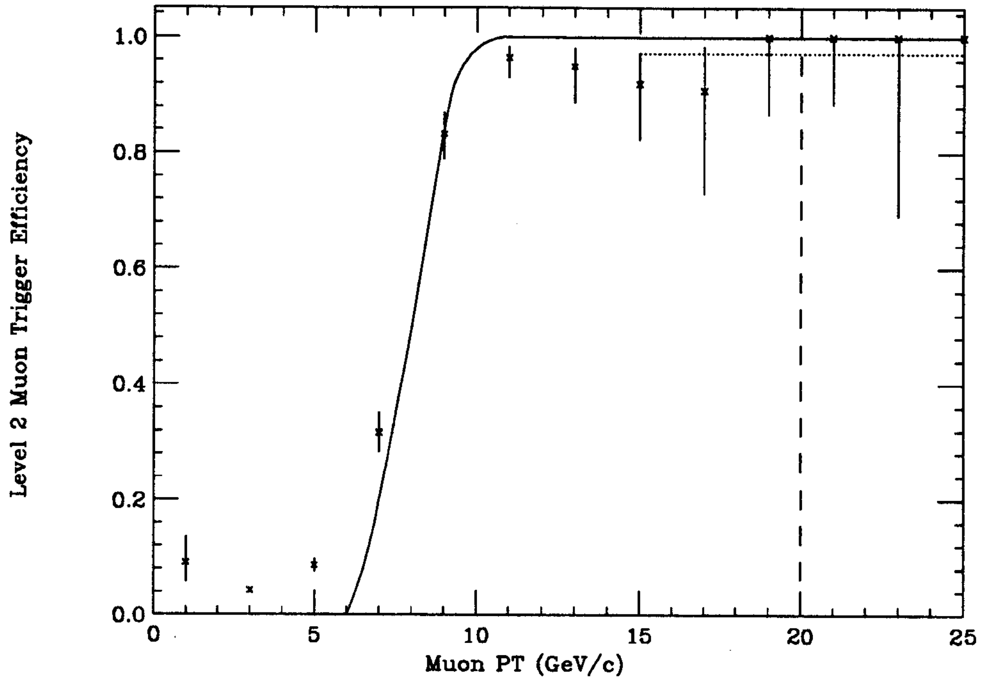

Figure 6.4: The efficiency of the Level 2 Muon trigger versus muon p_t. The curve is a theoretical calculation showing the effect of multpile scattering assuming a 100% trigger efficiency. The dotted line is the average efficiency (97.2%) for muons with $p_t \geq 15$ GeV/c, while the dashed line represents the minimum muon p_t we accept in the data sample.

CMUO that fired the muon triggers, we examine how many times the 'other' muon also fired the L1 and L2 muon triggers, giving an efficiency of $\varepsilon_T^{L1*L2} = 64/70 = 91.4^{+3.4}_{-4.8}\%$. When we require that the 'other' muon be in the CMU fiducial region, we get $\varepsilon_T^{L1*L2} = 59/64 = 92.2^{+3.3}_{-4.9}\%$. Both of these results confirm the L1*L2 efficiency result of 91 ± 3% reported in table 6.4.

The Level 3 Muon trigger requires a track found by a fast online tracking routine of at least $p_t \geq 11$ GeV/c to match the location of the CMU stub within 10 cm. A brief check of this efficiency is accomplished by using the 65 events from the L2 trigger study with $p_t > 15$ GeV/c [62]. We find that all of the muons have a L3 trigger, giving $\varepsilon_T^{L3} = 100.0^{+0.0}_{-2.8}\%$. We combine the trigger efficiencies as seen in Table 6.4 to get an overall trigger efficiency of $T = 90.8 \pm 2.7\%$.

6.7 Cosmic Filtering

We discussed the removal of cosmic rays from the data sample in section 4.4.3. The efficiency of the filter was estimated by applying it to a specially prepared sample of high-p_t muon events from the 1988-1989 data-taking run [38]. Out of 4521 events in the sample, the filter rejected 129 μ candidates as coming from cosmic rays, leaving 4392 events. These events were hand-scanned, and we concluded that 4 of them were falsely identified as cosmic rays. Furthermore, three events were identified as cosmic rays by the filter but we were unable to conclusively identify them as such, as they were borderline cases. Assuming that they were actually real $p\bar{p}$ events will give us a worse case for the efficiency of the filter. The conclusion is that the cosmic filter is better than

$$\frac{4392}{4392+7} = 99.8 \pm 0.1\%$$

efficient for W/Z events.

6.8 Combining the Efficiencies

If the muon parameters we used for event selection are correlated, the product of the single efficiencies is less than it should be. We measured the E_{em} and E_{had} efficiencies as one cut so any correlations were already included in the measurement [54]. The fact that the cosmic ray results agree with the $p\bar{p}$ results for the E_{em} and E_{had} studies shows that isolation has a small effect on the calorimeter efficiency, thus these parameters are uncorrelated. When the Δx cut was studied, all of the other cuts including the muon trigger requirement had already been imposed on the data sample, so any correlation between Δx and any other cut has already been taken into account. The only other efficiency left that may have a correlation with other

Cut Type	Measured Efficiency
Track-stub matching, $\lvert\Delta x\rvert \leq 2$ cm	$\varepsilon_{\Delta x} = 96.0 \pm 1.0\%$
Minimum Ionizing (E_{em}, E_{had})	$\varepsilon_{m.i.} = 98.7^{+0.3}_{-0.4}\%$
Isolation, $ISO \leq 0.1$	$\varepsilon_{ISO} = 98.0 \pm 1.0\%$
Track Reconstruction	$\varepsilon_{trk} = 98.7 \pm 1.0\%$
CMU segment finding	$\varepsilon_{CMU} = 98.6^{+1.2}_{-3.3}\%$
Cosmic filter	$\varepsilon_{cos} = 99.8 \pm 0.1\%$
Muon Trigger	
L1: $\varepsilon_T^{L1} = 93.4 \pm 0.5\%$	
L2: $\varepsilon_T^{L2} = 97.2^{+1.5}_{-2.7}\%$	
L3: $\varepsilon_T^{L3} = 100.0^{+0.0}_{-2.8}\%$	
Combined $T = \varepsilon_T^{L1} \cdot \varepsilon_T^{L2} \cdot \varepsilon_T^{L3}$	$T = 90.8 \pm 2.7\%$
Combined fiducial "silver" $\varepsilon_{s1} = \varepsilon_{CMU}\varepsilon_{m.i.}\varepsilon_{trk}$	$\varepsilon_{s1} = 96.0 \pm 3.5\%$
Combined non-fiducial "silver" $\varepsilon_{s2} = \varepsilon_{m.i.}\varepsilon_{trk}$	$\varepsilon_{s2} = 97.4 \pm 1.1\%$
Combined "gold" $\varepsilon_g = \varepsilon_{s2}\varepsilon_{iso}\varepsilon_{\Delta x}\varepsilon_{CMUO}$	$\varepsilon_g = 90.4 \pm 3.8\%$

Table 6.4: Summary of the Selection Efficiencies.

cuts is the muon isolation efficiency. This was studied by throwing cones in W events, for both our standard sample and for a set of clean W's with a tight Δx cut [63]. If Isolation and Δx were correlated the results from these two samples should vary. These methods gave the same result. We conclude that any correlations between the muon parameters is small, and so the total efficiency is just the product of the individual efficiencies, summarized in Table 6.4

Chapter 7

Backgrounds

It is possible for other processes to mimic $W \rightarrow \mu\nu$ or $Z^0 \rightarrow \mu^+\mu^-$ events. In measuring the cross sections by counting events, we are vulnerable to these false boson events. Our golden muon selection criteria eliminates a portion of these background events, but it is naive to assume that this has completely purified our samples. In this section we establish the methods that were used to estimate the backgrounds in the sample.

7.1 Background to W Bosons

Having only one high-p_t muon, there are several other physics processes that will mimic a $W \rightarrow \mu\nu$ decay, several of which are caused directly by detector inefficiencies. For example, a QCD dijet might mimic a W because the jets simulate the muon and neutrino. A $Z^0 \rightarrow \mu^+\mu^-$ event can also mimic a W if the second track is at a high $|\eta|$, and is undetected. In this section, we estimate the contribution of these "false" W's so that we do not include them in the cross section measurement.

7.1.1 $Z^0 \rightarrow \mu^+\mu^-$, with a missing muon

The primary source of backgrounds to the $W \rightarrow \mu\nu$ events are $Z^0 \rightarrow \mu^+\mu^-$ events where one of the muons traverses the CMU and produces a golden muon while the other is undetected. This is usually caused by the second muon being in an η range that is too high for the CTC to reliably reconstruct the track. This missing muon will result in the event having an artificially high $\not{E}_t^\nu$ measurement, causing the event to be identified as a W.

As discussed briefly in section 5.2.1, a simulated Z event that has one unseen muon would continue to be modeled as a W. When the acceptance of the Z's was measured we also measured the acceptance of these events, which we called A_{ZW}. We take the ratio of this acceptance to that of detecting the Z (A_Z), adjust for the difference in efficiencies between Z and W events, and normalize to the number of Z's seen in the data. This is expressed by

$$N_W^{bkg} = \frac{A_{ZW}}{A_Z}\frac{\epsilon_W}{\epsilon_Z} \cdot N_Z^{obs}. \tag{7.1}$$

The fast Monte Carlo detector simulation indicates a background of 131 ± 13(*stat*) ± 8(*syst*) events. A cross check with ISAJET gives a result of 137 ± 10 events, which is in excellent agreement. These simulated events are added to simulated W events in Figure 7.6, and are superimposed with the data.

It is also possible for the second muon in a Z event to fail the associated loose cuts. This will result in $\not{E}_t^\nu$ being artifically high, just as in the above case, and will likely cause the event to be seen as a W. A quick estimate of this background can be calculated for this as $\sum_{i=1}^{2}(1 - \varepsilon_{si}) \cdot N_{Zi}^{obs}$, where N_{Zi}^{obs} is the number of observed Z events of each type ("mm" and "mt"), and ε_{si} is the efficiency of the silver muon for that type of Z. There are 37 muon-muon

Zs, and 69 Zs where only 1 leg is a good CMU muon. The silver efficiency where both legs are good muons is 0.960 ± 0.035, while that where the second leg is only a high-p_t track is 0.974 ± 0.011. Thus, this background is

$$(1 - 0.96) \cdot 37 + (1 - 0.974) \cdot 69 = 3 \pm 3 \text{ events.}$$

Hand-scanning the W sample yields 6 events of this type, where the event failed a single Z cut by a small amount. We use the calculated result for this background.

7.1.2 $W \rightarrow \tau\nu$, $Z^0 \rightarrow \tau\tau$ backgrounds to W

Events where a W or Z decay via the tau channel and the tau subsequently decays to a muon may mimic a direct $W \rightarrow \mu\nu$ event. To estimate the magnitude of this effect, we use ISAJET to generate samples of $W \rightarrow \tau\nu$ and $Z^0 \rightarrow \tau\tau$ events, and to also generate $Z^0 \rightarrow \mu^+\mu^-$ events. We then use the CDFSIM full CDF detector simulation and apply W selection criteria to the tau events, and Z criteria to the muon events. Then, in a manner similar to equation 7.1 we normalize the $Z^0 \rightarrow \mu^+\mu^-$ Monte Carlo to the data, and normalize the tau acceptance to the muons; removing the effect of the assumed cross section in the Monte Carlo generator from the results. We find $A_W^{Z^0 \rightarrow \tau\tau} = 0.424 \pm 0.13$ and $A_W^{W \rightarrow \tau\nu} = 0.73 \pm 0.13$, leading to the results shown in Table 7.2. Figure 7.6 shows the contribution of this type of background to the W's, and compares the simulation to the data.

7.1.3 QCD dijets faking a μ and large $\not{E}_t$

The ~ 2 nb $W \rightarrow \mu\nu$ cross section is dwarfed by that of dijets. Even after requiring $|\eta| < 0.6$ and $E_t > 20$ GeV the dijet cross section is ~ 600 nb, and that of $b\bar{b}$ events is 8.5 ± 4.3 μb for

$p_t^b > 10$ GeV/c. Even with the low probability of the jets appearing as a muon and the opposite jet being mis-measured to generate an artificial $\not{E}_t^\nu$, the QCD background to $W \rightarrow \mu\nu$ is still sizable.

7.1.3.1 DiJet Background in $W \rightarrow \mu\nu$: $ISO-$ $\not{E}_t^\nu$ Method

By looking at the $\not{E}_t^\nu$ spectrum of the W sample (without the $\not{E}_t^\nu$ cut imposed) shown in Figure 7.1 (dashed line) we make several observations. The low $\not{E}_t^\nu$ region has a high amount of background which falls off with increasing $\not{E}_t^\nu$ just as the W events (those with $\not{E}_t^\nu > 20$ GeV or so) begin to dominate. It is obvious that the background continues falling under the W region, and that there are W events under the background region. Ideally, we'd like to continue a fit of the low $\not{E}_t^\nu$ region into the W region as a method of estimating the dijet background to the Ws. Unfortunately, just as the dijets contaminate the Ws, W events are contaminating the dijets so that a fit to the dijet region will not only eliminate dijet events, but will also eliminate real W's.

A background sample of the same shape (without the W's) is needed. Examining the high-p_t muon sample, and requiring a non-isolated muon with $ISO \geq 0.3$ and a jet with $E_t \geq 10$ GeV, we have such a sample. Recall that our expected QCD dijet background to the W sample contains one jet that fluctuated to a muon while the other jet falls upon a crack, or is otherwise poorly measured. This sample will be similar to the expected background except that the second jet is seen. By requiring a jet we are selecting QCD events, and with the non-isolated muon we are rejecting Ws. The $\not{E}_t^\nu$ of this background sample is plotted as the solid line in Figure 7.1.

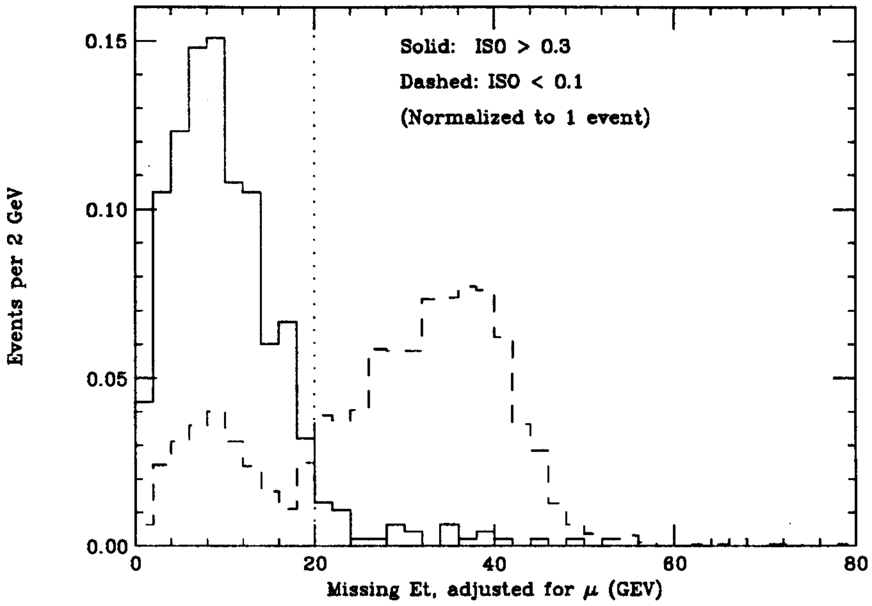

Figure 7.1: The $\not{E}_t^\nu$ of the W data and that of a dijet background sample for use in determining the QCD background to the W. The dotted line represents the minimum $\not{E}_t^\nu$ required for an event to be included in the data sample. The low $\not{E}_t$ peak in the data is from dijet events where one of the jets has fragmented to mimic a muon.

The procedure is then to normalize the low $\not{E}_t^\nu$ region of the $ISO > 0.3$ sample to the same region of the W sample, and thereby determine the number of number of events contained in the high $\not{E}_t^\nu$ region of the normalized $ISO > 0.3$ sample. The results of this process are listed in Table 7.1.

An implicit assumption of this method is that the parameters ISO and $\not{E}_t^\nu$ are uncorrelated in the background sample. If a correlation exists the shape of the $\not{E}_t^\nu$ for the isolated sample may be different from that of the non-isolated sample. We check for this correlation by dividing the sample into regions of $\not{E}_t^\nu$ that are 5 GeV wide. By plotting ISO for the non-isolated sample in four $\not{E}_t^\nu$ bins (figure 7.2) we see the shape change as $\not{E}_t^\nu$ increases. The change is small and we do not believe it is enough to completely invalidate the method, so we shall keep the result and increase the uncertainty to ±20.

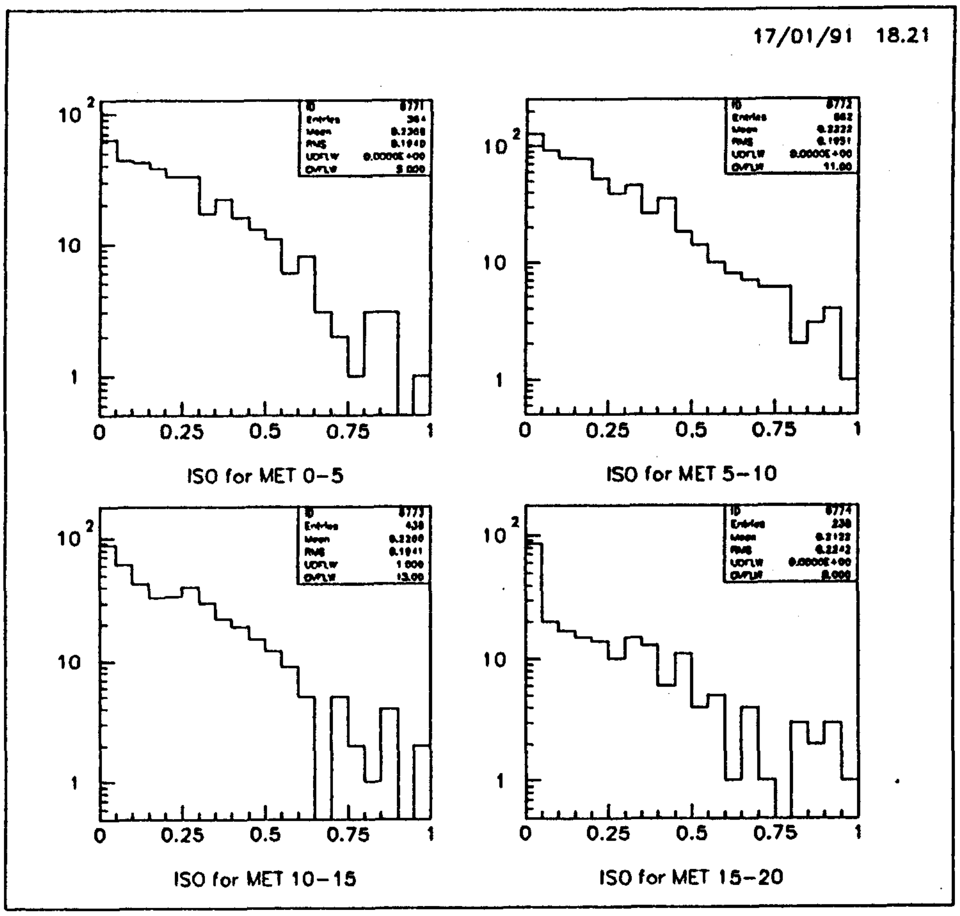

Figure 7.2: ISO distributions for four different $\vec{\not\!\!E}_t^{\nu}$ bins: a) $0 < \not\!\!E_t < 5$ GeV, b) $5 < \not\!\!E_t < 10$ GeV, c) $10 < \not\!\!E_t < 15$ GeV, d) $15 < \not\!\!E_t < 20$ GeV.

	Δx in W sample	
Jet cut on background sample	$\|\Delta x\| < 2$ cm	$\|\Delta x\| < 10$ cm
No jet requirement	20-26 events	29-40 events
≥ 1 jet, $E_t^{jet} \geq 10$ GeV	17-24	29-37
≥ 1 jet, $E_t^{jet} \geq 20$ GeV	7-15	16-24
≥ 2 jets, $E_t^{jet} \geq 10$ GeV	6	11

Table 7.1: QCD background estimate using the $ISO-\not{E}_t^{\nu}$ method for different W sample definitions.

By modifying the muon Δx cut for the background sample we determine if this method is stable. We can also vary the Δx cut on our data sample to determine if it results in the expected increase in background. One such possibility is imposing a requirement on background events to contain a jet with $E_t^{jet} \geq 10$ GeV. This will decrease the size of the background sample, which will decrease the calculated background. Some of the results are summarized in Table 7.1. We note that increasing the cuts on the background sample will make the sample less like the W's and decrease the background estimate. As we did the calculation there were differences between the background and W samples, therefore we expect that we have slightly underestimated the backgrounds. We therefore take the higher end of the range shown in Table 7.1, and inflate the uncertainty to ±20 events, to estimate a QCD background of 30 ± 20 events.

7.1.3.2 Jet-muon angle method

Since the primary assumption of the above method, that the parameters ISO and $\not{E}_t^{\nu}$ be uncorrelated, is not rigorously true we use an independent method to check our results. We use the PAPAGENO Monte Carlo generator to generate $W + 1$ jet and $W + 2$ jet events. The PAPAGENO generator does not generate muon events; it only allows the W to decay via the electron channel. Assuming lepton universality we treat the resulting simulated electron as a muon.

We expect a W QCD background event to consist of two back-to-back jets with one of the jets fluctuating to appear as a muon and the other to be undetected. By plotting $\Delta\phi_{mj}$, the two dimensional opening angle between the "muon" and the leading jet in the background sample described above, we see this behavior (Figure 7.3). We do not expect to see a large background spike in the W data at 180° since the background events that make it into the W sample are those where the non-muonic jet has been mis-measured so as to disappear, looking like a neutrino.

In Figure 7.4, we plot $\Delta\phi_{mj}$ for both PAPAGENO and the W sample. The two plots agree over most of the range. The apparent excess in the bins near 0° in both the PAPAGENO plot and the dijet background plot is apparently caused by the jet clustering algorithm suppressing a jet within $\Delta R_c = \sqrt{\Delta\eta^2 + \Delta\phi^2} = 0.7$ of an already existing calorimeter cluster. PAPAGENO simulates electrons, thus the event reconstruction supresses jets near the simulated electron calorimeter signal, leading to the difference with the muon data. Incorporating such a suppression effect into the muon W data yields Figure 7.5, where a better match is obtained.

By using Figure 7.5 we conclude that the QCD background is small. Figure 7.4 indicates that when not supressed, the jet reconstruction locates jets near the muon for ~ 20 events. This value is consistent with the previous result of 30 ± 20 events.

7.1.4 Backgrounds from Top Decays

The experimental Top quark mass limit is above the mass of the W, so Top may decay into real W's which we will measure as direct $q\bar{q} \rightarrow W \rightarrow \mu\nu$ production. At the current Top mass

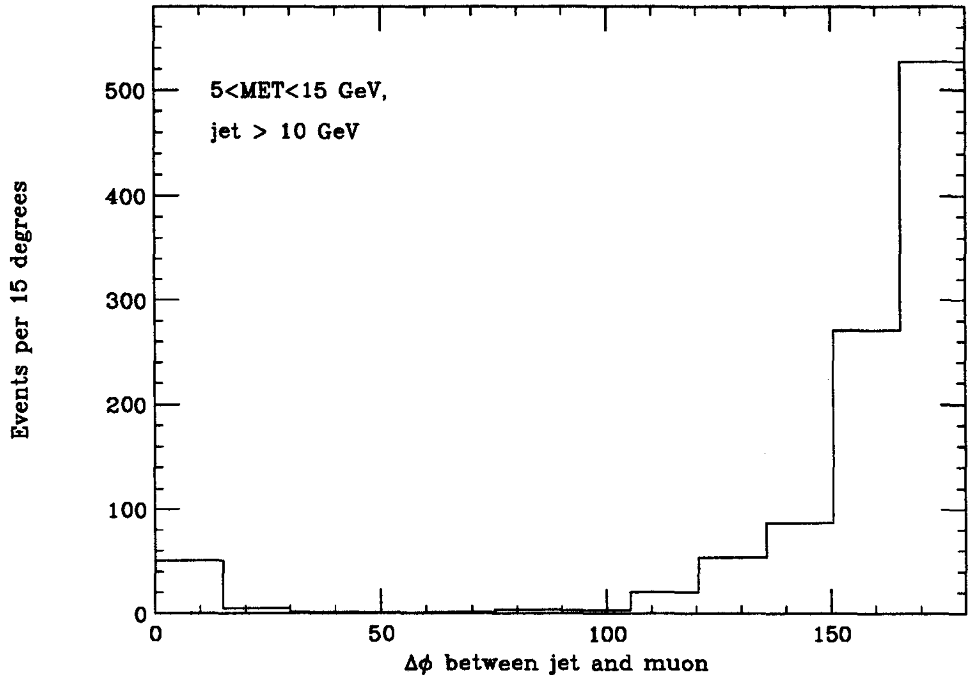

Figure 7.3: The two dimensional opening angle between the muon and the jet ($E_t^{jet} > 10$ GeV) in the background sample. The excess at 0° is cause by a $\Delta R_c > 0.7$ cut in the offline jet clustering.

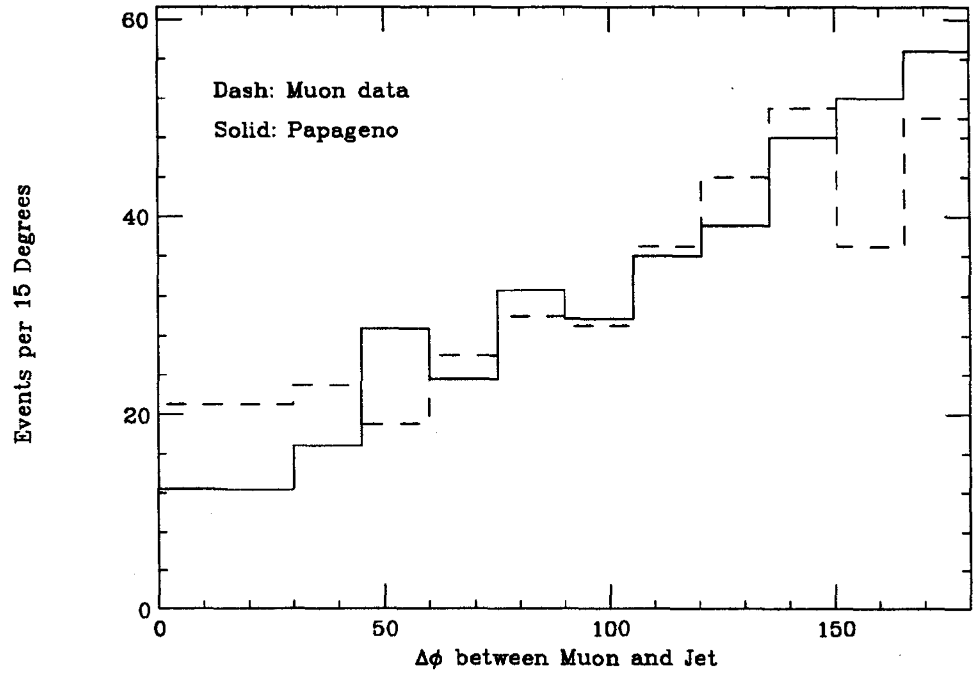

Figure 7.4: The two dimensional opening angle between the muon and a jet ($E_t^{jet} > 10$ GeV) in the W sample compared to that generated by the PAPAGENO $W + 1$ jet Monte Carlo generator.

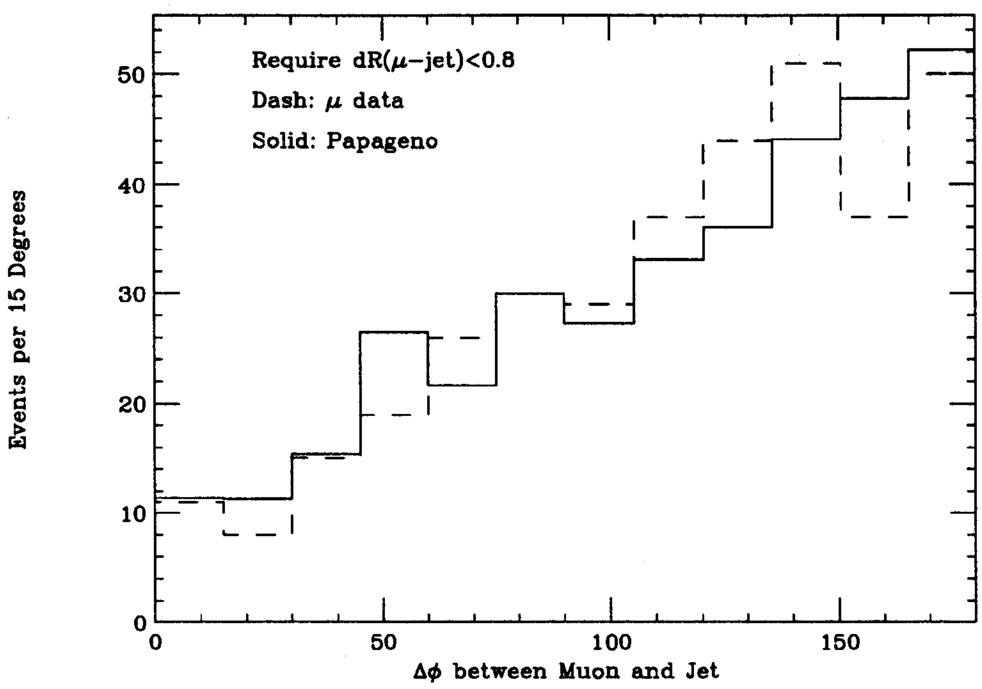

Figure 7.5: The two dimensional opening angle between the muon and a jet ($E_t^{jet} > 10$ GeV) in the W sample compared to that generated by the PAPAGENO $W + 1$ jet Monte Carlo generator after a $\Delta R_c > 0.7$ cut is imposed on the Monte Carlo as it is in the data.

limit of 91 GeV [64] the predicted cross section for $p\bar{p} \rightarrow t\bar{t}$ is 150 pb^{-1} at CDF energies. By using ISAJET and the full CDF detector simulation we found that a 91 GeV Top quark would contribute 15 background events to the W sample. Since the Top cross section falls with increasing M_{top}, this is an upper limit.

7.2 Cosmic Ray Background

While testing the cosmic filter for the purposes of measuring its efficiency of passing real $p\bar{p}$ events, as described in an earlier section, we found by hand-scanning that 2 out of 1000 events passing the cosmic ray filter were actually cosmic rays that should not have passed. An additional 3 events were possibly cosmics. The filtered test sample therefore contained

$$\frac{2+3}{1000} = 0.5 \pm 0.3\%$$

cosmic background, yielding 7 ± 4 events for the W sample and 0.5 ± 0.3 events for the Z's.

7.3 Backgrounds to Z Bosons

The Z events are much cleaner than the W events as there are very few processed that are able to mimic the Z signal. These are

- $W+$ jet, where the jet fluctuates in such a way to mimic a muon,
- QCD dijet events, where both jets appear as muons,
- $Z^0 \rightarrow \tau\tau$, followed by two $\tau \rightarrow \mu\nu\bar{\nu}$ decays,
- cosmic rays.

Cosmic rays have already been discussed in the preceeding section, so we shall consider the remaining three possibilities. The results are summarized in Table 7.2

7.3.1 W+jet and QCD DiJet Backgrounds to $Z^0 \rightarrow \mu^+\mu^-$

The techniques for investigating the existence of Z backgrounds caused either by a QCD dijet event or a W produced with a jet are similar. In each case we focus on the possibility that a jet will mimic a muon.

Although we impose an ISO cut on the golden muon in an event, the second muon in a Z event has no such requirement. If the second muon was a jet that fluctuated to appear as a

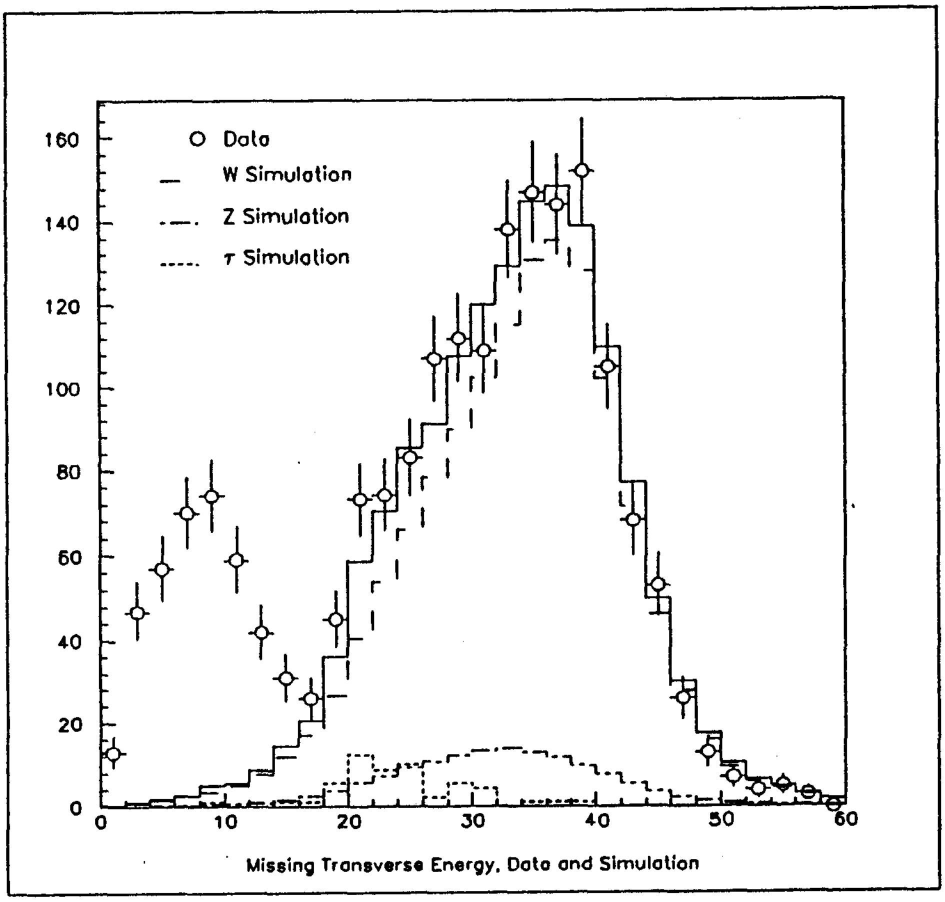

Figure 7.6: The $dN/d\not{E}_t$ spectrum for simulated W events showing the contributions for the primary backgrounds (one-legged Z's, W and Z tau events). The simulation shows a good match with the data (crosses). The low $\not{E}_t$ peak in the data is caused by dijet events where one jet fragments to mimic a muon. These are not in the final data sample, which is restricted to the region $\not{E}_t \geq 20$ GeV.

muon, we should see some energy in the calorimeter from the neutral particles in the jet. An examination of the Z data shows no excess energy around the muon.

The partons that produce jets evolve independently after the interaction. Since there is no requirement that two jets must appear as opposite-sign muons, or that a single jet in a W event have an opposite charge than the W, half of this type of background is expected to be like sign events. We see no like sign events in the Z sample, and thus expect no opposite-sign background.

In trying to use the W $ISO-$ $\not\!\!E_t^{\nu}$ method to calculate the QCD background, we find no events in the high ISO region. Thus we cannot extrapolate to the low ISO region, reinforcing the conclusion that there is no significant background.

As a final check, we estimate the expected amount of jet background to the Z sample, using the high-p_t dataset and apply the same cuts that were used to obtain the Z sample, except that we require the second muon to explicitly fail the calorimeter cuts, i.e. $E_{em} > 2$ GeV or $E_{had} > 6$ GeV. We assume that those particles that fail the calorimeter cuts are pions within a $W+$ jet event. We find 34 such events, of which 16 are opposite sign. There are 12 events within the Z mass window of $65 \leq M_{\mu\mu} \leq 115$ GeV/c^2. The probability of a pion traversing the calorimeter and leaving a signal in the CMU is approximately 2% [34, 35, 36]. We therefore multiply this probability by the number of pion events within the Z mass window as an estimate of the $W+$ jet background; obtaining 0.24 events for this type of background. We conclude that the total Z background from this type of process is 0^{+1}_{-0} events.

Type of Background	Events
Backgrounds to W	
QCD	30 ± 20
$Z \rightarrow \mu\mu$	
2^{nd} leg beyond CTC	$131 \pm 13 \pm 8$
2^{nd} leg in CTC	3 ± 3
$W \rightarrow \tau\nu$	$47 \pm 1.5 \pm 8.4$
$Z \rightarrow \tau\tau$	$2.8 \pm 0.3 \pm 0.9$
Top	0^{+15}_{-0}
Cosmics	7 ± 4
Backgrounds to Z	
$Z \rightarrow \tau\tau$	0^{+1}_{-0}
QCD	0^{+1}_{-0}
Cosmics	0.5 ± 0.3
Total W background	$B_W = 220^{+42}_{-27}$
Total Z background	$B_Z = 0.5^{+1.0}_{-0.3}$

Table 7.2: Backgrounds.

7.3.2 $Z^0 \rightarrow \tau\tau$, resulting in muons

The branching ratio of a τ decaying to a muon is 17.4%. With a $Z^0 \rightarrow \tau\tau$ event, we thus expect about 3% of the decays to be to a muon pair. As a crude estimate we expect approximately 688 $Z^0 \rightarrow \tau\tau$ events, producing $\sim$ 20 dimuon events. The muons from τ decays will have a much lower p_t than direct muons from Z decays, so we expect this value to be an extreme upper limit on the background.

We use ISAJET to generate $Z^0 \rightarrow \tau\tau$ events, which are then run through the CDFSIM detector simulation where we measure the acceptance of these events much like that of the $Z^0 \rightarrow \mu^+\mu^-$ events. Only 1 of 4008 events passed the Z selection criteria, yielding an acceptance of 0.00025 which, when normalized to the size of the $Z^0 \rightarrow \mu^+\mu^-$ sample, estimates a background of 0.1 event. We therefore conclude a background of 0^{+1}_{-0} events.

Chapter 8

Results

8.1 Drell-Yan Contribution to Z cross section

In addition to production by way of Z bosons, dimuons are also produced via virtual photons. Therefore the cross section is a combination of three terms:

$$|Z+\gamma|^2 = Z^2 + \gamma Z + \gamma^2,$$

where γZ represents the interference terms between the pure Z process and the pure γ process. In the mass window $65 < M_{\mu\mu} < 115$ GeV/c^2 dimuons come mainly from the Z term, although the photon terms contribute. Theorists usually calculate only the Z term, so to compare with theory, we need to correct for these contributions.

We obtained a version of the fast LO Monte Carlo generator which includes the photon terms. The correction factor for the photons was calculated as

$$DY = \int_{65}^{115} Z^2 dM \Big/ \int_{65}^{115} (Z^2 + \gamma Z + \gamma^2) dM = 0.97.$$

This term was also calculated using ISAJET, where we found agreement within 0.2%. We apply this factor to $\sigma \cdot B(Z)$ as a multiplicative correction.

8.2 Final $A \cdot \varepsilon$ for W's and Z's

Once the data sample is selected and the acceptances, efficiencies and backgrounds have been obtained (Table 8.1), the cross section can then be calculated using equation 2.6. The term ϵ_W in equation 2.6 is the product of several factors coming from geometric and kinematic cuts as well as from trigger and chamber performance and from cuts made in the offline analysis. A more specific relation for the $W^{\pm}$ cross section, in terms of the parameters we have determined, is

$$\sigma \cdot B(W \to \mu\nu) = \frac{N_W^{sig}}{A_W \cdot \varepsilon_g \cdot T \cdot \varepsilon_{cos} \cdot \int \mathcal{L}dt}, \tag{8.1}$$

where ε_g is the combined efficiency of the cuts defining a golden muon, T is the trigger efficiency and ε_{cos} is the efficiency of the cosmic ray filter for W and Z events.

The expression for the Z cross section is much more complex; there are two muons, increasing the number of possibilities to be considered when combining the efficiencies. Both muons may impact the CMU chambers and, if they do, both have a chance to fire the Level 2 Muon Trigger. Either, or both, might satisfy the gold muon identification requirements. The major terms of interest are

$$f \cdot A_Z \cdot T(2 - T) \cdot \varepsilon_g(2\varepsilon_{s1} - \varepsilon_g) \cdot \varepsilon_{cos} \tag{8.2}$$

$$f \cdot A_Z \cdot 2(1 - \varepsilon_{CMU}) \cdot T \cdot \varepsilon_g \varepsilon_{s2} \cdot \varepsilon_{cos} \tag{8.3}$$

$$(1 - f) \cdot A_Z \cdot T \cdot \varepsilon_g \varepsilon_{s2} \cdot \varepsilon_{cos} \tag{8.4}$$

where $\varepsilon_{s1} = \varepsilon_{CMU} \cdot \varepsilon_{m.i.} \cdot \varepsilon_{trk}$ is the loose-cut efficiency for tracks which project to the fiducial region of the muon chambers, and $\varepsilon_{s2} = \varepsilon_{m.i.} \cdot \varepsilon_{trk}$ is this efficiency for muon candidates which project outside this region (see Table 6.4).

The first term (8.2) counts events where both tracks extrapolate to the CMU and produce a CMU stub, and might also satisfy the gold muon requirements. The next term (8.3) counts events where both muons project to the fiducial region of the CMU, but for whatever reason one of the muons does not have an associated CMU stub, and thus had no chance at triggering. The last term (8.4) counts events where one track projects to the CMU, producing a muon stub, and the other projects beyond the end of the chambers or into a muon chamber crack.

In the data, we explicitly rejected events where both tracks project to the muon chambers, but only one has a stub. This removes term 8.3 from the expression for the acceptance-efficiency product for Z's, and one event from the data sample. We felt that the one event was not worth the added complication of the cross section equation, and removing the term simplified the formula for $\mathcal{R}_\mu$ as well.

The real advantage of the $\mathcal{R}$ measurement is apparent when we form the ratio of the W and Z cross-section formulas. With cancellations, the result is

$$\mathcal{R}_\mu = \frac{N_W^{sig}}{N_Z^{sig}} \cdot \frac{A_Z}{A_W} \cdot DY \cdot [f(2-T)(2\varepsilon_{s1} - \varepsilon_g) + (1-f)\varepsilon_{s2}] \tag{8.5}$$

in which we note the luminosity term is absent, along with its related uncertainty.

	W events	Z events
W/Z Candidates (N^{obs})	1436	106
Background:		
$Z^0 \to \mu^+\mu^-$	$134 \pm 13 \pm 8$	–
$W \to \tau\nu$	$47 \pm 1.5 \pm 8.4$	–
$Z^0 \to \tau\tau$	$2.8 \pm 0.3 \pm 0.9$	0^{+1}_{-0}
QCD	30 ± 20	0^{+1}_{-0}
Top	0^{+15}_{-0}	–
Cosmic rays	7 ± 4	0.5 ± 0.3
Total bkgd. (N^{bkg})	220^{+42}_{-27}	$0.5^{+1.0}_{-0.3}$
Total events (N^{sig})	$1216 \pm 38^{+27}_{-42}$	$106 \pm 10^{+0.3}_{-1}$
Efficiencies:		
Matching< 2 cm	$\varepsilon_{\Delta x} = 96.0 \pm 1.0\%$	
Minimum ionizing	$\varepsilon_{m.i.} = 98.7^{+0.3}_{-0.4}\%$	
Isolation	$\varepsilon_{ISO} = 98 \pm 1\%$	
Tracking	$\varepsilon_{trk} = 98.7 \pm 1.0\ \%$	
Muon 'stub' finding	$\varepsilon_{CMU} = 98.6^{+1.2}_{-3.3}\%$	
Total loose fiducial	$\varepsilon_{s1} = 96.0 \pm 3.5\%$	
Total loose non-fiducial	$\varepsilon_{s2} = 97.4 \pm 1.1\%$	
Total "tight" cuts	$\varepsilon_g = 90.4 \pm 3.8\%$	
Cosmic filter	$\varepsilon_{cos} = 99.8 \pm 0.1\%$	
Trigger	$T = 90.8 \pm 2.7\%$	
$A \cdot \epsilon$	0.156 ± 0.010	0.132 ± 0.010
$\sigma \cdot B$	$2.21 \pm 0.07 \pm 0.14$ nb	$226 \pm 22 \pm 18$ pb

Table 8.1: Summary of W and Z selection efficiencies, backgrounds and results. The first uncertainty is statistical and the second is systematic. The 6.8% systematic uncertainty in the integrated luminosity has not been included.

8.3 Final Muon Cross Sections and Ratio

Using equations 8.1 through 8.4 and Table 8.1, calculating the cross sections and $\mathcal{R}_\mu$ yields

$$\sigma \cdot B(W \to \mu\nu) = 2211 \pm 70(stat) \pm 144(syst) \pm 150(lum) \text{ pb}$$

and

$$\sigma \cdot B(Z^0 \to \mu^+\mu^-) = 226 \pm 22(stat) \pm 18(syst) \pm 15(lum) \text{ pb}$$

where the last uncertainty comes from the luminosity measurement. These results are illustrated in Figure 8.1, as are the CDF electron results from the '88-'89 run. The theoretical curve is from ref. [65].

As a cross check we varied the kinematic cuts on the muon p_t and on the $\not{E}_t^\nu$ in combinations of the values 20 and 25 GeV. Since the QCD backgrounds cluster near the 20 GeV cut, this should reveal any error in our estimates. We recalculate the acceptances and backgrounds (where the p_t and $\not{E}_t^\nu$ cuts were applied), but assume the efficiencies will remain the same. We observed a variation of less than 1% in $\sigma \cdot B(W \to \mu\nu)$, and conclude that the measurement is robust.

The cross section ratio determined from equation 8.5 is

$$\mathcal{R}_\mu = \frac{\sigma \cdot B(W \to \mu\nu)}{\sigma \cdot B(Z^0 \to \mu^+\mu^-)} = 9.8 \pm 1.1(stat) \pm 0.4(syst).$$

We can now rearrange equation 2.3 to obtain the W branching ratio. We note that the uncertainty in $\mathcal{R}_\mu$ is dominated by Z statistics, and therefore the variation in $1/\mathcal{R}_\mu$ more closely approximates a gaussian distribution than $\mathcal{R}_\mu$. Thus, the inverse branching ratio B^{-1}

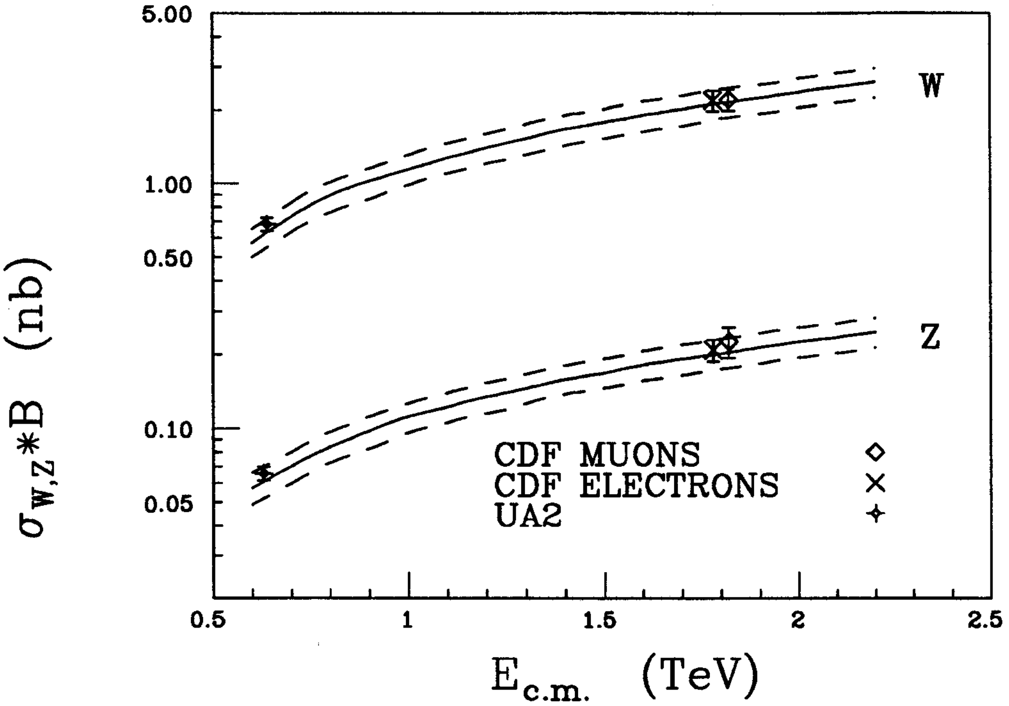

Figure 8.1: CDF Cross Sections versus c.m. energy. The theoretical predictions are from ref. [65] with the dashed curves outlining the 1σ uncertainties.

is a better defined quantity than B, so we rearrange equation 2.3 to obtain

$$B^{-1}(W \to \mu\nu) = \frac{\Gamma_{tot}(W)}{\Gamma(W \to \mu\nu)} = \frac{1}{\mathcal{R}_\mu} \cdot \frac{\sigma(W)}{\sigma(Z)} \cdot \frac{\Gamma_{tot}(Z)}{\Gamma(Z^0 \to \mu^+\mu^-)}. \tag{8.6}$$

Using the cross section ratio is about the only good way to measure $B(W \to \mu\nu)$. In examining equation 8.6 we note that the ratio $\frac{\sigma(W)}{\sigma(Z)}$ is theoretically well-defined, depending only on slight variations in the proton structure functions. The last term, $B^{-1}(Z^0 \to \mu^+\mu^-)$, has been measured very accurately at LEP [67], leaving the experimental measurement of $\mathcal{R}_\mu$ as the defining factor in determining $B(W \to \mu\nu)$.

Many theoretical uncertainties cancel in the total cross-section ratio, yielding

$$\frac{\sigma(p\bar{p} \to WX)}{\sigma(p\bar{p} \to ZX)} = 3.23 \pm 0.03$$

at $\sqrt{s} = 1.8$ TeV for HMRSB proton structure functions [66]. Also, LEP has measured the Z widths as $\Gamma(Z^0 \to \mu^+\mu^-) = 83.37 \pm 0.84$ MeV and $\Gamma_{tot}(Z) = 2.487 \pm 0.010$ GeV [67], from which we obtain

$$B^{-1}(W \to \mu\nu) = \frac{\Gamma(W)}{\Gamma(W \to l\nu)} = 9.9 \pm 1.2(stat + syst)$$

which agrees with the theoretical result of $B^{-1}(W \to \mu\nu) = 9.20 \pm 0.12$ obtained from [11] and presented in section 2.3.

The total width of the W isobtained by multiplying equation 8.6 by $\Gamma(W \to \mu\nu)$ and using the above LEP results and the theoretical value

$$\frac{\Gamma(W \to \mu\nu)}{\Gamma(Z^0 \to \mu^+\mu^-)} = \left(\frac{M_W}{M_Z}\right)^3 \frac{2}{1 - 4\sin^2\theta_W + 8\sin^4\theta_W}.$$

By using $M_W/M_Z = 0.8791 \pm 0.0034$ [68] and $sin^2\theta_W = 0.2327 \pm 0.00085$ [52] we find

$$\frac{\Gamma(W \to \mu\nu)}{\Gamma(Z^0 \to \mu^+\mu^-)} = 2.71 \pm 0.03,$$

which yields

$$\Gamma_{tot}(W) = 2.21 \pm 0.27(stat + syst) \text{ GeV}.$$

This measurement agrees well with the theoretical prediction of 2.08 ± 0.02 GeV [11].

Chapter 9

Conclusions

9.1 Combining the CDF Cross Section Results

We wish to combine these results with the CDF electron results [40] to obtain the the best CDF result to the $\sigma(W \rightarrow l\nu)$ and $\sigma(Z^0 \rightarrow ll)$ rates. Determination of the 'best' cross section ratio will also constrain the Top quark mass, and provide a test of lepton universality. CDF also obtained a low statistics measurement of $\sigma(W \rightarrow \tau\nu)$ [69], as seen in Table 9.1. Since the uncertainty of this measurement is large compared for that of the electron and muon

	CDF muon	CDF electron	CDF tau
	Statistical and systematic uncertainties		
$\sigma \cdot B(W \rightarrow l\nu)$ (nb)	$2.21 \pm 0.07 \pm 0.14$	$2.19 \pm 0.04 \pm 0.14$	$2.05 \pm 0.22 \pm 0.19$
$\sigma \cdot B(Z^0 \rightarrow ll)$ (pb)	$226 \pm 22 \pm 18$	$209 \pm 13 \pm 9$	
$\mathcal{R}_l$	$9.8 \pm 1.1 \pm 0.4$	$10.2 \pm 0.8 \pm 0.4$	
$B(W \rightarrow l\nu)$	9.9 ± 1.2	9.5 ± 0.9	

Table 9.1: Comparison of CDF muon, electron, and tau (when available) results. The 6.8% systematic uncertainty due to the luminosity has not been included.

measurements, little is gained by combining it with the others. We shall only use the tau measurement to complete the picture when measuring lepton universality at CDF.

The CDF electron and muon results were combined by using the method used by the Particle Data Group for combining results that have common systematic uncertainties [70]. The basic method is to assume that the data is of the form $A_i \pm \sigma_i \pm \Delta$, where Δ is the common systematic uncertainty. The weighted average is then

$$A = \frac{1}{w} \sum w_i A_i \tag{9.1}$$

where $w_i = \frac{1}{\sigma_i^2}$ and $w = \sum w_i$. This method requires separating the muon and electron uncertainties into two groups; completely correlated and completely uncorrelated. By doing so for the W's we obtain Table 9.2 [71] and the result obtained is

$$\sigma \cdot B(W \rightarrow \mu\nu) = 2211 \pm 124(uncorr) \text{ pb} \pm 8.44\%(corr) \tag{9.2}$$

$$\sigma \cdot B(W \rightarrow e\nu) = 2190 \pm 103(uncorr) \text{ pb} \pm 8.44\%(corr) \tag{9.3}$$

which gives, after the combination via equation 9.1,

$$\sigma \cdot B(W \rightarrow l\nu) = 2199 \pm 79(uncorr) \pm 186(corr) \text{ pb}.$$

The combined statistics for the electron and muon measurement give a statistical uncertainty of 38 pb. Subtracting this from the total uncertainty in the result above yields

$$\sigma \cdot B(W \rightarrow l\nu) = 2199 \pm 38(stat) \pm 198(syst) \text{ pb}.$$

	Muons		Electrons		Comments	Magnitude
	pb	%	pb	%		%
statistics	73.	3.2	44.	2.0	uncorrelated	–
A_W *S.F.*	75.	3.3	66.	3.0	correlated	3.3
A_W M_W	25.	1.1	17.5	0.8	correlated	1.1
A_W W P_T	5.0	0.22	22.	1.0	correlated	1.0
A_W *H.O.*	1.4	0.06	55.	2.5	correlated	2.5
ε_{vtx}	–	–	11.	0.5	uncorrelated	–
ε_{ν}	19.	0.83	46.	2.1	uncorrelated	–
lept id eff	103.	4.5	79.	3.6	uncorrelated	–
QCD BCK	37.	1.6	44.	2.0	correlated	2.0
Top BCK	27.	1.2	28.	1.3	correlated	1.3
$Z^0 \rightarrow ll$ BCK	8.2	0.36	14.	0.62	uncorrelated	–
$Z^0 \rightarrow \tau\tau$	negligible		negligible		uncorrelated	–
$W \rightarrow \tau\nu$	16.	0.69	9.0	0.41	uncorrelated	–
Lum	156.	6.8	150.	6.8	correlated	6.8

Table 9.2: Contributions to the electron and muon W cross section uncertainties. The last column contains the magnitudes of the value we use for the correlated uncertainties; always the larger of the electron and muon values.

For the Z's, using Table 9.3 [71] the results are

$$\sigma \cdot B(Z^0 \rightarrow \mu^+\mu^-) = 226 \pm 23.5(uncorr) \pm 7.2\%(corr)\ \text{pb}$$

$$\sigma \cdot B(Z^0 \rightarrow e^+e^-) = 209 \pm 15.8(uncorr) \pm 7.2\%(corr)\ \text{pb}$$

which combine to give

$$\sigma \cdot B(Z^0 \rightarrow ll) = 214 \pm 13(uncorr) \pm 15(corr)\ \text{pb}.$$

Again combining the statistics as for the W's, we find

$$\sigma \cdot B(Z^0 \rightarrow ll) = 214 \pm 11(stat) \pm 17(syst)\ \text{pb}.$$

	Muons		Electrons		Comments	Magnitude
	pb	%	pb	%		%
statistics	23.	9.7	13.	6.4	uncorrelated	–
A_Z	5.0	2.1	4.0	1.9	correlated	2.1
ε_{vtx}	–	–	1.0	0.5	uncorrelated	–
B_Z	–	–	2.6	1.25	uncorrelated	–
lept id eff	9.0	3.8	7.8	3.75	uncorrelated	–
Drell-Yan	–	–	2.1	1	correlated	1
Lum	16.	6.8	14.	6.8	correlated	6.8

Table 9.3: Contributions to the electron and muon Z cross section uncertainties. The last column contains the magnitudes of the value we use for the correlated uncertainties; always the larger of the electron and muon values.

When the CDF electron $\mathcal{R}$ measurement was obtained it was found that by rejecting events containing jets with $E_t > 10$ GeV the statistics were reduced, but in the process the systematic uncertainties were reduced as well. This allowed them to report a lower total uncertainty for the $\mathcal{R}$ measurement than obtained by simply taking the ratio of the cross sections. Therefore, the electron result is reported as the two individual cross sections, found with as many events as possible to reduce uncertainties and the ratio, obtained with a slightly reduced dataset to decrease the total uncertainty on $\mathcal{R}_e$. For this analysis, we combine our muon $\mathcal{R}_\mu$ result with the electron $\mathcal{R}_e$ result independently of the cross section results. Again the uncertainties are divided into correlated and uncorrelated parts using Table 9.4 [71],

$$\mathcal{R}_\mu = 9.8 \pm 1.15(uncorr) \pm 3.2\%(corr),$$

$$\mathcal{R}_e = 10.2 \pm 0.86(uncorr) \pm 3.2\%(corr)$$

which yields

$$\mathcal{R}_l = 10.0 \pm 0.69(uncorr) \pm 0.32(corr).$$

	Muons		Electrons		Comments	Magnitude
	absolute	%	absolute	%		%
statistics	1.1	11.5	0.8	7.8	uncorrelated	–
$\frac{A_Z}{A_W}$ (including ε_ν)	0.31	3.2	0.31	3.0	correlated	3.2
B_{WQCD}	0.15	1.6	0.05	0.5	uncorrelated	–
B_{WTop}	0.11	1.2	–	–	uncorrelated	–
$B_{WZ\to l^+l^-}$	0.03	0.3	0.03	0.3	uncorrelated	–
B_{WW_τ}	0.07	0.69	0.035	0.34	uncorrelated	–
B_{WZ_τ}	negligible		negligible		uncorrelated	–
B_Z	–	–	0.16	1.6	uncorrelated	–
e, μ id effy	0.16	1.7	0.29	2.8	uncorrelated	–

Table 9.4: Correlated and uncorrelated uncertainties of the $\mathcal{R}$ calculation. The last column contains the magnitude of the correlated uncertainty we used, which was the larger of the electron and muon values.

We again combine the statistics of the measurements to obtain

$$\mathcal{R}_l = 10.0 \pm 0.6(stat) \pm 0.4(syst).$$

Again proceeding as in the last chapter, we use equation 8.6 and the associated theoretical and experimental parameters to obtain

$$B^{-1}(W \to l\nu) = \frac{\Gamma_{tot}(W)}{\Gamma(W \to l\nu)} = 9.6 \pm 0.7(stat + syst),$$

and

$$\Gamma_{tot}(W) = 2.18 \pm 0.16 \text{ GeV}.$$

These results again agrees with the theoretical prediction, as did the muon-only results, and the first value issuperimposed on Figure 9.1 to obtain a 90%(95%) confidence level lower limit for the Top quark of 49(45) GeV/c^2.

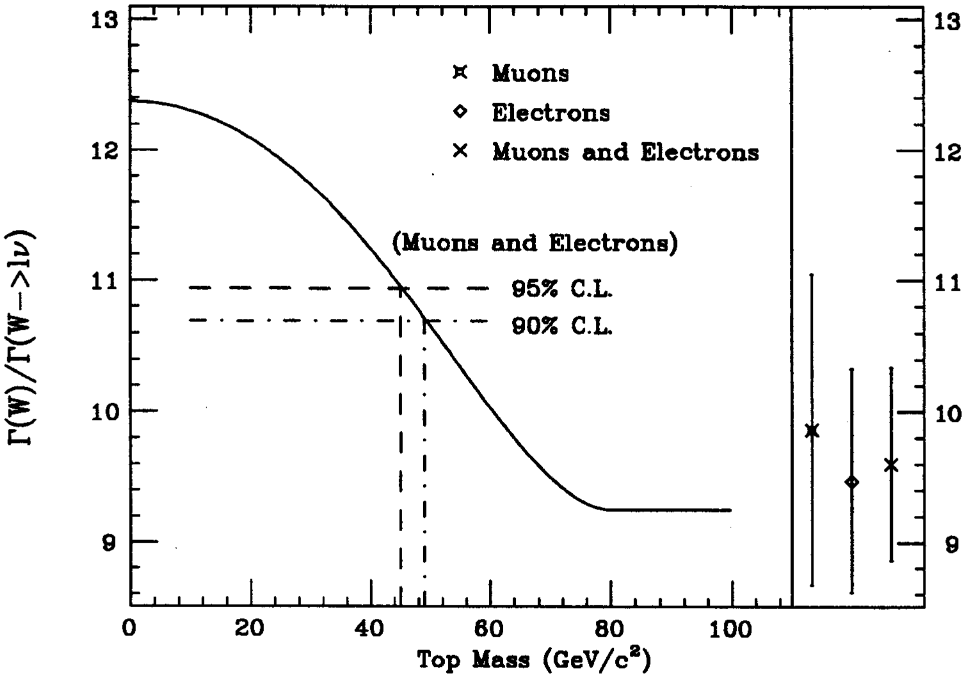

Figure 9.1: The relation of the W inverse branching ratio to the top mass, with the CDF electron, muon, and combined results included. We see that above 80 GeV/c^2, the Top mass has no effect on B^{-1}. The vertical lines represent the lower limit on M_{top} from this analysis.

9.1.1 Lepton Universality Tests from CDF Results

An additional physics goal of this analysis is to test lepton universality at the W mass scale. This may be directly measured via the relation

$$\left(\frac{g_\mu}{g_e}\right)^2 = \frac{\sigma \cdot B(W \to \mu\nu)}{\sigma \cdot B(W \to e\nu)}$$

which is assumed in the Standard Model to be unity. When taking the ratio of the electron and muon W cross sections we cancel the correlated uncertainties in eqns. 9.2 and 9.3. The ratio is thus

$$\frac{g_\mu}{g_e} = \sqrt{\frac{2211 \pm 124}{2190 \pm 103}} = 1.00 \pm 0.04(stat + syst).$$

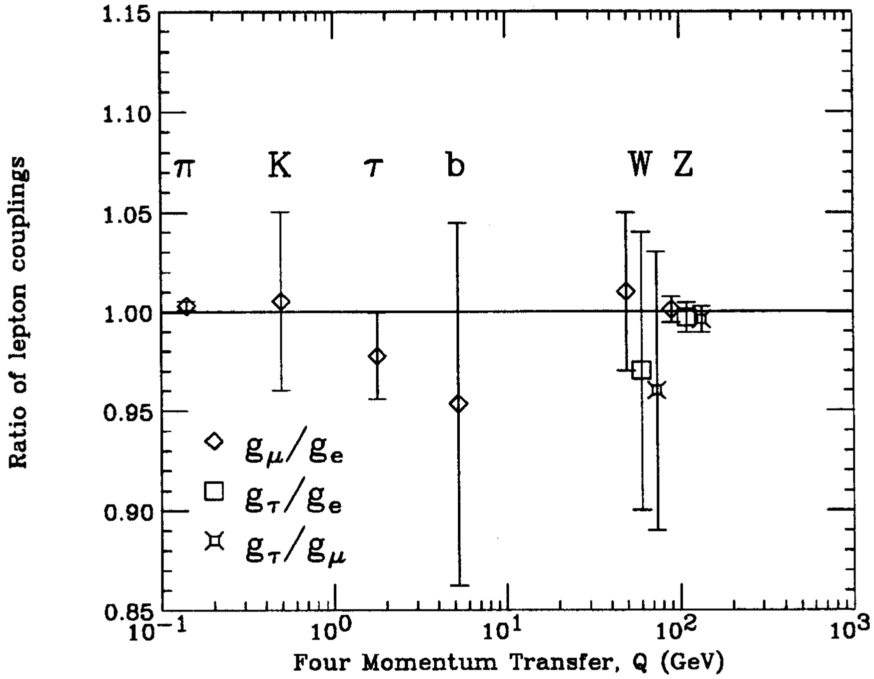

Figure 9.2: The lepton universality results from various experiments, plotted against the mass scale of the measurement.

We can also calculate the τ/μ ratio, yielding

$$\frac{g_\tau}{g_\mu} = \sqrt{\frac{2050 \pm 270}{2211 \pm 124}} = 0.96 \pm 0.07(stat + syst).$$

Both of these measurements are in excellent agreement with the Standard Model. These results are shown in Figure 9.2 along with the associated results of other experiments [72, 67].

9.1.2 Comparing CDF Experimental Results to Theory

The W and Z cross sections have been calculated to second order in α_s [73]. Table 9.5 is an excerpt of a table presented in [74] which predicts the W and Z cross sections and the cross section ratio for a range of proton structure functions, where we have taken the appropriate function. Taking our CDF combined values of $\sigma(W \rightarrow l\nu)$ and $\sigma(Z^0 \rightarrow ll)$, along with the

Parton Set	Tree Level			$\mathcal{O}(\alpha_s)$			$\mathcal{O}(\alpha_s^2)$		
	$\sigma(W)$	$\sigma(Z)$	$\frac{\sigma(W)}{\sigma(Z)}$	$\sigma(W)$	$\sigma(Z)$	$\frac{\sigma(W)}{\sigma(Z)}$	$\sigma(W)$	$\sigma(Z)$	$\frac{\sigma(W)}{\sigma(Z)}$
HMRSB	15.822	4.778	3.311	19.317	5.852	3.301	21.143	6.381	3.313

Table 9.5: The theoretical total boson cross sections (in nb) and the effect that QCD corrections have on the result. Note that for the ratio of the cross sections the QCD corrections have minimal effect.

theoretical branching ratios from [12] (reported in section 2.3), we calculate the total W and Z cross sections, obtaining

$$\sigma(W) = \frac{\sigma \cdot B(W \to l\nu)}{B(W \to \mu\nu)} = 20.5 \pm 1.9(stat + syst) \text{ nb},$$

$$\sigma(Z) = \frac{\sigma \cdot B(Z^0 \to ll)}{B(Z^0 \to \mu^+\mu^-)} = 6.4 \pm 0.6(stat + syst) \text{ nb},$$

and

$$\frac{\sigma(W)}{\sigma(Z)} = \mathcal{R}_l \cdot \left(\frac{B(Z^0 \to ll)}{B(W \to l\nu)}\right)_{thy} = 3.1 \pm 0.2(stat + syst).$$

We compare these values to those in the table and see that the best agreement for the total cross sections is for the $\mathcal{O}(\alpha_s^2)$ values, resulting in the conclusion that higher-order QCD processes are real and must be included in the boson cross section calculations. We also note that the experimental ratio of the total cross sections is consistent with the theoretical ratio, which is nearly constant with respect to the QCD corrections.

9.2 The Future

Earlier this year CDF conpleted taking data from Tevatron run Ia, and is currently preparing for run Ib at the Tevatron. The data from Ia is being analyzed, and future measurements of

W and Z production and decay parameters will have enough data to significantly reduce the statistical uncertainties on the measurements. The CDF detector is also being upgraded, which will allow greater particle identification efficiencies and reduce backgrounds. In particular the CDF muon detection system has been upgraded with another layer of central muon chambers and extensions which increase the effective fiducial volume in the η direction. These added features will combine to decrease the systematic uncertainties of a cross section measurement. The Tevatron is also expected to function at a full 1 TeV per beam in Ib, allowing the next set of measurements to be made in a new energy regime.

BIBLIOGRAPHY

[1] E. Rutherford, Phil. Mag. **21**:669 (1911).

[2] S. L. Glashow, Nucl. Phys. **22**:579 (1961).

[3] S. Weinberg, Phys. Rev. Lett. **19**:1264 (1967).

[4] A. Salam, Nobel Symposium #8, edited by W. Svartholm (1968).

[5] E. Fermi, "Tentativo di una Teoria dei Raggia", β. *Nuovo Cimento*, 11:1, 1934;
Ric. Sci., **4**, 491 (1933); reprinted in E. Fermi, *Collected Papers*, E. Serge, et al., editors
(University of Chicago Press, Chicago, 1962) vol. 1, pp.538-544
and Z. Phys. **88**:161 (1934).

[6] G. Arinson, et al. (UA1 Collaboration), Phys. Lett., **122B**:103 (1983).

[7] M. Banner, et al. (UA2 Collaboration), Phys. Lett., **122B**:476 (1983).

[8] G. Arinson, et al. (UA1 Collaboration), Phys. Lett., **126B**:398 (1983).

[9] P. Bagnaia, et al. (UA2 Collaboration), Phys. Lett., **129B**:130 (1983).

[10] P.N. Harriman, A.D. Martin, R.G. Roberts, W.J. Stirling, Phys. Rev. D42:798-810 (1990).

[11] "Review of Particle Properties", Phys. Rev. **45D**:III.61-62 (1992).

[12] "Review of Particle Properties", Phys. Rev. **45D**:II.1 (1992).

[13] F. Abe, et al. (CDF Collaboration), "The CDF Detector: An Overview", Nucl. Inst. and Meth. **A271**:387-403, (1988).

[14] F. Abe, et al., "The CDF Vertex Time Projection Chamber System", Nucl. Inst. and Meth. **A268**:75-91, (1988).

[15] F. Bedeschi, et al., "Design and Construction of the CDF Central Tracking Chamber", Nucl. Inst. and Meth. **A268**:50-74, (1988).

[16] S. Bhadra, et al., "The Design and Construction of the CDF Central Drift Tube Array", Nucl. Inst. and Meth. **A268**:92-104, (1988).

[17] L. Balka, et al., "The CDF Central Electromagnetic Calorimeter", Nucl. Inst. and Meth. **A267**:272-279, (1988).

[18] G. Apollinari, et al., "The CDF Central and Endwall Hadron Calorimeter", Nucl. Inst. and Meth. **A267**:301-314, (1988).

[19] Y. Fukui, et al., "CDF End Plug Electromagnetic Calorimeter Using Conductive Plastic Proportional Tubes", Nucl. Inst. and Meth. **A268**:50-74, (1988).

[20] J. Bensinger, et al., "An Electromagnetic Calorimeter for the Small Angle Regions of the Collider Detector at Fermilab," Nucl. Inst. and Meth. **A267**:257-271, (1988).

[21] S. Cihangir, et al., "The CDF Forward/Backward Hadron Calorimeter", Nucl. Inst. and Meth. **A267**:249-256, (1988).

[22] M. Bozzo, et al., Phys. Lett. **147B**:392 (1984);
D. Bernard, et al., Phys. Lett. **198B**:583 (1987).

[23] T. Liss, "Luminosity Monitoring and Beam-Beam Counter Performance", **CDF-552**.

[24] S. Belforte and K. Goulianos, "A Complete Minimum Bias Event Generator", **CDF-256**.

[25] G. Ascoli, et al., "CDF Central Muon Detector", Nucl. Inst. and Meth. **A268**:33-40, (1988).

[26] D. Amidei, et al., "A Two Level FASTBUS Based Trigger System for CDF", Nucl. Inst. and Meth. **A269**:51-62, (1988).

[27] G. Ascoli, et al., "CDF Central Muon Level 1 Trigger Electronics", Nucl. Inst. and Meth. **A269**:63-67, (1988).

[28] G. W. Foster, et al., "A Fast Hardware Track Finder for the CDF Central Tracking Chamber", Nucl. Inst. and Meth. **A269**:93-100, (1988).

[29] A. Mukherjee, "CTC Alignment and Calibration", **CDF-1006**.

[30] F. Abe, et al. (CDF Collaboration) Phys. Rev. Lett. **63**:720 (1989).

[31] S.R. Hahn et al., "Calibration Systems for the CDF Central Electromagnetic Calorimeter", Nuc. Inst. and Meth. **A267**:351 (1988).

[32] M. Binkley, S. Errede, B. Wicklund, "E/P Calibration of the CEM Energy Scale", **CDF-1226**.

[33] A.B. Wicklund, "E/P Calibration from Data", **CDF-1233**.

[34] D.A. Smith and H.B. Jensen, "Pion Punchthrough Probability in the Central Calorimeter", **CDF-707**.

[35] B. Denby, "A New Look at Punchthrough at CDF", **CDF-1324**.

[36] David Austen Smith, "Study of Muons Associated with Jets in Proton-Antiproton Collisions at $\sqrt{s} = 1.8$ TeV", Ph.D. Thesis (unpublished), University of Illinois, Appendix B (1989).

[37] W. Trischuk, L. Nodulman, "1988-89 Missing E_t Resolution", **CDF-948**

[38] A. Byon et al., "Cosmic Filtering of Central Muon Events", **CDF-1260.**

[39] C. Campagnari, "A Fast W and Z Monte Carlo", **CDF-1025.**

[40] F. Abe et al. (CDF Collaboration), "Measurement of the Ratio $\sigma(W \rightarrow e\nu)/\sigma(Z^0 \rightarrow e^+e^-)$ in $p\bar{p}$ Collisions at $\sqrt{s} = 1.8$ TeV", Phys. Rev. Lett. **64** 152 (1990).

[41] C. Albajar, et al. (UA1 Collaboration), "Measurement of the Ratio $R = \sigma(W)BR(W \rightarrow \mu\nu)/\sigma(Z)BR(Z^0 \rightarrow \mu^+\mu^-)$ and $\Gamma_{tot}(W)$ at the CERN $p\bar{p}$ Collider", Phys. Lett. **253B**:503 (1991).

[42] J. Alitti, et al. (UA2 Collaboration), "A Measurement of the W and Z Production Cross-Sections and a Determination of $\Gamma(W)$ at the CERN $p\bar{p}$ Collider", Phys. Lett. **276B**:365-374 (1992).

[43] F. Abe, et al. (CDF Collaboration), "A Measurement of the W Boson Mass in 1.8 TeV $\bar{p}p$ Collisions", Phys. Rev. D. **43D**:2070-2093 (1991);

[44] F. Abe et al. (CDF Collaboration), "Measurement of the W boson p_t Distribution in $\bar{p}p$ Collisions at $\sqrt{s} = 1.8$ TeV", Phys. Rev. Lett. **66**:2951-2955 (1991).

[45] F. Abe et al. (CDF Collaboration), "Measurement of the Z p_t Distribution in $p\bar{p}$ Collisions at $\sqrt{s} = 1.8$ TeV", Phys. Rev. Lett. **67**:2937-2941 (1991).

[46] P. B. Arnold and M. H. Reno, Nucl. Phys. **319B**:37 (1989);

P. B. Arnold and R. P. Kauffmann, Nucl. Phys. **349B**:381 (1991).

[47] I. Hinchliffe, "The PAPAGENO Partonic Monte Carlo Program", Submitted to Workshop on Physics at Current Accelerators and the Supercollider, Argonne, IL, 2-5 Jun 1993, LBL-34372.

[48] S. Behrends, et al., "Charged Track Corrections to Jets and the Effect on Jet Energy/Momentum Resolution", **CDF-1015**.

[49] M. Diemoz, F.Ferroni, E. Longo, G. Martinelli, Z. Phys. **39C**:21, (1988).

[50] J.G. Morfin and Wu-Ki Tung, Z. Phys. **52C**:13 (1991).

[51] K. K. Phua and Y. Yamaguchi, "Proceedings of the 25th International Conference on High Energy Physics", Singaport, August, 1990

[52] H. Burkhardt and J. Steinberger, "Tests of Electroweak Theory at the Z Resonance", CERN-PPE/91-50 (31 March 1991) for Vol. 41 of the Annual Review of Nuclear and Particle Science.

[53] J. Ng, "A Comparison between the W and the Z p_t distributions", **CDF-1504**.

[54] D. Kardelis, "Efficiency of 'Standard' Muon Calorimeter Cuts", **CDF-1301**.

[55] S. Miyashita, "CDF Detector Simulation and Analysis", **CDF-161**.

[56] D. Kardelis, "A Study of the CTC-CMU Matching Cut Efficiency for W Muon Analysis", **CDF-1336**.

[57] T.K. Westhusing and H. Grassmann, "$Z^0 \to \mu^+\mu^-$: Efficiency of the Pseudorapidity Cuts and Track Reconstruction", **CDF-1012**.

[58] M. Gold, "Search for High Mass Electron Pairs", **CDF-1229**;
M. Gold, "Limits on Z' and Compositeness from $p\bar{p} \to e^+e^-X$", **CDF-1302**.

[59] A. Byon, "Central Production of Charged Particles at CDF", Ph. D. Thesis (unpublished), Purdue University, page 67 (1989).

[60] A. Gauthier, "Efficiency of the Level 1 Central Muon Trigger", **CDF-937**.

[61] A. Gauthier and D. Kardelis, "Efficiency of the Level 2 Central Muon Trigger", **CDF-1106**.

[62] A. Gauthier, "Efficiency of the Level 3 Central Muon Trigger", **CDF-1145**.

[63] D. Kardelis, "Correlation Studies in the Muon R Analysis", **CDF-1525**.

[64] F. Abe, et al. (CDF Collaboration), "A Limit on the Top Quark Mass from $p\bar{p}$ Collisions at $\sqrt{s} = 1.8$ TeV", Phys. Rev. **45D**:3921-3948 (1992).

[65] Altarelli, Ellis, Greco, and Martinelli, Nucl. Phys. **246B**, 12 (1984);
Altarelli, Ellis, and Martinelli, Z. Phys. **27C**:617 (1985).

[66] A.D. Martin, W.J. Stirling, and R.G. Roberts, Phys. Lett. **228B**:149 (1989).

[67] J. M. Brom, D. Huss, M. E. Michalon ed., "Proceedings of the 11th International Conference on Physics in Collision", Colmar, June 1991

[68] F. Abe, et al. (CDF Collaboration), "Measurement of the W Boson Mass in 1.8 TeV Collisions", Phys. Rev. **43D**:2070 (1991).

[69] A. Roodman, "$W \to \tau\nu$", **CDF-1402**;

F. Abe, et al. (CDF Collaboration), Phys. Rev. Lett. **68**:3403-3407 (1992).

[70] Particle Data Group, "Review of Particle Properties", Phys. Lett. **239B**:III.35 (1990).

[71] S. Eno, D.A. Smith, C. Newman-Holmes, "Combined Boson Cross Sections", **CDF-1493**.

[72] D.I. Britton, et al., Phys. Rev. Lett. 68:3000-3, (1992);

T. Kinoshita, Phys. Rev. Lett. 2:477-480 (1959);

"Review of particle properties", Phys. Rev. **45D**:VI.20 (1992);

"Review of particle properties", Phys. Rev. **45D**:II.17 (1992);

F. Abe, et al. (CDF Collaboration), Phys. Rev. Lett. 68:3398-3402, (1992);

F. Abe, et al. (CDF Collaboration), Phys. Rev. Lett. 69:23-32, (1992).

[73] T. Matsuura, "Higher Order Corrections to the Drell-Yan Process", Ph.D. Thesis (unpublished), University of Leiden, (1989);

T. Matsuura, W. L. van Neerven, Z. Phys. **38C**:623, (1988);

T. Matsuura, et al., Phys. Lett. **221B**:171 (1988) and Nucl. Phys. **319B**:570 (1989).

[74] K. Einsweiler, "The W and Z Cross Sections: A Theoretical Appraisal", **CDF-1292**.

Vita

In 1969, young Ray sat on the outfield of a baseball field and wondered how the birds flew. His baseball coach, however, wished he'd pay more attention to the flying baseballs, so Ray achieved free agency. He then went through the Walled Lake school system in Michigan and read a lot. Exhausting the science books in the libraries of his elementary and junior high schools, Ray moved on to high school to see if they knew how the birds flew. This led to physics and math classes. Graduating from high school and having a computer at home, Ray did some independent study on the problem, and learned the wonders of the binary universe, including machine language, cellular automata, and cryptography. Soon, Ray decided he was having too much fun and went off to Michigan Tech to learn about both physics and skiing. The skiing didn't go so well, so Ray dropped that and started working on math. After three years at Michigan Tech, his friends could say that Ray knew a lot of B.S., two to be exact. Moving on to grad school, he decided to follow Steve Martin's advice, and "get small", by studying high energy physics. This led to many long drives to Fermilab in the dark of night, so he got his pilot's license. He also learned that, however the birds did it, they did it with a skill level that he could not match. Unfortunately, an airplane isn't very good for commuting once getting to his destination, so he didn't use one too often for the trip. After getting together with Dave,

Dave and Sarah, and having nothing to do, Ray started counting events. When he was done, his idle numerical intonations were written up and called a thesis, and Ray was thrust out of the nest, still wondering just how was it that the birds flew so well.